

Wissenschaftliche Mitteilungen

**aus dem
Institut für Meteorologie der Universität Leipzig**



ISBN 978-3-9814401-0-2

**Meteorologische Arbeiten (XVII) und
Jahresbericht 2011 des Instituts für
Meteorologie der Universität Leipzig**

Hrsg.: Armin Raabe

Leipzig 2012

Band 50

Wissenschaftliche Mitteilungen aus dem Institut für Meteorologie der
Universität Leipzig Bd. 50

C. Fricke, A. Ehrlich, M. Wendisch, B. Bohn Influence of surface albedo inhomogeneities on remote sensing of optical thin cirrus cloud mikrophysics.	1
P. Hoffmann, Ch. Jacobi Simulation of sudden stratospheric warmings with the Middle and Upper Atmosphere Model MUAM	11
Ch. Jacobi Long-term trends and decadal variability of upper mesosphere/lower thermosphere gravity waves at midlatitudes	25
Ch. Jacobi, C. Arras Enhanced sporadic E occurrence rates during the Geminid meteor showers 2006-2010	35
C. Unglaub, Ch. Jacobi, G. Schmidtke, B. Nikutowski, R. Brunner Proxies to describe ionospheric variability and heating rates of the upper atmosphere: current progress	45
H.-J. Schönfeldt Measuring saltation and creep with high spatial and temporal resolution	55
Jahresbericht des Instituts für Meteorologie 2011	69

Wissenschaftliche Mitteilungen aus dem Institut für Meteorologie der
Universität Leipzig Bd. 50

Influence of surface albedo inhomogeneities on remote sensing of optical thin cirrus cloud mikrophysics.

Clemens Fricke, André Ehrlich, Manfred Wendisch, Birger Bohn

Summary

Cirrus clouds play an important role in atmospheric chemistry and climate, but they are complicated to handle mostly due to the complex non-spherical shape of the particles and their spatial inhomogeneity which causes major problems in remote sensing of cirrus from satellite platforms. Therefore spectral measurements of solar radiation are applied on the new research aircraft for atmospheric research and earth observation of the german science community HALO (High Altitude and LOng range research aircraft). With its maximum flight altitude of 14 km combined with times of flight up to 10 hours it provides the opportunity to study fields of radiation all over the world. Aboard of the first HALO flight with operational scientific instruments (Techno-Mission in October/November 2010) a spectrometer system to measure the upward radiance was operated by the University of Leipzig together with an instrument for measurements of the actinic flux density in co-operation with the Forschungszentrum Jülich called HALO-SR (HALO-SolarRadiation). The data is generally used in combination with 1-dimensional radiative transfer calculations (1D) to derive informations on the shape and spatial distribution of cirrus cloud ice crystals based on the retrieval of Nakajima & King (King et al., 1990), supported by lidar data gathered by the DLR (Deutsche Luft und Raumfahrt) instrument WALES (WAter vapour Lidar Experiment in Space) during the Mission. Due to the low optical thickness of the observed cirrus clouds ($0.2 \leq \tau \leq 2$) the effect of the surface albedo has to be considered. In this regard, the topic of this report will be the influence of the heterogeneity of the surface albedo on the cloud retrieval. Based on the albedo map derived from MODIS satellite-data (MODerate resolution Imaging Spectroradiometer), the retrieval is performed in a statistic approach to determine the effect of the albedo variation on the retrieved cloud properties. Mean values and standard deviations of optical thickness and effective particle diameter are derived depending on frequency distributions of the surface albedo. For the cloud optical thickness the results are additionally compared with lidar data derived from the DLR instrument WALES. Methodology and results are presented.

Zusammenfassung

Zirruswolken sind hinsichtlich ihres Einflusses auf das Klima von besonderer Bedeutung, gleichzeitig aber aufgrund der komplexen nichtsphärischen Form ihrer Partikel schwer zu beschreiben. Des Weiteren verursachen räumliche Inhomogenitäten der Zirruswolken Probleme bei satellitenbasierten Fernerkundungsmessungen. In dem Zusammenhang finden Strahlungsmessungen auf dem neuen deutschen Forschungsflugzeug HALO mittels eines

neuen Spektrometersystemes statt. Die maximale Flughöhe von 14 km kombiniert mit einer Flugdauer von bis zu 10 Stunden bietet die Möglichkeit weltweit grossräumige Strahlungsfelder zu erfassen. Während der ersten HALO Kampagne mit wissenschaftlicher Instrumentierung an Bord (Techno Mission Oktober/November 2010) kam das Spektrometersystem HALO-SR (HALO-SolarRadiation) erstmalig zum Einsatz. Dabei wurden Messungen der aufwärtsgerichteten Strahldichte, betrieben von der Universität Leipzig, zusammen mit Messungen der aktinischen Flussdichte des Forschungszentrums Jülich durchgeführt. Die Strahldichtemessungen werden anschliessend mithilfe von eindimensionalen (1D) Strahlungstransferrechnungen genutzt, um Informationen über die Ausbreitung sowie die Form der Partikel der Zirruswolken auf Basis des Nakajima&King Verfahrens zu gewinnen. Aufgrund der zu untersuchenden optisch dünnen Zirren ($0.2 \leq \tau \leq 2$) muss hierbei zusätzlich der Einfluss der reflektierten Strahlung der Bodenoberfläche berücksichtigt werden. Dieser ist jedoch nicht eindeutig zuweisbar. Somit wird hier der Einfluss der Heterogenität der Bodenalbedo auf die Fernerkundung der Wolkeneigenschaften untersucht. Mittels von Satelliten (MODIS) gewonnenen Daten der Bodenalbedo wird die Fernerkundung in einem statistischen Ansatz durchgeführt. Gewichtete Mittelwerte und Standardabweichungen der optischen Dicke sowie der Effektivradien werden in Abhängigkeit der Verteilung der Bodenalbedo ermittelt. Zusätzlich werden die Ergebnisse der optischen Dicke mit den Messwerten des DLR (Deutsche Luft und Raumfahrt)-Lidars WALES (WAter vapour Lidar Experiment in Space) verglichen. Methodik und Ergebnisse werden dabei präsentiert.

Airborne measurements and cirrus cloud mikrophysics

Remote sensing techniques, either satellite or plane based, are a well established method for retrieving cloud microphysical parameters (Stephens et. al, 2007, Eichler, 2009). Multispectral measurements are used for this purpose. The information is gathered by measuring the upward directed radiation and using the spectral proportionalities relating to the radiation going into the atmosphere for a retrieval of cloud mikrophysic properties. For remote sensing purposes the appropriate measured parameter is the radiance.

$$I(\hat{s}) = \frac{dF}{d\Omega} = \frac{d\Phi}{dA_{\perp} d\Omega} \quad (1)$$

It describes the radiant flux $d\Phi$ entering a receiving plane dA_{\perp} perpendicular to the direction of the incident radiation \hat{s} , depending on the solid angle $d\Omega$ and is given in units of $\text{W m}^{-2} \text{nm}^{-1} \text{sr}^{-1}$. During October, 27th and November, 4th the radiance was measured during the first scientific HALO-campaign using a multispectral spectrometer from Zeiss operated by the University of Leipzig monitoring a spectral range between 350 nm and $2 \mu\text{m}$. With the measured radiance and the knowledge of the incident solar radiation input at the top of the atmosphere the reflectance R is calculated. Cloud microphysical and optical properties are retrieved using the method developed by Nakajima & King

(Nakajima & King, 1990). It bases on the main principle of using a non-absorbing wavelength in the visible spectral range (650 nm) in addition with an absorbing wavelength in the near infrared spectral region (1646 nm). One retrieved quantity is the cloud optical thickness τ .

$$\tau = \int_{z2}^{z1} b_{ext}(z) dz \quad (2)$$

It describes the integrated extinction b_{ext} within a given vertical column z . Thus it is a quantity to describe the fraction of radiation that is extinct by travelling through the cloud given by the integration limits. The second parameter is the effective radius of cloud particles r_{eff} ,

$$D_{eff} = 2 r_{eff} = \frac{\int dN/dD \cdot D'^3 dD'}{\int dN/dD \cdot D'^2 dD'} \quad (3)$$

which is described by the relation of the volume to the area cross section of the respective particle using a infinitesimal number of particles dN . However, this equation is only valid for spherical ice/water particles. For non-spherical ice crystal shape situations different approaches of parametrizations exist.

Influence of heterogeneous surface albedo

Optical thick clouds lead to high extinctions, thus the reflected radiance mainly results from scattering within in the cloud. The surface albedo has only a minor impact. The situation for optical thin clouds is more complex. The reduced extinction of optical thin clouds leads to an increased part of incident radiation that is passing the cloud either by transmission or scattering in forward directions. This fraction of radiation interacts with the surface. Depending on the albedo of the surface an increasing part of radiation reflected by the ground is transmitting and scattered in upward direction. Due to the fact of measuring the total amount of upward directed radiation during remote sensing measurements in nadir direction, the received signal consists of parts reflected by the cloud and parts reflected by the surface as well. To apply a N.-King retrieval the surface albedo has to be known exactly. The investigated measurements were performed in a flight altitude of 14 km covering cirrus cloud situations. These situations offer the following problem. The variability in the measured radiance results either from variations in the surface albedo or from the variation of cloud optical thickness. Both cloud optical thickness and surface albedo are highly inhomogeneous for the observed scene. Unfortunately, the variation of surface albedo is not known exactly. Using a fixed surface albedo may cause high errors in the retrieved cloud properties. These aspects lead to the question:

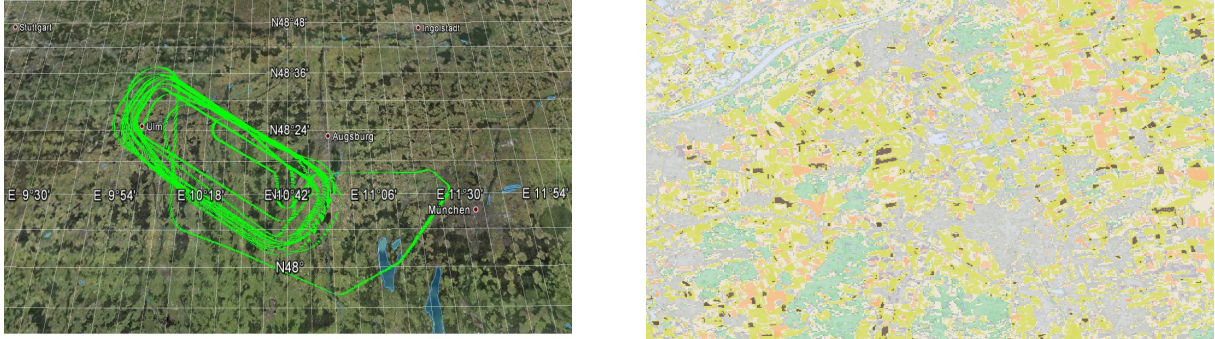


Figure 1: **left panel:** Example flight track showing the measurement area in the Allgäu region using GPS (illustrated using Google Earth). **right panel:** Classified surface albedo types of the area below the flighttrack within a windows of approximately 35 x 26,5 km. Classification includes several field types (yellow), different forest (green), urban (dark grey) and water areas (light grey). Image is based on LANDSAT data.

What is the exact influence of the surface albedo on the retrieval of cloud mikrophysics and is a cloud retrieval still possible without knowing the accurate albedo values?

Figure 1 shows the general situation during the flights. The investigated data was collected above a flight area (Allgäu, southern Germany) with a small scale heterogeneos surface albedo as shown in the right panel of Figure 1. It shows a classification of several surface types based on LANDSAT image data that were present in the flight area. The surface types are agricultural, urban, forest and water areas on a small scale.

To investigate the influence of the surface albedo on the cloud retrieval the following strategy has been applied. As no direct measurements exist, processed MODIS satellite data, based on GPS based flighttrackrecording, is used for the campaign time. These are time averaged athmospheric corrected albedo values representing the estimated surface reflectance as if there were no atmospheric scattering or absorption present (Wanner et. al, 1997). Because the Nakajima & King retrieval is based on the use of two wavelengths, the MODIS surface albedo is obtained for two available wavelength bands, a visible band covering 620 – 670 nm (VIS) and a near infrared band covering the 1628 – 1652 nm (NIR) range. The MODIS data is smoothed on the footprint size of the HALO-SR radiance measurements. The footprint results by combining the opening angle of the optical inlet (2°) and the flight path over which is integrated during the exposure time of up to five seconds. A measurement altitude of 14 km and flight velocities of 200 m/s were considered. Since no explicit allocation of the albedo value distributions of both wavelength bands to the radiance measurements is possible, the retrieval of τ and r_{eff} has to be performed in a statistic approach. In this regard 1D radiative transfer calculations are performed for each possible albedo combination of the whole distribution derived from MODIS. For the simulations the radiative transfer calculation package libRadtran (Mayer et. al, 2005) was used. For each albedo a possible combination of τ and r_{eff} is derived. The generated pool of possible solutions has to be weighted afterwards with the frequency distribution of the surface albedo. Thus a 2-dimensional frequency distribution of the combined VIS+NIR albedo value is generated (Figure 2). The combined albedo distribution presents a pro-

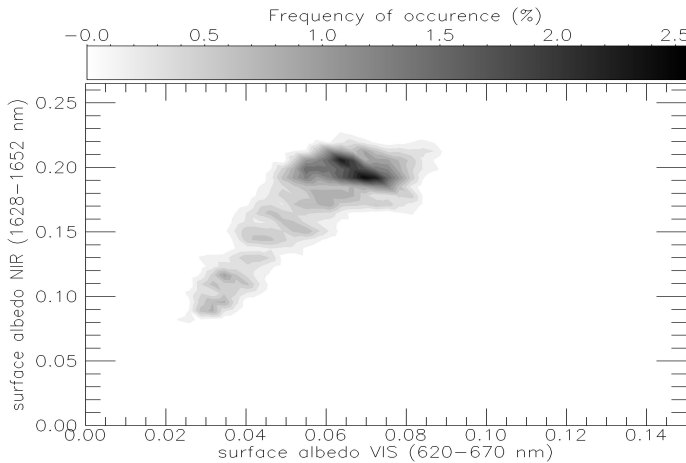


Figure 2: 2-dim. frequency distribution of the combined VIS+NIR surface albedo for the area of interest. Each value stands for a surface albedo pair with bin size of 0.005.

portional characteristic between both wavelenghts. It offers possible value pairs for the VIS between 0.025-0.09 and 0.08-0.23 for the NIR wavelength band with a maximum of VIS/NIR probability around 0.07/0.2. This distribution is now used to calculate weighted mean values (\bar{x}^*) and weighted standard deviations (σ^*) of τ and r_{eff} for each timestamp of measurement (4). Here, w_i is the weight for the i th albedo value of all combinations, N marks the amount of used combinations of albedo values and M the total amount of albedo values N .

$$\sigma^* = \sqrt{\frac{\sum_{i=1}^N w_i(x_i - \bar{x}^*)^2}{1 - \frac{1}{M} \sum_{i=1}^N w_i}} \quad \bar{x}^* = \sum_{i=1}^N w_i x_i \quad (4)$$

Figure 3 displays the results for two example measurements. A distribution of possible solutions is calculated of which the weighted statistic is generated afterwards. Both examples show similar results for τ ranging between 0.5 and 1 for the first and 0.7 and 1.3 for the second case. The narrow frequency distribution lead to small uncertainties with a standard deviation below 0.1. For r_{eff} both examples show differences in the valuation of the solution spaces of the frequency distributions leading to different uncertainties described by the standard deviation. The retrieval method has been applied for two parts of campaign flights from November, 3rd and November, 4th by calculating \bar{x}^* and σ^* for each measurement of a time series. Data with roll and/or pitch angles larger 3° were excluded from the retrieval. Figure 4 shows the retrieved results for the flight of November, 4th between 11:00 and 11:30 UTC. During the time of measurements HALO was at an altitude of 14 km. A cirrus cloud field between 9 and 13 km derived by the DLR lidar WALEs was situated below the plane.

The retrieval results for τ were compared to the optical thickness calculated by integration of the extinction backscatter coefficient measured by the DLR Lidar Wales during the

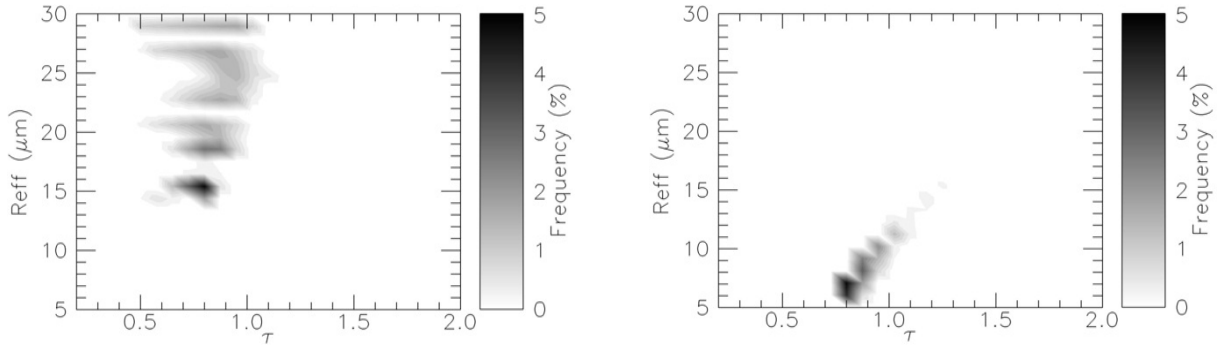


Figure 3: *Solution space of two measurement examples. While the possible τ is situated in a small band of solutions in both cases (between 0.5-1 in the left and 0.7-1.2 in the right case), r_{eff} offers a larger uncertainty in general as well as different uncertainties between the measurements ($dr_{eff} = 15 \mu m$ in the left and $dr_{eff} = 10 \mu m$ in the right case).*

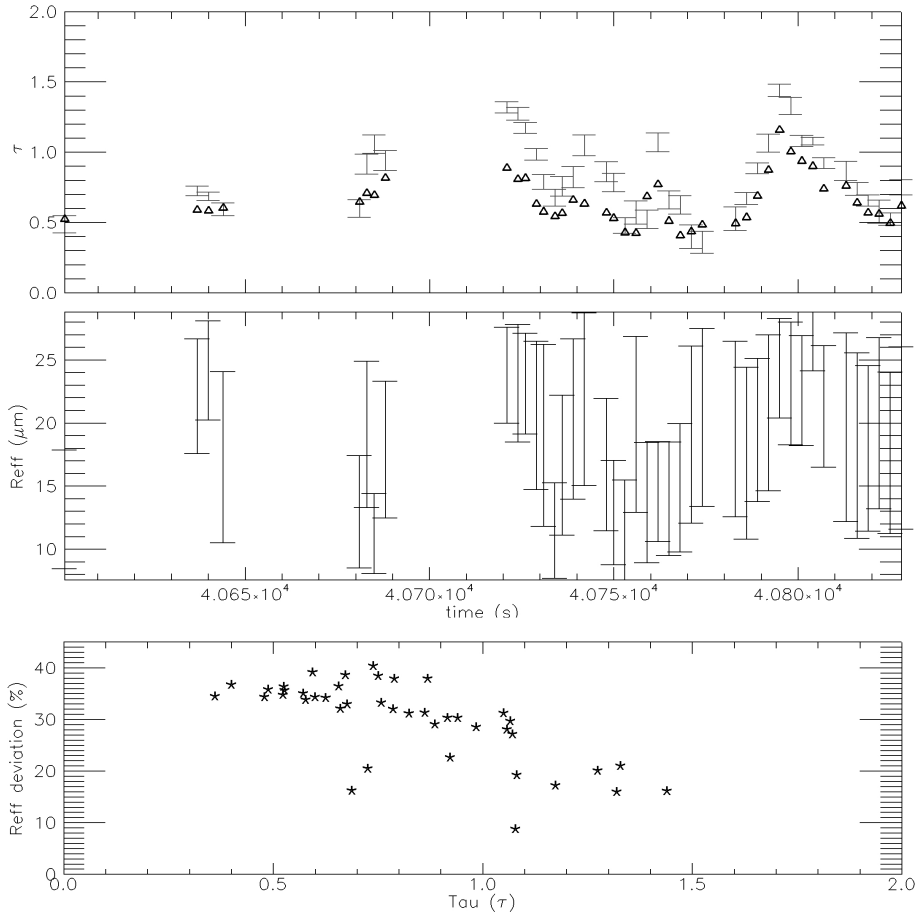


Figure 4: **upper panel:** τ comparison between statistic retrieval (bars) and values derived of the DLR Lidar WALES (triangle) from the November, 4th flight between 11:00 and 11:30 UTC. Gaps are caused by roll movements of the plane, where nadir measurements could not be obtained. **middle panel:** σ^* for r_{eff} of the corresponding timeframe. **lower panel:** τ dependance of r_{eff} deviation.

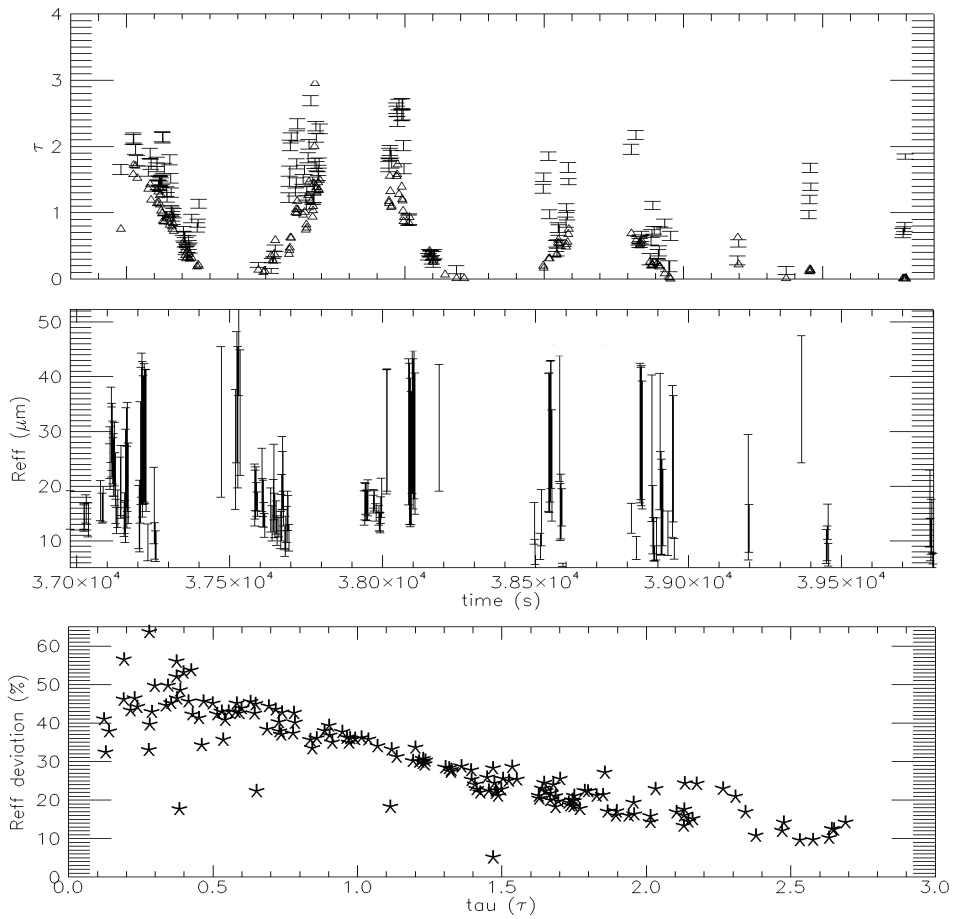


Figure 5: **upper panel:** τ comparison between statistic retrieval (bars) and values derived of the DLR Lidar WALES (triangle) from the November, 3th flight between 11 : 00 and 11 : 30 UTC. Gaps are caused by roll movements of the plane, where nadir measurements could not be obtained. **middle panel:** σ^* for r_{eff} of the corresponding timeframe. **lower panel:** τ dependance of r_{eff} deviation.

flight between 9 and 13 km. As displayed in the upper panel of *Figure 4*, the retrieved values for the optical thickness show similar characteristics between the statistic approach and the LIDAR values throughout the whole time frame. Although differences in the individual timestamps of measurements occur, the changing ascending and descending optical thickness during the time series can be seen in both results. The investigated cloud situation had optical thicknesses between 0.3 and 1.5 with deviations for the retrieved τ lower than 0.1. For r_{eff} the retrieved mean values vary between 5 μm and 24 μm with uncertainties between $\pm 3 \mu\text{m}$ and $\pm 7.5 \mu\text{m}$ as shown in the middle panel of *Figure 4*. Obviously there is a relationship between the uncertainty of r_{eff} and the retrieved values of τ . With increasing τ the deviation of r_{eff} decreases (*Figure 4*, lower panel). While the deviation is approximately 40 % for $\tau = 0.5$ it decreases to deviations of 20 % for $\tau = 1.5$. To verify this result, a time series of the flight from November, 3rd is shown in *Figure 5*.

Contrary to the flight of November, 4th the cloud field was not continuous during the

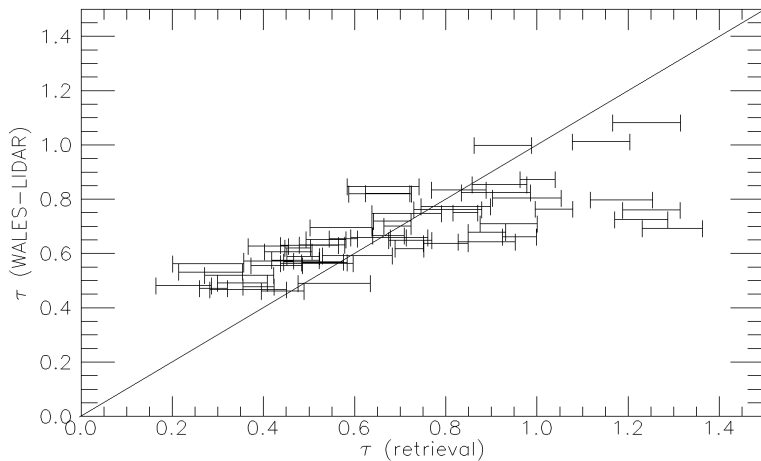


Figure 6: Comparison of statistic retrieval approach and LIDAR measurements to determine τ from a 30 min time series of the flight from November, 4th. Displayed are the weighted standard deviations as degree of uncertainty compared to the LIDAR values.

measurements. Cloudy and cloudless situations were alternating with two separate cloud layers below the plane. In areas with cirrus clouds a second cloud layer was situated around 5 km altitude below to the cirrus between 8.5 and 13 km. While the τ retrieved from the Lidar is based on the extinction between 7 and 13 km only, the statistic approach is based on the signal during the measurements including reflected radiation of the cloud in 5 km altitude. Thus, as seen in Figure 5 the statistic retrieval approach delivers higher values for τ . Nevertheless the time dependent characteristics are comparable again. The statistic approach leads to values of τ between 0.2 and 2.8 with deviations of the statistic retrieval below 0.1. \bar{x}^* for r_{eff} vary between $9 \mu\text{m}$ and $40 \mu\text{m}$ with a higher variation of deviation compared to the flight of November, 4th. As for the time frame from November 4th the deviation for the time series reaches values between 40 % and 50 % for $\tau = 0.5$. Correlating to the decreasing character of the deviation with increasing τ the deviation reduces to 10 % for $\tau = 2.5$. The reason for the decreasing deviation is the decreasing influence of the surface albedo with increasing τ as less radiation is transmitted through the cloud for higher cloud optical thickness. Unlike the consistently small deviation for the retrieved τ , the results for r_{eff} offer a high sensitivity to the values for τ .

The optical thickness derived from the lidar measurements are compared to the HALO-SR retrieval in Figure 6. Both results do not agree within the uncertainties for most of the measurements.

For low optical thicknesses ($\tau \leq 0.5$) the statistic approach results in an underestimation. With increasing ($\tau \geq 0.5$) it switches to an overestimation. One possible reason is the influence of the ice crystal shape. Different to water clouds the non-spherical particles are not consistently defined leading to several parametrization approaches. The calculations presented here are performed using an ice crystal parametrization by Baum (Baum et. al, 2007) simulating a mixture of different crystal shapes within a cloud. Differences of the observed clouds from the assumed ice crystal mixture would cause a deviation.

Another possible reason is the surface albedo product provided by MODIS combined with 1D radiative transfer calculations. Surface reflectances are dependent on the viewing

angle, as each surface type has a characteristic reflectance behavior that is described with the bidirectional reflectance distribution function (BRDF). At this point the radiative transfer calculations are performed in a 1D approach leaving out possible 3D radiative effects. Both reasons will be addressed in further investigations.

Conclusion

The influence of surface albedo inhomogeneities on the retrieval of cloud microphysics has been investigated. Because the affecting surface albedo necessary for the retrieval is unknown, the influence is investigated using a statistic approach. The optical thickness and the effective radius are retrieved by deriving statistic weighted mean values and standard deviations as dimensions for uncertainty. For the optical thickness the standard deviations ranges below 0.1 (including measurement error, which got considered by repeating the retrieval with limiting values given by the measurement error) which shows that the presented method is suitable for retrieving cloud optical thicknesses over heterogeneous surface situations when the exact influence cannot be addressed. It has to be pointed out that these results do hold only for the cloud analyzed here. The result is depending on the data pool the statistic is being performed with. The influencing surface albedo types should be reduced to a valuation which includes the affecting surface albedo types only. For the effective radius the suitability depends on the cloud optical thickness. The larger the part of the measured signal affected by the surface albedo the larger is the deviation of the effective radius gets. In consequence the statistic based retrieval of the effective radius offers only limited use as the influence for optical thin clouds leads to high deviations. Possible 3D as well as ice crystal particle shape effects are investigated in the following.

References

- Baum, B. A., Heymsfield, A. J., Yang, P., and Bedka, S. T., 2005a: Bulk scattering properties for the remote sensing of ice clouds. Part I: Microphysical data and models, *J. Appl. Meteor.*, 44, 1885-1895.
- Baum, B. A., Yang, P., Heymsfield, A. J., Platnick, S., King, M. D., Hu, Y. X., and Bedka, S. T., 2005b: Bulk scattering properties for the remote sensing of ice clouds. Part II: Narrowband models, *J. Appl. Meteor.*, 44, 1896-1911.
- Baum, B. A., Yang, P., Nasiri, S., Heidinger, A. K., Heymsfield, A., and Li, J., 2007: Bulk scattering properties for the remote sensing of ice clouds. Part III: High-resolution spectral models from 100 to 3250 cm⁻¹, *J. Appl. Meteor.*, 46, 423-434.
- Eichler, H., 2009:: Influence of Ice Crystal Habit and Cirrus Spatial Inhomogeneities on the Retrieval of Cirrus Optical Thickness and Effective Radius, PhD Thesis, University of Mainz.

- Key, J. R., Yang, P., Baum, B. A., and Nasiri, S. L., 2002: Parameterization of shortwave ice cloud optical properties for various particle habits, *J. Geophys. Res.*, 107, Art. No. 4181.
- Liang, S., Fang, H., Chen, M., Shuey, C. J., Walthall, C., Daughtry, C., Morisette, J., Schaaf, C., Strahler, A., 2002: Validating MODIS land surface reflectance and albedo products: methods and preliminary results, *Remote Sensing of Environment*, 83, 149-162.
- Mayer, B. and Kylling, A., 2005: Technical note: The libRadtran software package for radiative transfer calculations - description and examples of use, *Atmos. Chem. Phys.*, 5, 1.855-1.877.
- Nakajima, T., King, M. D., 1990: Determination of the Optical Thickness and Effective Particle Radius of Clouds from Reflected Solar Radiation Measurements. Part I: Theory, *Journal of the Atmospheric Sciences*, 47, No 15.
- Pierluissi, J. and Peng, G.-S., 1985:: New molecular transmission band models for LOWTRAN, *Optical Engineering*, 24, 541-547.
- Stephens, G. L. and Kummerow, C. D., 2007: The remote sensing of clouds and precipitation from space: A review, *J. Atmos. Sci.*, 64, 3742-3765.
- Wanner, W., Strahler, A.H., Hu, B., Lewis, P., Muller, J.-P., Li, X., Barker Schaaf, C.L., Barnsley, M.J., 1997: The remote sensing of clouds and precipitation from space: A review, *J. Atmos. Sci.*, 64, 3742-3765.
- Wendisch, M., Yang, P., 2012: Theory of Atmospheric Radiative Transfer: A Comprehensive Introduction.

Simulation of sudden stratospheric warmings with the Middle and Upper Atmosphere Model

P. Hoffmann, Ch. Jacobi

Abstract

The Middle and Upper Atmosphere Model has been used to simulate the middle atmosphere variability by changing the lower boundary conditions. For this purpose quasi steady-state simulations were performed for individual days around the sudden stratospheric warmings (SSWs) in January 2009 and 2012. The modelled time series reveal a qualitatively good agreement with reanalysis zonal wind with the observed one by reanalysis at the same height and latitude. A medium-range prediction of SSW events appears possible if planetary waves (PW) in the lower stratosphere are additionally assimilated in form of externally forced travelling PW.

Zusammenfassung

Mit dem Modell der mittleren und oberen Atmosphäre ist der Einfluss der unteren Randbedingungen auf die Variabilität der mittleren Atmosphäre simuliert worden. Dafür wurden eine Vielzahl quasi-stationärer Modellläufe durchgeführt, die in ihrer Gesamtheit den zeitlichen Verlauf der plötzlichen Stratosphärenwärmungen im Januar 2009 und 2012 wiedergeben. Es zeigt sich, dass der modellierte mittlere Zonalwind in qualitativ guter Übereinstimmung zu den Reanalysen liegt. Bei einer zusätzlichen Assimilation stratosphärischer planetarer Wellen wäre eine Mittelfristvorhersage für stratosphärische Erwärmungen möglich.

1. Introduction

The circulation of the atmosphere also includes the thermosphere/ionosphere system. Through vertical coupling processes by upward propagating small scale gravity waves (GW) with high phase speeds (e.g., Fritts and Vadas, 2008), global wave structures such as planetary waves (e.g., Borries and Hoffmann, 2010; Mukhtarov et al., 2010; Hoffmann et al., 2011) or even more irregular phenomena (e.g., sudden stratospheric warmings; SSWs) may be transferred into the upper atmosphere (e.g., Goncharenko et al., 2010). Usually, a direct impact is not possible due to the wind reversal in the mesosphere/lower thermosphere (MLT) region. Because standard reanalysis products, e.g., ECMWF and MetOffice (Swinbank and Ortland, 2003), provide only data up to the lower mesosphere (~ 60 km) satellite measurements, e.g., from TIMED (<http://www.timed.jhuapl.edu/WWW/index.php>) and model results help to extend the picture up to the thermosphere. Until now, there exists no comprehensive database to investigate the signals of the middle atmosphere in a changing climate.

In order to simulate the so-called “meteorological” influence on the thermosphere, whole atmosphere circulation models, for example, HAMMONIA¹(Schmidt and Brasseur, 2006),

¹HAMBurg Model of the Neutral and Ionized Atmosphere

WAM²(Wang et al., 2011), and TIME-GCM³(Roble and Ridley, 1994), can be used to reproduce the observed phenomena in the stratosphere (SSW, PW) first. The response of the middle and upper atmosphere can be studied next.

Here, we simulate quasi steady-state conditions with MUAM⁴ (Pogoreltsev et al., 2007) for each day around the SSW in January 2009 and 2012 by changing the lower boundary conditions (zonal mean temperature and stationary planetary waves). These are taken from NCEP reanalysis (Kalnay et al., 1996).

In according to Kuroda (2008), which declare the role of the stratospheric polar vortex on the quality of seasonal forecasts, a potential medium-range prediction of SSW events (30 days) will be proposed by running small ensemble simulations (6 members) with slightly different amplitudes of externally forced travelling PW components.

2. Nature of sudden stratospheric warmings

The state of the polar winter circulation in the stratosphere/mesosphere is more disturbed than on the summer hemisphere due to the global distribution of PW and their interaction with the mean flow. An intensification of these global scale waves, which are predominantly stationary and westward propagating, lead to momentum deposition, an oscillating state, and a non-zonal symmetric structure of the background winds (e.g., Haynes, 2005). So-called sudden stratospheric warmings (SSW) are the consequence of the polar vortex breakdown. The preconditions of SSW in the troposphere has been recently studied by Cohen and Jones (2011). They found that sea-level pressure anomalies over the north Atlantic and north Pacific (Arctic Oscillation) that influence the Siberian high may be responsible for an intensified upward energy flux. This oscillating state of the background flow continues for one or two weeks and impede the vertical propagation of PW into the mesosphere. Instead of that, a reflexion of the wave occur that leads to a downward interaction between stratosphere and troposphere (e.g., Reichler et al., 2005; Kodera et al., 2008; Hinssen et al., 2011).

Recently, a major stratospheric warming in January 2012 caused cold weeks at the end of that month up to about mid February over Siberia and Central and Eastern Europe as well. Such behaviour is a typically feedback of the tropospheric circulation on SSW at midlatitudes (e.g., Limasuvan et al., 2004; Mukougawa et al., 2005; Mukougawa and Hirooka, 2007; Hirooka et al., 2007). Figure 1 illustrates a troposphere-stratosphere-troposphere cycle around a SSW event. Reichler et al. (2005) divides the life-time in five stages: (1) forcing of PW, (2) upward-propagation, (3) wave breaking, (4) downward-propagation and (5) tropospheric feedback. This leads to weaker tropospheric westerlies associated with more defined blocking patterns (e.g. Schoeberl, 1978; Labitzke, 1981; Hinssen et al., 2011) in the North Atlantic Oscillation (NAO). However, the nature of trigger mechanisms (e.g. tropical convections) that cause such phenomena is not still completely understood.

Especially, the role of the middle atmosphere in the future climate and the change of SSW in frequency and intensity will be an important question to answer. Currently, climate models (e.g. ECHAM5) do not really include middle atmosphere dynamics (note, however, that the recent ECHAM6 model includes a more detailed middle atmosphere). Generally,

²Whole Atmosphere Model

³Thermosphere- Ionosphere-Mesosphere-Electrodynamics general circulation model

⁴Middle and Upper Atmosphere Model

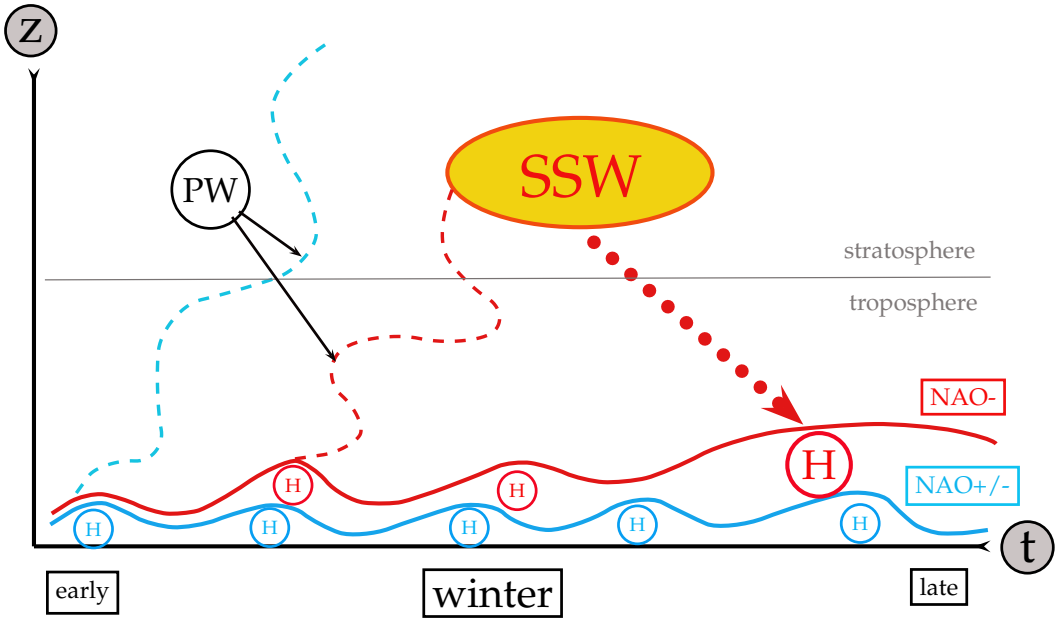


Figure 1: *Scheme of the troposphere-stratosphere-troposphere interaction during sudden stratospheric warming (SSW) events after Reichler et al. (2005).*

climate models underestimate the feedback of the stratosphere to the troposphere during SSW events.

3. Model setup

The mechanistic circulation model MUAM was operated in the following configurations. The simulations start with a windless atmosphere and stationary waves are forced by the lower boundary conditions (daily NCEP fields). During the “warm-up” process (0-120 model days) the atmospheric circulation develops under steady-state conditions (e.g., monthly mean ozone climatology). After 30 days the model Earth begins to rotate and tidal waves are excited due to the ozone absorption in the lower stratosphere. Finally, the model results from days 120-150 are averaged and the obtained middle atmosphere circulation (up to 130 km) corresponds to the day that is used as lower boundary condition. Altogether 89 simulations (from 2008-12-01 to 2009-02-28) has been performed automatically in order to simulate the conditions around the SSW event in January 2009. During the runs the declination angle of the sun and the monthly ozone distribution is set in accordance to the respective day. Other than in previous simulations with MUAM (e.g. Pogoreltsev et al., 2007; Hoffmann and Jacobi, 2011) the most important parameters have been defined as namelist in order to modify these without recompile the model code. In Tab.1 we summarize some technical information about the running system. By starting simulations on 2008-12-01 with the model “warm-up” (CPU time ca. 1.5h) one obtains a quasi “steady state” 0.5h later. These 30 days of model results are saved and converted into *netcdf* format. The temporal average represents the conditions for the particular day and is calculated later by external analysis software. The following days are modelled by replacing the lower boundary conditions. After further 30 model days (0.5h) the new state is obtained. This saves CPU time because the assimilation of the new data starts from the previous tuned model state. Accordingly, a 3-month season simulation takes about 2 days of CPU time on one server and one cluster. The obtained data require about 62

GByte disk space.

Ensemble simulations with a sufficiently large number of runs per day (e.g., 40) enable additional application for such models for a potentially seasonal forecast.

simulations	“warm-up”	“steady state”	“state change”
			<i>change LB</i>
model days	0-90 d	90-120 d	120-150 d
CPU-time	1.5 h	0.5 h	0.5 h
space into Netcdf format	not saved	683.4 MByte	683.4 MByte

	2008-12-01	2008-12-02 to 2009-02-28	total
“warm-up”	1	0	1
“steady state”	1	0	1
“state change”	1	88	89
CPU-time / h	2	44	< 2 days
disk-space / GByte	0.6834	60.8226	~ 62

Table 1: *List of technical parameters related to ensemble simulations with MUAM on compute-servers at LIM.*

4. Simulation of SSW in January 2009

In this section we describe the simulation results by only replacing the lower boundary conditions for the day 2009-01-010 (before SSW) and 2009-01-20 (during SSW). For the two situations the modelled mean zonal wind, stationary planetary waves and the Eliassen-Palm-flux divergence is discussed. Finally, the course of the 89 simulations from 2008-12-01 to 2009-02-28 are compared with NCEP reanalysis data ($\sim 30\text{km}$).

4.1 Lower Boundary Conditions

Information about the real atmosphere are taken from NCEP reanalysis data. The spectral components of the first 3 zonal harmonics in temperature and geopotential height were extracted from the 1000hPa pressure level as well as the zonal mean temperature distribution up to about 30km. The latitudinal distributions of these parameters are depicted in Fig.2. This corresponds to the global distribution of high (positive) and low (negative) geopotential height shown in Fig.3.

2009-01-10 (before SSW)

On the northern winter hemisphere the amplitude distribution (Fig.2, left panel, top) for the zonal wavenumber 1-3 indicates a dominant maximum of wave 1 (solid) at 60°N

($A_{W1} = 170m$). Quasi stationary waves with shorter horizontal wavelength are weaker. At lower midlatitudes ($\sim 40^\circ\text{N}$) the amplitude of wave 1 decreases below the one of wave 2 and 3 (dashed, dotted). On the global map in Fig.3 (left panel) the longitudinal distribution of geopotential height around 60°N reveals high geopotential (pressure) over the continents (Siberia) and low geopotential (pressure) over the north Atlantic ocean. At midlatitudes we observe a superposition of wave 2 and 3 mainly caused by the land-sea contrast there. Also local synoptical disturbances (high over Central Europe) that are usually reduced by averaging over one month are visible considering daily values. These may be responsible to trigger SSW events.

2009-01-20 (after SSW)

A few days later the amplitude distribution changes dramatically. Figure 2 (right panel, top) shows that wave 2 achieves almost the same magnitude as wave 1 has. Due to the strong pressure gradient over the north Atlantic (negative NAO index) it develops two cells with high geopotential; one over north east Siberia and another one over Aleuts. In transition of the two states on 2009-01-15 wave 2 and 3 dominates at midlatitudes ($40^\circ\text{N}-60^\circ\text{N}$) with similar amplitude of about $A_{W2} \simeq A_{W3} \simeq 130m$. The positions of the maxima (not shown here) are slightly shifted with 40°N (W2) and 50°N (W3).

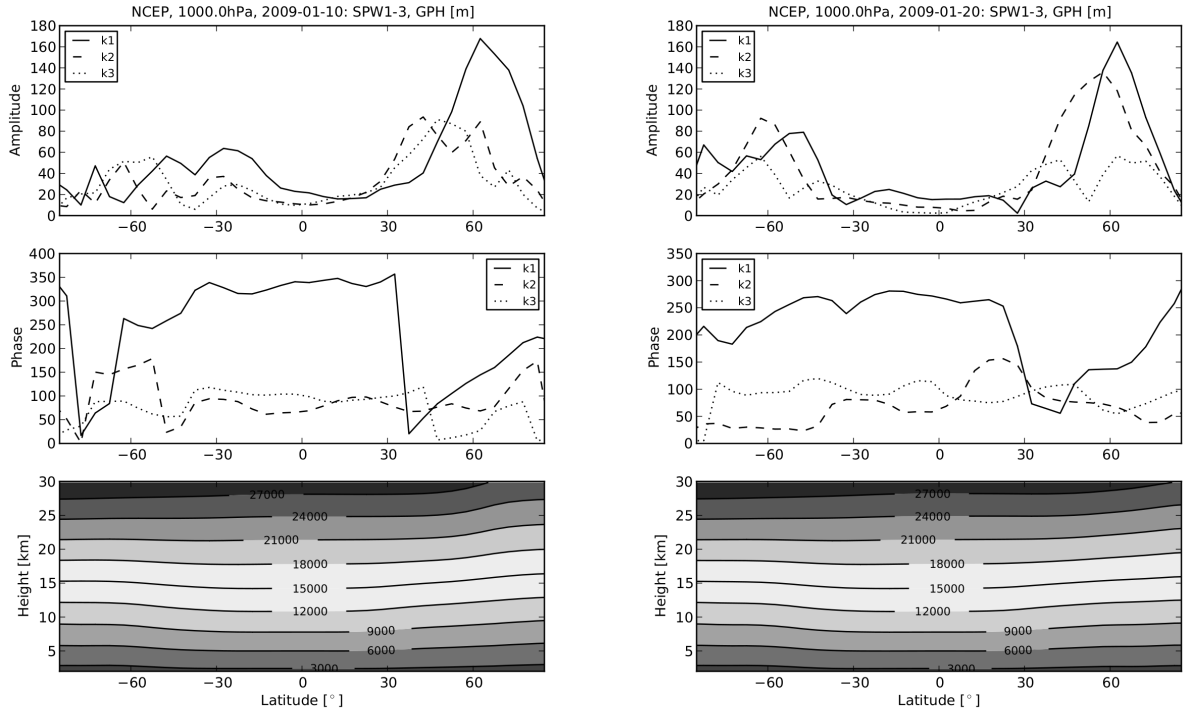


Figure 2: *Latitudinal distribution of amplitude (upper) and phase (middle) of the first three zonal harmonics in geopotential height at 1000 hPa on 2009-01-10 (left) and 2009-01-20 (right). The lower panels show cross sections of the zonal mean geopotential height.*

4.2 Wave-mean flow interaction

The model simulations for the previously discussed lower boundary conditions are shown in this subsection. Thereby, we focus on the northern hemisphere. The most prominent

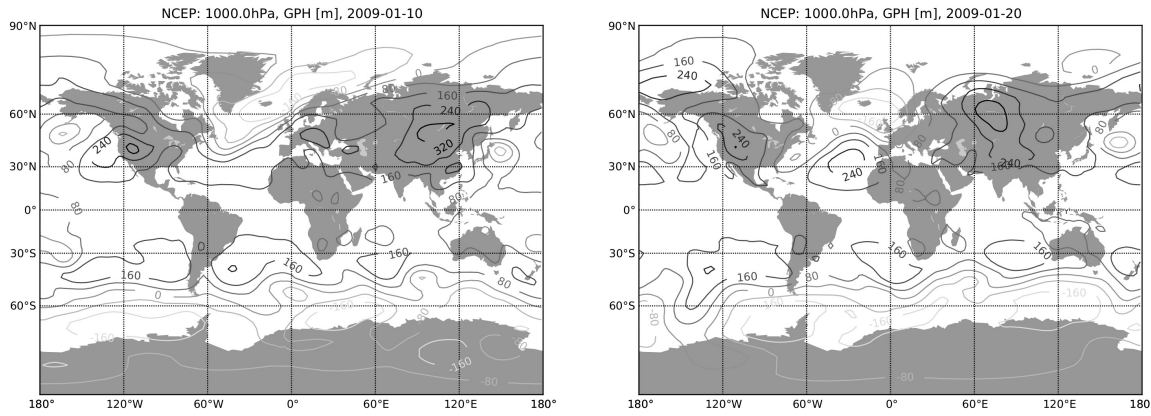


Figure 3: *Maps of geopotential height distribution at 1000 hPa pressure level on 2009-01-10 (left) and 2009-01-20 (right).*

wave features in the middle atmosphere are stationary planetary waves (SPW). These are forced in the troposphere (distribution of continents) and propagate upward during westerly wind regimes on the winter hemisphere. Because our simulation base on daily initial data they result in a strong variation of SPW. Figure 4 presents height-latitude cross sections of SPW1-3 amplitudes for the days 2009-01-10 (upper row) and 2009-01-20 (lower row). In according to the amplitude distribution as provided by the lower boundary conditions (see Fig.2) the SPW1 show the strongest magnitude of about 18K before SSW. 10-days later the pattern reverse. On 2009-01-20 (during SSW) SPW2 dominates (12K) and SPW1 reaches only about 6K. The amplitude of SPW3 changes from 4K to 2K. How far this component has an impact on SSW is unclear.

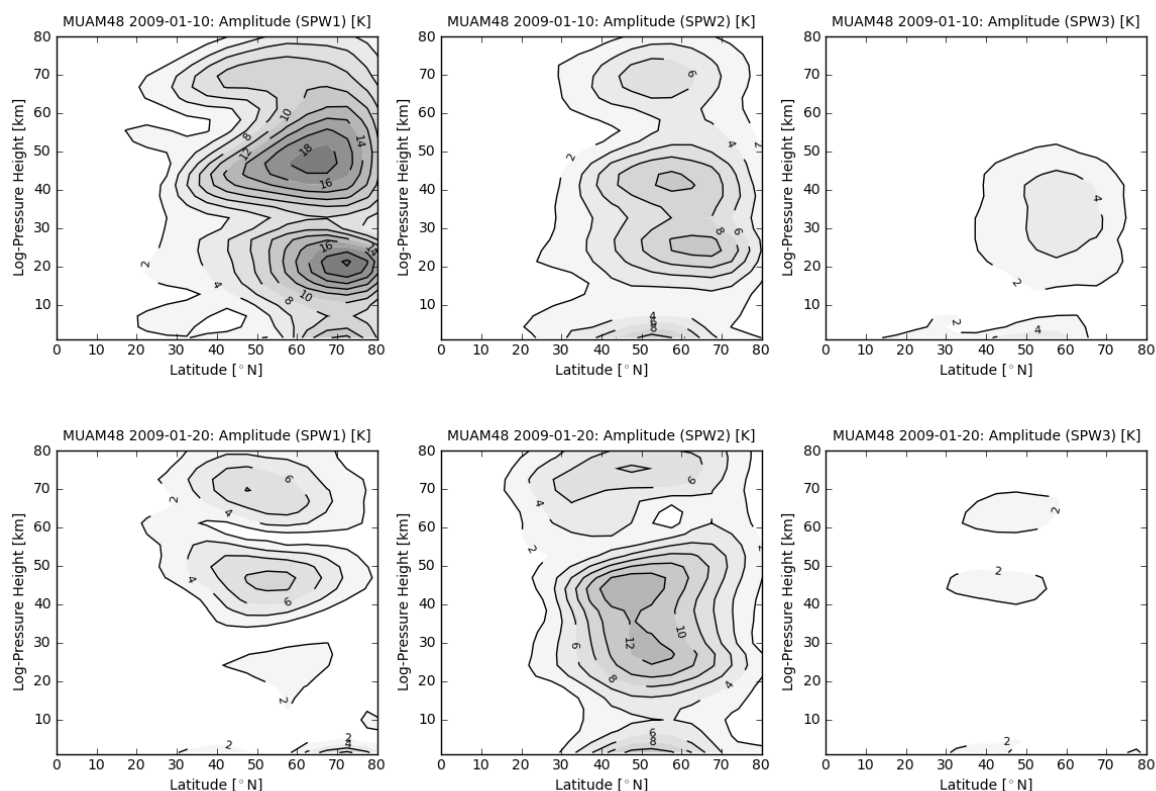


Figure 4: *Height-latitude cross section of SPW amplitude simulated with MUAM using the daily lower boundary conditions 2009-01-10 (upper row) and 2009-01-20 (lower row): SPW1 (left), SPW2 (middle) and SPW3 (right).*

This wave characteristics is a signature of the SSW itself.

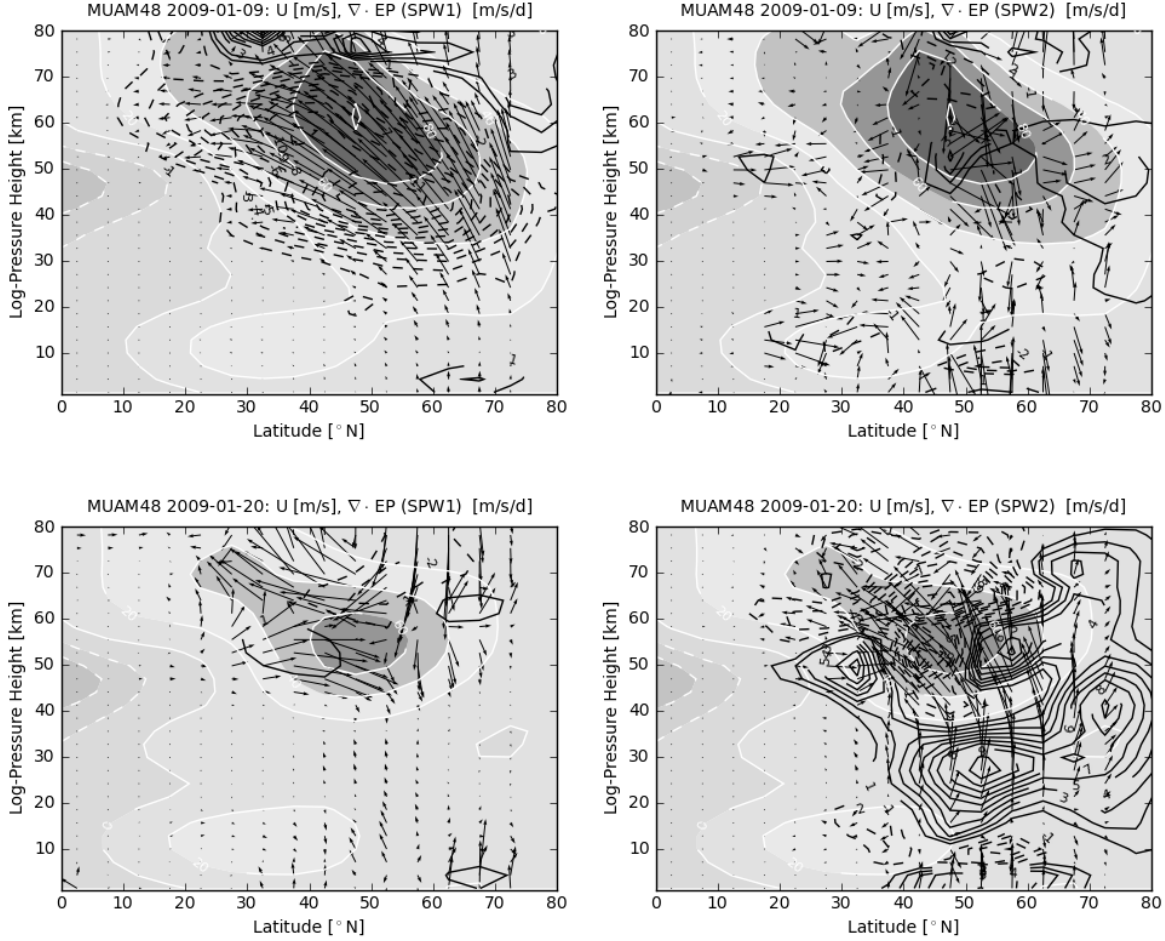


Figure 5: *Height-latitude cross section of Eliassen-Palm Flux (arrows) divergence (black contours) of SPW1 (left) and SPW2 (right) simulated with MUAM using the daily lower boundary conditions 2009-01-10 (upper row) and 2009-01-20 (lower row). The mean zonal wind is given in greyscaling, respectively.*

4.3 NCEP-MUAM comparison

The north-polar projection of the geopotential height distribution (Fig.6) near 30km reveals the dramatic breakdown of the polar vortex within a few days. The upper row represents MUAM simulation results for the two dates. The lower row shows the NCEP data, respectively. In both cases the polar vortex is deep and undisturbed on 2009-01-10 and weak and strongly disturbed on 2009-01-20, even though the bipolar structure is not fully reconstructed with the model. This is well-explained by the absence of travelling PW. During the warming PW at high latitudes are reflected at the easterly wind jet.

A temporally resolved picture is obtained by collecting all 89 MUAM runs to reproduce the atmosphere circulation around the SSW event in January 2009. Figure 7 (lower row) depicts the course of the single simulations (circles) from 2008-12-01 to 2009-02-28 in comparison to the NCEP data (solid line) at 62.5° N/30km for mean zonal wind (left panel)

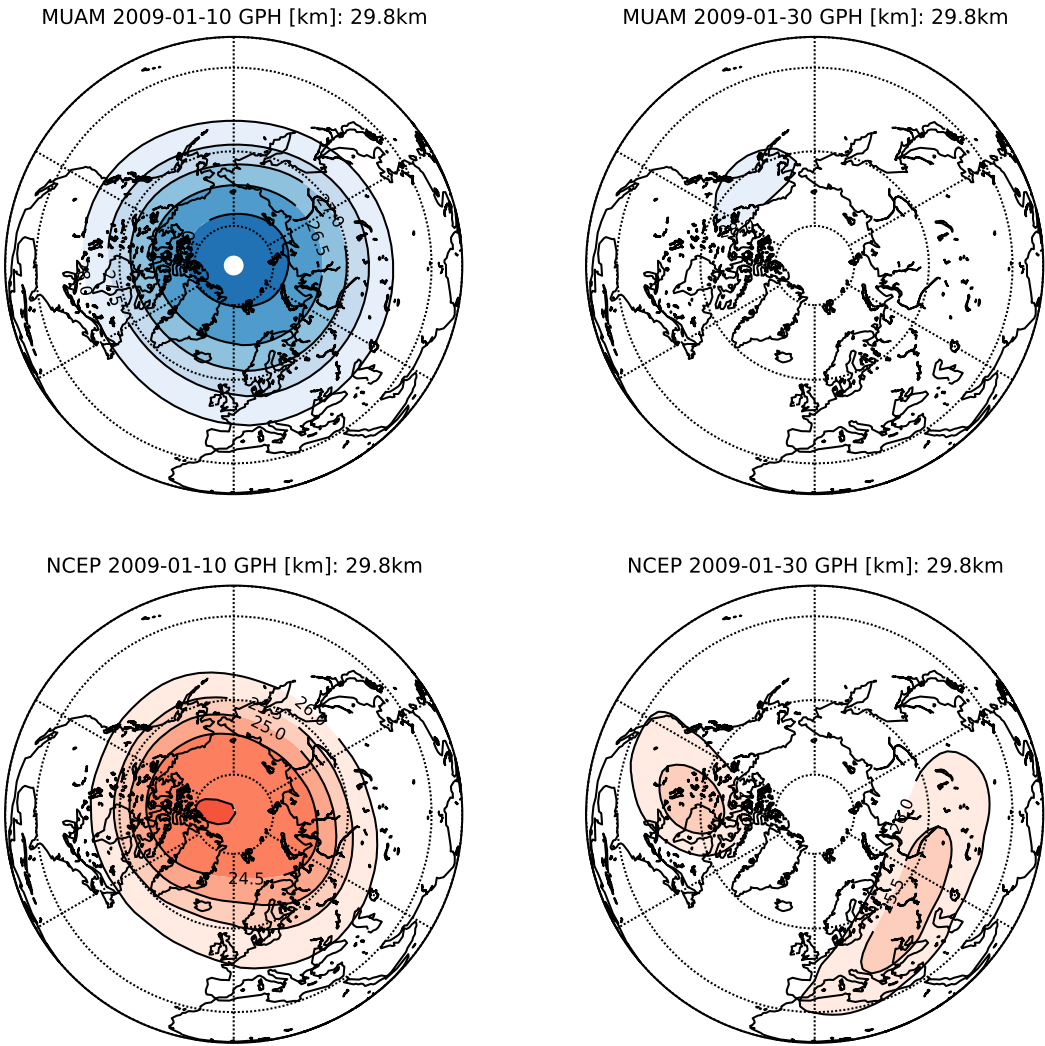


Figure 6: *North-polar projection of geopotential height near 30km in MUAM (upper row) and NCEP (lower row) for 2009-01-10 (left column) and 2009-01-30 (right column).*

and temperature (right panel). On 2009-01-10 the circulation begins to change abruptly. The mean zonal wind decreases within the following 20 days from 55m/s to -15m/s . This is accompanied with a temperature increase of about $30K$. MUAM simulations are able to reproduce such tendencies in winds quite well, even though the temperature increase only amounts to $12K$. Especially, the warming episode around 2009-01-30 is underestimated and the precondition of the warming indicates an offset of about $-5K$. This results in a much too weak zonal wind reversal. Thus, the assimilation of externally forced travelling PW is necessary to improve the precision of the simulation. They import extra energy and momentum into the system and will rise the mean temperature and reinforce the wind reversal. From this example we can see that the temperature response of the dynamical development follows with a delay of circa 10 days. However, a time shift between the MUAM simulations and NCEP reanalysis is not visible as expected. The modelled response of the MLT region to the assimilated SSW in the lower stratosphere is depicted in the Fig.7 (upper row). At an approximated height of about 100km (log-pressure height) the zonal wind values are consistently negative (easterly). The pre-

condition is characterized by a strong oscillating state of the background wind and temperature. With the onset of the decreasing zonal wind at 30km, a shortly continuing wind jump from -20m/s to 35m/s and back reveals the vertical coupling over more than 50km, quasi simultaneously. This shows the relevance of SSWs and PW on the dynamics of the upper atmosphere.

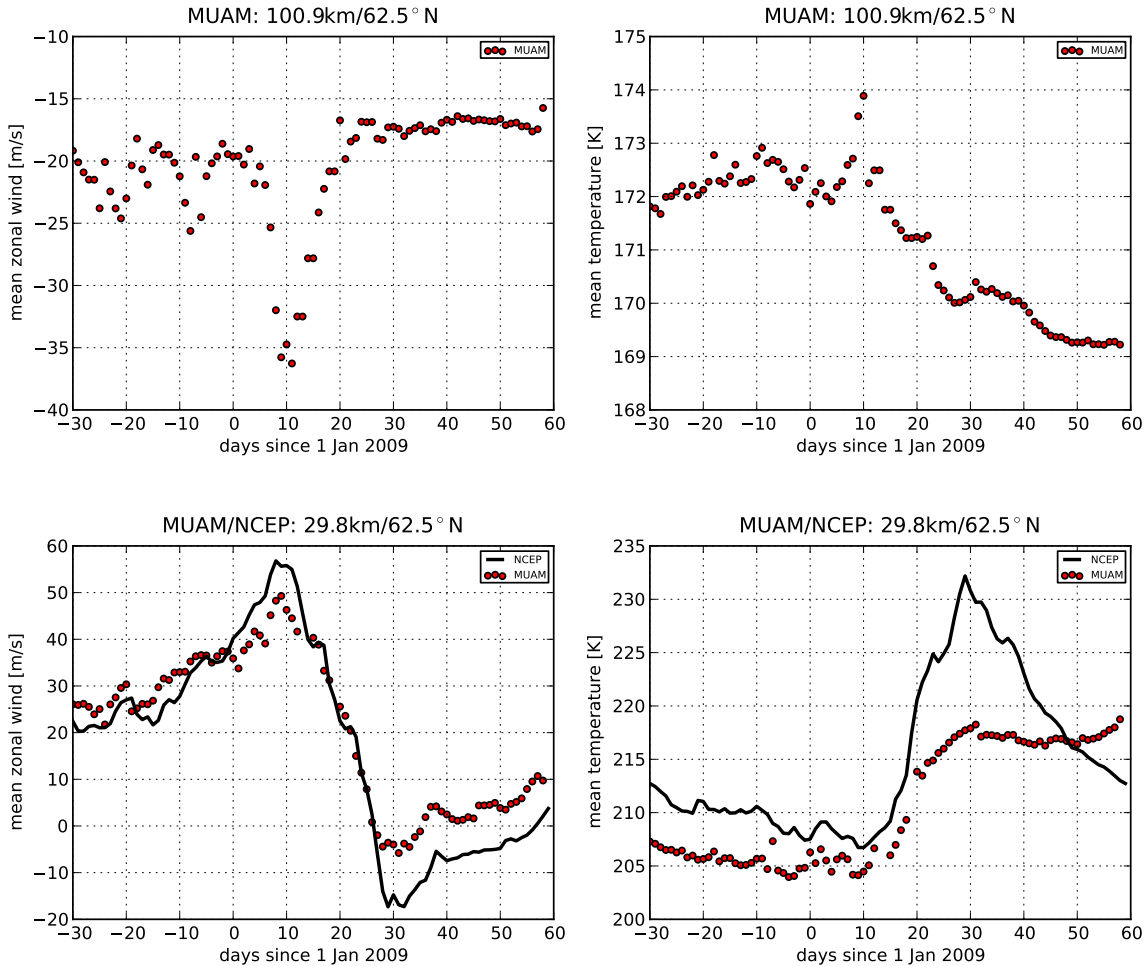


Figure 7: Comparison of mean zonal wind (left) and mean temperature (right) at $62.5^{\circ}\text{N}/30\text{km}$ between NCEP reanalyses (heavy black line) and MUAM simulations (circles) from 2008-12-01 to 2009-02-28 (lower row). The modelled time series at 100km , respectively (upper row).

The importance of the traveling PW forcing in the model is evident in Figure 8 (right panel). It presents one ensemble simulation for the date 2009-01-06. Because the real information of traveling PW are not considered and assimilated to this point, the amplitude of the quasi 16-day wave has been gradually increased (see Table in Fig.8) in order to improve the temperature simulation. The results of the 6 simulations reveal one single member with a 60% stronger amplitude that is able to predict the temperature jumps in near future quite well. In the other simulations temperatures remain below the observations. Only a resonant configuration of externally forced PW provides the breakdown of the polar vortex. Consequently, ensemble means are not helpful, but each member must be individually considered. In order to improve the predictability of SSW events the full

spectrum of PW obtained from reanalyses must be assimilated. Additional simulations per ensemble could increase the probability to find the correct configuration.

PW	16DW	10DW	5DW	4DW
mode	(1,3)	(1,2)	(1,2)	(2,1)
PW1111	0.500E-4	0.37E-4	0.20E-4	0.55E-4
PW2111	0.600E-4	0.37E-4	0.20E-4	0.55E-4
PW3111	0.700E-4	0.37E-4	0.20E-4	0.55E-4
PW4111	0.800E-4	0.37E-4	0.20E-4	0.55E-4
PW4111	0.900E-4	0.37E-4	0.20E-4	0.55E-4
PW5111	1.000E-4	0.37E-4	0.20E-4	0.55E-4

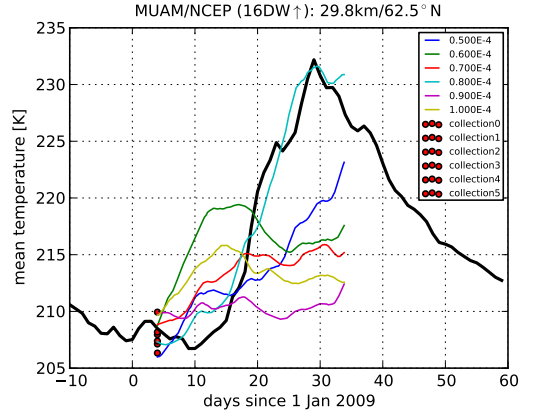


Figure 8: *Example medium-range forecast (30-days) on 2009-01-04 for mean temperature (right) before SSW by changing the amplitude of the externally forced 16-day PW. The table of the used amplitudes of externally forced PW is given on the left.*

One additional model experiment has been carried out for the recent SSW in January 2012. Equivalent to Fig.7, Fig.9 shows the MUAM (circles) and NCEP (solid line) time series from 2011-01-01 to 2012-01-31. Different from the previously discussed example, the warming in late January is accompanied by the zonal wind change at 62.5°N within a few days from 35m/s to 10m/s. The oscillating behaviour of the mean zonal wind in December 2011 is caused by interaction with PW. These are currently not explicitly forced in the performed MUAM simulations. Consequently, the precondition of the warming is not exactly represented in the model. However, the general tendency of the mean zonal wind and temperature can be simulated with the model.

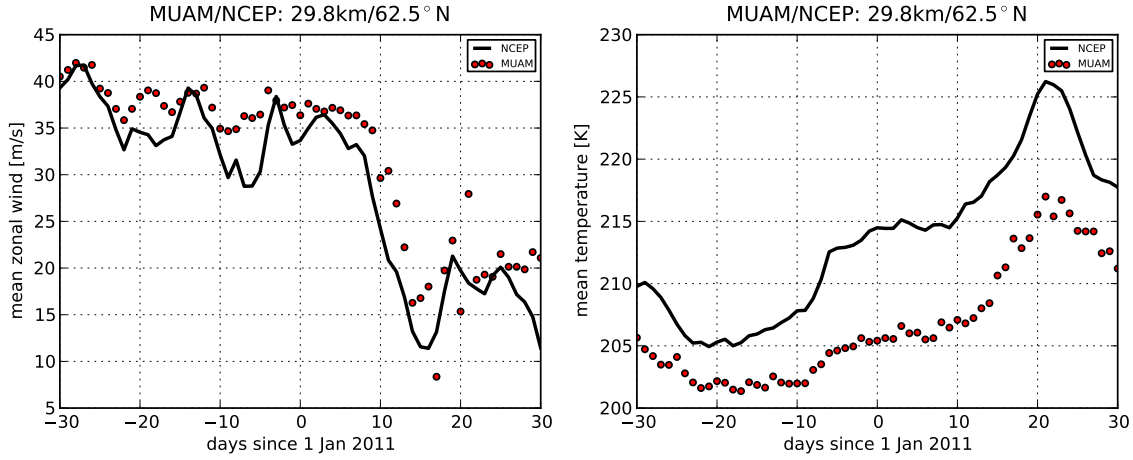


Figure 9: *Comparison of zonal standard deviation in zonal wind (left) and temperature (right) at 62.5°N/30km between NCEP reanalyses (heavy black line) and MUAM simulations (circles) from 2011-12-01 to 2012-01-31.*

5. Conclusions and Outlook

The application of mechanistic circulation models of the middle and upper atmosphere is actually underestimated and in the past, these are only used for studies with the focus on wave propagation and to simulate their consequence of the background and non-linear interactions. The *upper atmosphere research group* at Leipzig Institute of Meteorology (LIM) works on an extended application of this model family in order to investigate the sensitivity of the middle atmosphere in a changing climate on the one hand and to apply such models for quasi real-time simulations up to the upper atmosphere ($\sim 400\text{km}$) on the other hand. Within and acceptable time-frame ensemble simulations can be operated.

This is demonstrated by a simulation of the SSW in January 2009. MUAM is able to reproduce such stratospheric characteristics by a lot of composed single simulations each with a new lower boundary condition, respectively. These provide additional information up to the thermosphere. The predictability of SSW and PW activity and their response to the upper atmosphere will be the most important application in the future.

The performed simulations have shown that MUAM is able to qualitatively reproduce SSW without the assimilation of externally forced travelling PW in the stratosphere, when mean zonal fields are assimilated in the troposphere. However, PW forcing is necessary in order to predict the middle atmosphere circulation more accurate and to extend and tune MUAM for further applications.

References

- Borries, C. and Hoffmann, P. (2010). Characteristics of F2-layer planetary wave-type oscillations in northern middle and high latitudes during 2002 to 2008. *J. Geophys. Res.*, 115:A00G10, doi:10.1029/2010JA015456.
- Cohen, J. and Jones, J. (2011). Tropospheric Precursors and Stratospheric Warmings. *J. Climate*, 24:6562–6572.
- Fritts, D. C. and Vadas, S. L. (2008). Gravity wave penetration into the thermosphere: Sensitivity to solar cycle variations and mean winds. *Annals. Geophys.*, 26:3841–3861.
- Goncharenko, L. P., Chau, J. L., Liu, H.-L., and Coster, A. J. (2010). Unexpected connections between the stratosphere and ionosphere. *Geophys. Res. Lett.*, 37:L10101, doi:10.1029/2010GL043125.
- Haynes, P. (2005). Stratospheric dynamics. *Ann. Rev. Fluid Mech.*, 37:263–293.
- Hinssen, Y., van Delden, A., and Opsteegh, T. (2011). Influence of sudden stratospheric warmings on tropospheric winds. *Meteor. Zeitschrift*, 20(3):259–266.
- Hirooka, T., Ichimaru, T., and Mukougawa, H. (2007). Predictability of stratospheric warmings as inferred from ensemble forecast data: Intercomparison of 2001/02 and 2003/04 winters. *J. Met. Soc. Japan*, 85(6):919–925.
- Hoffmann, P. and Jacobi, C. (2011). Gravity wave influence on middle atmosphere dynamics in model and satellite data. *Rep. Inst. Meteorol. Univ. Leipzig*, 48:33–47.
- Hoffmann, P., Jacobi, C., and Borries, C. (2011). A possible planetary wave coupling between the stratosphere and ionosphere by gravity wave modulation. *J. Atmos. Solar-Terr. Phys.*, accepted, doi:10.1016/j.jastp.2011.07.008.

- Kalnay, E., Kanamitsu, M., Kistler, R., Collins, W., Deaven, D., Gandin, L., Iredell, M., Saha, S., White, G., Woollen, J., Zhu, Y., Leetmaa, A., Reynolds, R., Chelliah, M., Ebisuzaki, W., Higgins, W., Janowiak, J., Mo, K. C., Ropelewski, C., and Wang, J. (1996). The NCEP/NCAR 40-year reanalysis project. *Bull. Amer. Meteor. Soc.*, 77:437–470.
- Kodera, K., Mukougawa, H., and Itoh, S. (2008). Tropospheric impact of reflected planetary waves from the stratosphere. *Geophys. Res. Lett.*, 35:L16806, doi:10.1029/2008GL034575.
- Kuroda, Y. (2008). Role of the stratosphere on the predictability of medium-range weather forecast: A case study of winter 2003-2004. *Geophys. Res. Lett.*, 35:L19701, doi:10.1029/2008GL034902.
- Labitzke, K. (1981). The Amplification of Height Wave 1 in January 1979: A Characteristic Precondition for the Major Warming in February. *Mon. Wea. Rev.*, 109:983–989.
- Limasuvan, V., Thompson, D. W., and Hartmann, D. (2004). The Life Cycle of the Northern Hemisphere Sudden Stratospheric Warmings. *J. Climate*, 17:2584–2596.
- Mukhtarov, P., Andonov, B., Borries, B., Pancheva, D., and Jakowski, N. (2010). Forcing of the ionosphere from above and below during the arctic winter of 2005/2006. *J. Atmos. Solar-Terr. Phys.*, 72:193–205.
- Mukougawa, H. and Hirooka, T. (2007). Predictability of the downward migration of the northern annular mode: A case study for January 2003. *J. Met. Soc. Japan*, 85(6):861–870.
- Mukougawa, H., Sakai, H., and Hirooka, T. (2005). High sensitivity to the initial condition for the prediction of stratospheric sudden warming. *Geophys. Res. Lett.*, 32:L17806, doi:10.1029/2005GL022909.
- Pogoreltsev, A. I., Vlasov, A. A., Fröhlich, K., and Jacobi, C. (2007). Planetary waves in coupling the lower and upper atmosphere. *J. Atmos. Solar-Terr. Phys.*, 69:2083–2101.
- Reichler, T., Kushner, P. J., and Polvani, L. M. (2005). The Coupled Stratosphere-Troposphere Response to Impulsive Forcing from the Troposphere. *J. Atmos. Sci.*, 62:3337–3352.
- Roble, R. G. and Ridley, E. C. (1994). A thermosphere-ionosphere-mesosphere-electrodynamics general circulation model (TIMEGCM): Equinox solar cycle minimum simulations (30-500 km). *Geophys. Res. Lett.*, 21:417–420.
- Schmidt, H. and Brasseur, G. P. (2006). The response of the middle atmosphere to solar forcing in the hamburg model of the neutral and ionized atmosphere. *Space Sci. Rev.*, 125:345–356, doi:10.1007/s11214-006-9068-z.
- Schoeberl, M. R. (1978). Stratospheric Warnings: Observations and Theory. *Rev. Geophys. and Space Phys.*, 16(4):521–538.
- Swinbank, R. and Ortland, D. A. (2003). Compilation of the wind data for the Upper Atmosphere Research Satellite (UARS) Reference Atmosphere Project. *J. Geophys. Res.*, 108(D19):4615.

Wang, H., Fuller-Rowell, T. J., Akmaev, R. A., Hu, M., Kleist, D. T., and Iredell, M. D. (2011). First simulations with a whole atmosphere data assimilation and forecast system: The January 2009 major sudden stratospheric warming. *J. Geophys. Res.*, 116:A12321, doi:10.1029/2011JA017081.

Addresses of the Authors:

Peter Hoffmann (phoffmann@uni-leipzig.de)
Christoph Jacobi (jacobi@uni-leipzig.de)

Institute for Meteorology
University of Leipzig
Stephanstr. 3
04103 Leipzig

Wissenschaftliche Mitteilungen aus dem Institut für Meteorologie der
Universität Leipzig Bd. 50

Long-term trends and decadal variability of upper mesosphere/lower thermosphere gravity waves at midlatitudes

Ch. Jacobi

Institut für Meteorologie, Universität Leipzig, Stephanstr. 3, 04104 Leipzig

Summary

Mesosphere/lower thermosphere (MLT) winds over Germany as measured with a low-frequency spaced receiver system at Collm 1984-2007 have been analysed with respect to variations at the time scales of gravity waves. Background winds are also registered to analyse gravity-mean flow interactions at decadal and interdecadal time scales. In both winter and summer an increasing mesospheric zonal wind jet with time is registered, which is connected with increasing gravity wave variances. At greater altitudes in summer, the mean wind jet trend reverses, and negative trends of gravity wave variances are found. This connection between gravity waves and mean wind is also observed on a quasi-decadal scale: during solar maximum stronger mesospheric zonal wind jets as well as larger gravity wave amplitudes are observed. This results in a solar cycle modulation of gravity waves with larger amplitudes during solar maximum. The connection between gravity waves and mean zonal wind may be explained by wave filtering within linear wave theory, such that stronger mesospheric zonal winds are connected with larger gravity wave amplitudes.

Zusammenfassung

Horizontalwinde, gemessen 1984-2007 mit einem Langwellen-Windprofilersystem in Collm wurden im Hinblick auf Langzeitvariationen kurzperiodischer Schwankungen, die als Signatur von Schwerewellen interpretiert werden können, ausgewertet. Der Grundwind wurde ebenfalls bestimmt, um Welle-Grundstrom-Wechselwirkungen auf der dekadischen und interdekadischen Zeitskala zu untersuchen. Sowohl im Sommer als auch im Winter wurde ein mit der Zeit zunehmender mesosphärischer Jet beobachtet, der mit zunehmenden Schwerewellenamplituden verbunden ist. In größeren Höhen dreht sich der Trend im Sommer um, verbunden mit negativem Trend der Schwerewellenaktivität. Dieser Zusammenhang lässt sich durch Schwerewellenfiltrierung im Rahmen linearer Theorie erklären. Der Zusammenhang zwischen Grundstrom und Schwerewellenaktivität ist auch auf der dekadischen Zeitskala zu sehen: im solaren Maximum sind die mesosphärischen Jets stärker und die Schwerewellenamplituden größer.

1. Introduction

Gravity waves (GWs) play a crucial role in maintaining the dynamics of the mesosphere/lower thermosphere (MLT) region. Their sources are mainly located in the troposphere, and they transport energy and momentum to the middle atmosphere, thus leading to a coupling between atmospheric layers. Changes of GW parameters and

amplitudes are thus connected with changes in atmospheric coupling, and the analysis of long-term trends of GW may give insight into changes of the atmosphere as a whole. Acceleration of the mean flow through GWs mainly occurs in the mesosphere/lower thermosphere (MLT). This region is characterised by the wind reversal, i.e. the change of the mesospheric summer/winter easterly/westerly jets to the lower thermosphere westerly/easterly jets through GW momentum deposition.

The MLT region is accessible to radar wind measurements, although standard methods only deliver limited temporal and thus spectral resolution of GW. On the other hand, however, radar measurements are cost effective, reliable, and independent of weather and thus may provide long-term datasets of background prevailing wind and GW information. Consequently, some effort has been undertaken to analyse GW changes in the MLT also in connection with background wind (Jacobi et al., 2006; Hoffmann et al., 2011). GWs are filtered in the mesosphere through the zonal wind jets. Eastward/westward travelling GWs usually encounter critical lines in the winter/summer mesosphere, where the phase speed equals the wind speed. Therefore, essentially westward/eastward travelling GWs remain in the upper mesosphere. According to linear theory, in the case of wave saturation the GW amplitudes equal the intrinsic phase speed, so that in summer stronger mesospheric easterlies should be connected with larger GW amplitudes, while in winter stronger mesospheric westerlies lead to larger GW amplitudes.

Jacobi et al. (2006) has found a positive correlation of solar activity and GW proxies derived from Collm wind measurements. They attributed this correlation to the possible effect of a solar cycle variation of the mesospheric jet, which is stronger during solar maximum both in winter and in summer. Hoffmann et al. (2011), analysing 22 years of medium frequency radar wind data over Juliusruh, Germany, showed a long-term increase of the mesospheric wind jet and consequently an increase of GW kinetic energy in summer. Both of these findings can be explained by linear theory.

Here, a 24 year dataset of gravity wave proxies is analysed with respect to long-term changes as well as decadal variability, the latter mainly driven by the 11-year solar cycle. The dataset represents an update of the one used by Jacobi et al. (2006). In the following section 2 the method of GW proxy analysis is briefly described. Section 3 presents results of long-term mean prevailing winds and gravity wave proxies. In section 4, analysis of trends and solar cycle dependence is performed using linear least-squares fitting. In section 4 the results are discussed in the light of linear GW theory. Section 6 concludes the paper.

2. LF wind measurements and gravity wave proxy analysis

From 1959-2007, MLT winds have been measured at Collm, Germany, using the spaced receiver method in the low-frequency (LF) range at oblique incidence. Commercial transmitters have been used, one of them located at Zehlendorf near Berlin (frequency 177 kHz), at a distance to Collm of about 165 km. Thus, the reflection point of the sky wave registered at Collm is located at 52.1°N, 13.2°E. Horizontal

winds have been analysed using the similar fade method at 3 receivers at 300 m distance. The applied method makes use of the fact that corresponding maxima or minima of similar fadings of the sky wave are registered at the different receivers with a time delay with respect to each other, which is proportional to the drift velocity of electron density fluctuation patterns at the LF reflection height near 90 km. The method has been described in detail, e.g., by Schminder and Kürschner (1995), and references therein.

The reflection height has been measured from late 1982 to 2007 on 177 kHz through comparison of the phase of the ground wave and sky wave on a side-band frequency near 1.8 kHz (Kürschner et al., 1987). Since the group velocity of radio waves in the lower ionosphere is lower than the speed of light, the resulting altitudes represent virtual heights, and these exceed the real heights by several kilometres. A correction, based on the comparison of semidiurnal tidal phase positions at corresponding heights using meteor radar (Jacobi, 2011) has been applied. Monthly median reflection heights range between 80 and 95 km (Figure 1).

The reflection heights change in a regular manner in the course of one day, since they broadly represent the altitude of a fixed electron density, which equals the critical frequency at oblique incidence. In addition, above all in summer regular data gaps appear during daylight hours (Figure 1, right panel). Therefore, estimates of daily height profiles of winds are not available. Monthly prevailing winds have thus been calculated from one month of half-hourly mean zonal and meridional winds and reflection heights. A least-squares fitting of the prevailing wind and the semidiurnal tide has been applied to these data. There, a second order height-dependence of the regression coefficient has been assumed. The method has been described, e.g., in Schminder and Kürschner (1988) and Jacobi (2011). Right-hand circular polarization of the horizontal tidal components has been assumed (Kürschner, 1991).

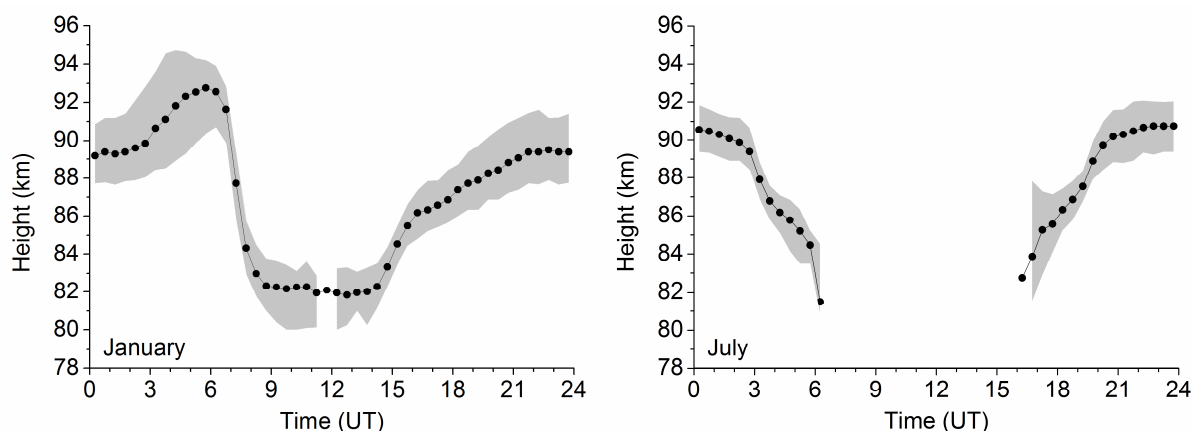


Fig. 1: 1983-2007 median reflection heights in January (left panel) and July (right panel). Upper and lower quartiles are indicated by the shaded area.

Proxies of gravity wave variance in the period range 0.7-3 h (Gavrilov et al., 2001) have been calculated from the squared differences of subsequent half-hourly mean zonal or meridional winds, provided that the height difference of these means does not exceed 1 km. Note that this means that GW proxies at different altitudes preferably refer to different times of the day (see Figure 1). The monthly mean variances have been calculated using data from one month of data within 7 km vertical windows each. The procedure is described in Gavrilov et al. (2001) and Jacobi et al. (2006), but there 10 km height windows and virtual heights have been used.

3. Long-term mean prevailing winds and gravity wave proxies

Long-term mean prevailing winds are presented in Figure 2a for the zonal and in Figure 2b for the meridional component. The results are similar to those that have been presented, e.g., by Jacobi (2011), but with a different time interval under consideration and the height correction applied. Note that the height correction proposed by Jacobi (2011) relies on winter tidal phases only, since during summer the semidiurnal tidal wind gradient is small and thus the respective phases cannot be attributed to a defined altitude. This means that there is an additional uncertainty in the heights attributed to the summer winds.

The zonal prevailing winds show the upward extension of the mesospheric westerly and easterly jets in winter and summer, respectively. The zonal winds are decreasing with altitude, and eventually reversing, however, on a long-term average the zero wind line in winter lies above the region covered by the measurements. The meridional wind (Figure 2b) is mainly southward (negative), but northward in winter below about 83 km. These jets are connected with gravity wave forcing of the zonal mean wind and residual circulation. The long-term means presented in Figure 2 qualitatively agree with results from other measurements (e.g., Hoffmann et al., 2011), but the amplitudes are biased towards smaller values compared with Doppler methods (e.g. Jacobi et al., 2009).

Long-term mean GW variances are presented in Figure 3. Generally, there are maximum amplitudes found in the summer upper mesosphere, and decreasing amplitudes with height. In the upper height gates, there is a tendency for increasing zonal amplitudes in winter. Comparing Figure 2 and Figure 3a, there is a tendency for (i) the southward meridional prevailing wind to maximise in the region of maximum zonal wind shear and (ii) the summer zonal GW variance maximising at regions of maximum zonal prevailing easterly (negative) wind. This would be consistent with linear GW theory, which predicts that, provided the GW are saturated, the GW amplitudes are proportional to the intrinsic phase speed and thus decrease with altitude when the zonal winds decrease or reverse.

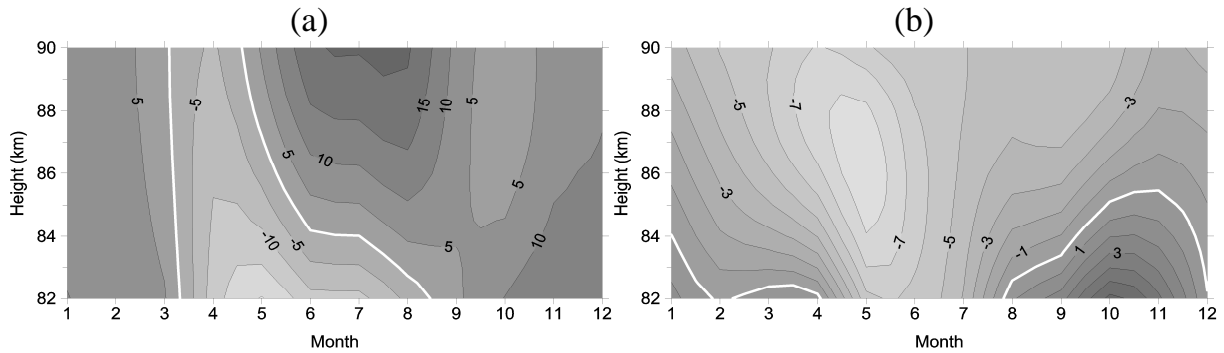


Fig. 2: Height-time cross-sections of the zonal (a) and meridional (b) prevailing wind over Collm. The data are 1984-2006 means based on regression analyses with quadratic height dependence of the coefficients and right-hand circularly polarized tidal components assumed.

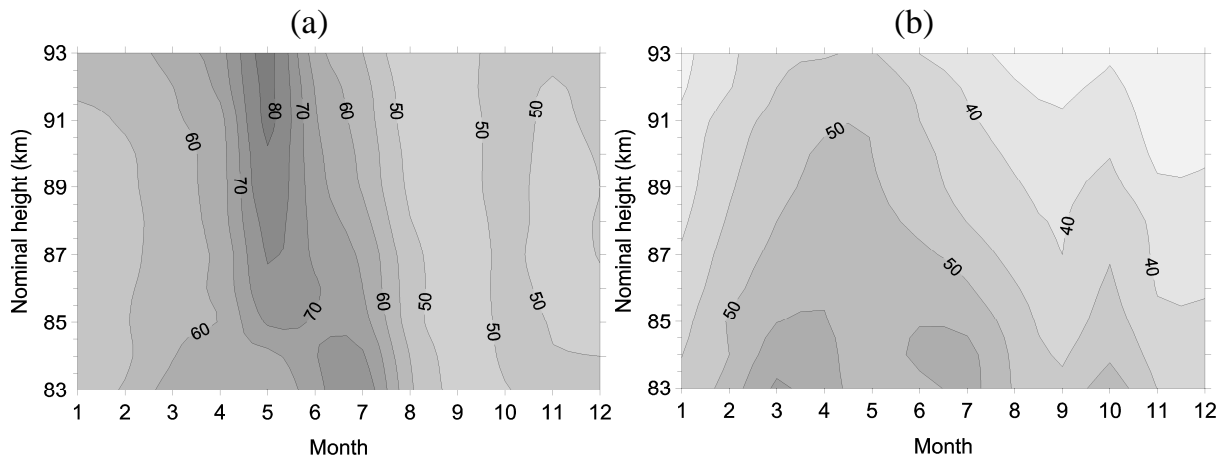


Fig. 3: 10/1983-9/2007 mean zonal (a) and meridional (b) variances over Collm, calculated from half-hourly wind differences (see Jacobi et al., 2006).

4. Long-term trend and solar cycle analysis

Jacobi et al. (2006) have already pointed out that there is an apparent solar cycle effect visible in both zonal and meridional variances over Collm. Regarding long-term changes, Hoffmann et al. (2011) presented long-term (22 years) trends of GW variances over Juliusruh, Germany, and found that summer GW variances have increased during that time interval, connected with an increase of the mesospheric wind jet. Therefore, here the GW variance time series are analysed with respect to a possible long-term change and a solar cycle by:

$$\sigma^2 = a + b \cdot \text{yr} + c \cdot F10.7, \quad (1)$$

with σ^2 as the sum of the zonal and meridional variance and $F10.7$ as the 10.7 cm radio flux given in solar flux units (sfu, 1 sfu = $10^{-22} \text{Wm}^{-2}\text{Hz}^{-1}$). The results, i.e. the coefficients b and c , are presented in Figure 4. For comparison, the same kind of analysis has been applied to the zonal prevailing winds v_{zon} , and the resulting regression coefficients are presented in Figure 5.

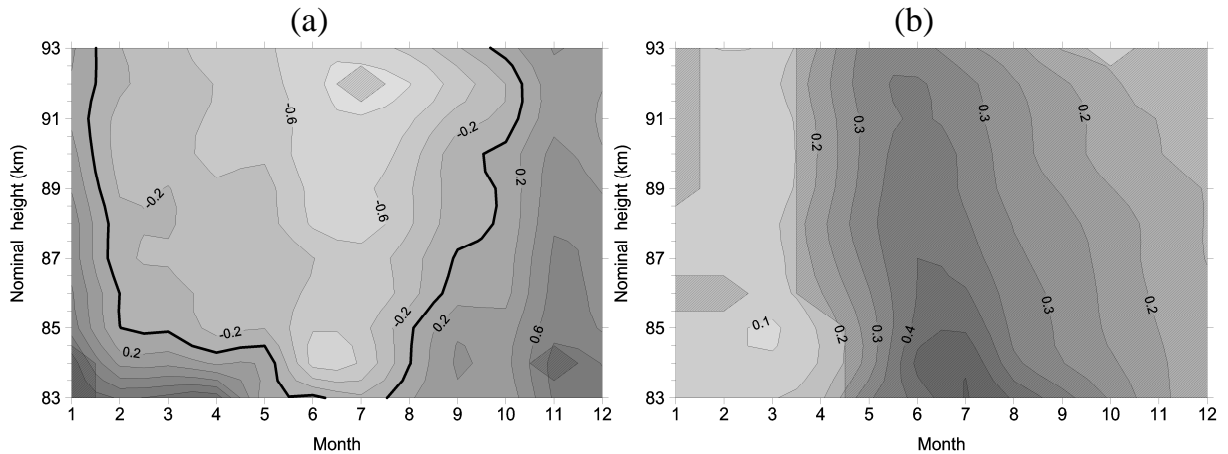


Fig. 4: Linear trend b ($m^2 s^{-2} \text{yr}^{-1}$) (a) and solar effect c ($m^2 s^{-2} \text{sfu}^{-1}$) (b) of GW variance according to a regression analysis $\sigma^2 = a + b \cdot \text{yr} + c \cdot F10.7$ based on 1984-2007 3-monthly means over Collm. Significant values at the 95% level according to a t-test are hatched.

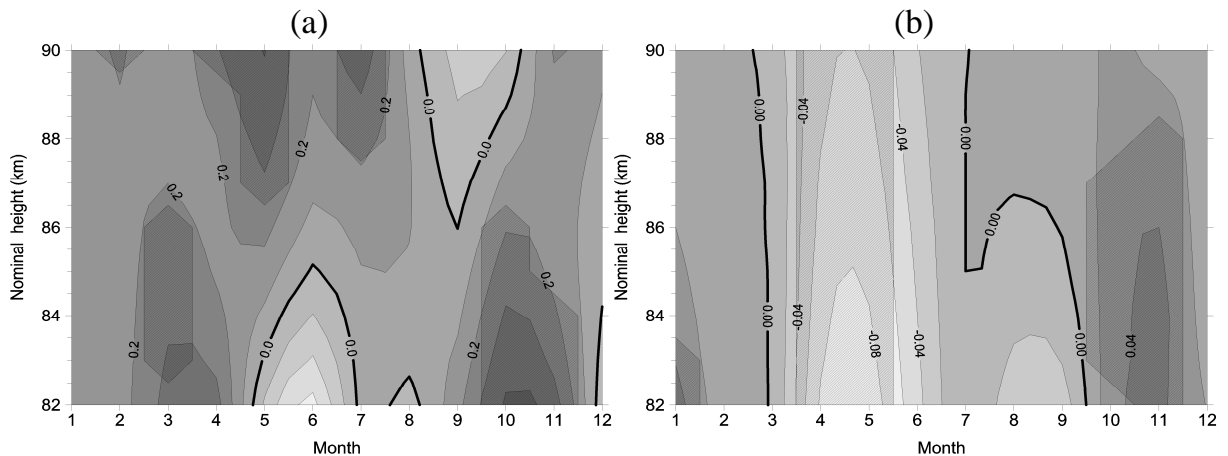


Fig. 5: Linear trend b ($ms^{-1} \text{yr}^{-1}$) (a) and solar effect c ($ms^{-1} \text{sfu}^{-1}$) (b) of the zonal prevailing wind according to a regression analysis $v_{zon} = a + b \cdot \text{yr} + c \cdot F10.7$ based on 1984-2007 3-monthly means over Collm. Significant values at the 95% level according to a t-test are hatched.

One may see from Figures 4b and 5b that the strongest solar cycle signal of the zonal prevailing wind is found in late spring/early summer and early winter. Analysed long-term trends are weaker and mostly insignificant; however, again the strongest signal is seen in late autumn/early winter. Therefore, to illustrate the long-term variability of the mean wind and GW parameters, in Figures 6 and 7 time series of 3-monthly mean σ^2 and v_{zon} are presented for May-July and October-December means at different altitudes. Linear trends, although not always being significant (see Figures 4 and 5) are added.

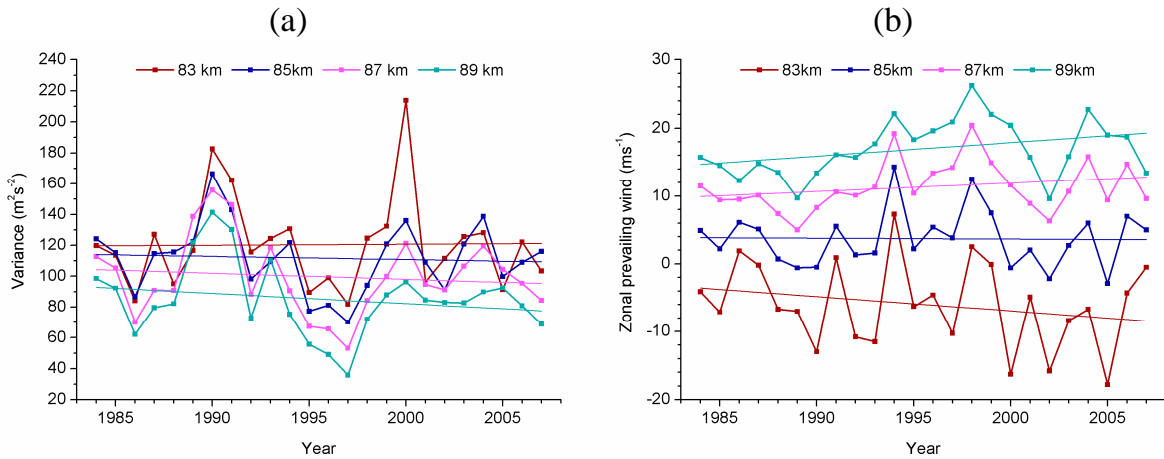


Fig. 6: May-July mean time series of variance σ^2 (a) and zonal prevailing wind v_{zon} (b) over Collm. Variances at 85/87/89 km have been shifted by -10/-20/-30 $m^2 s^{-2}$.

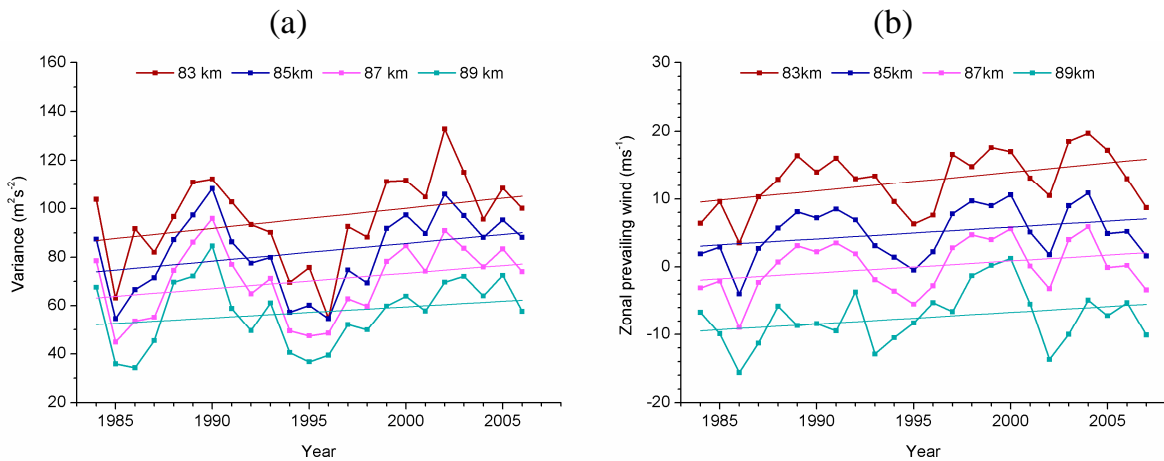


Fig. 7: October-December mean time series of variance (a) and zonal prevailing wind (b) over Collm. Variances at 85/87/89 km altitudes have been shifted by -10/-20/-30 $m^2 s^{-2}$. Mean winds at 85/87/89 km have been shifted by -5/-10/-15 ms^{-1} .

5. Discussion

Hoffmann et al. (2011) have presented negative summer prevailing wind trends, which indicate that the mesospheric summer easterly wind jet becomes stronger with time. This trend decreases with altitude and reverses in the lower thermosphere. One can see from Figure 5a that this behaviour is reproduced in the Collm data, although the trends are weaker and insignificant. Note that the negative wind trends in the lower layers cannot be seen in Figure 6a because this is masked by a strong solar cycle effect. During winter, the zonal wind trends are positive and decreasing with altitude as well. In both cases this means that the mesospheric wind jets have increased during the last 2-3 decades, but this effect decreases or even reverses with altitude.

Stronger mesospheric wind jets in the presence of saturation means larger GW amplitudes. Consequently, positive GW variance trends are expected in both summer

and winter, which is indeed visible in Figure 4a. An exception is found in July, but one may assume that the zero trend line is simply shifted to an altitude just below 83 km. The decreasing zonal mean wind trends lead to decreasing GW intrinsic phase speed trends and thus decreasing variance trends as well. During summer, the trends are mostly negative as expected from the positive prevailing wind trends. The decreasing or reversing zonal wind trends with altitude can be understood as an effect of GW momentum transfer. Stronger mesospheric jets lead to larger GW amplitudes, stronger wave drag and thus decreasing tendencies for the wind trends.

The solar cycle effect is stronger than the long term trend in both prevailing wind and GW variances. Figure 5b shows that the effect is consistent with a stronger mesospheric jet during solar maximum both for summer and for winter. In both seasons the effect decreases with height and partly reverses. Note that the effect is strongest for early summer and early winter. For summer, this may be explained by the decrease of the zero wind line with time. In midwinter the wind field is dominated by stratospheric warmings and strong year-to-year variability, so that significant decadal effects are expected only in early winter.

Stronger mesospheric jets during solar maximum should, according to linear theory, be connected with larger GW variances in both summer and winter. This is indeed visible in Figure 4b. One may also note the decreasing GW solar cycle effect with altitude, which is due to the decreasing zonal wind trend with height.

6. Conclusions

It could be shown from 24 years of zonal wind and GW proxy analyses, that GW variances and mean winds exhibit trends which are qualitatively consistent with each other and may be explained by linear theory and a strengthening of the mesospheric wind jet during the last decades. Note, however, that the long-term trend coefficients presented are in most cases not significant, so that on the one hand the conclusions drawn must be considered as preliminary. On the other hand, however, the results for summer are consistent with medium frequency radar analyses by Hoffmann et al. (2011) so that the overall picture of long-term trends drawn here may be qualitatively correct.

During both summer and winter the mesospheric jets increase with solar activity. These increased jets are connected with increased GW amplitudes. Thus, as is the case with the long-term trends, solar cycle effects of GW may be explained by linear theory.

Still, however, the time series to be analysed are short. Long-term trends can only qualitatively be analysed from slightly more than 2 solar cycles of data. Unfortunately, the Collm LF time series have been terminated after 2007. Although the wind measurements are continued by meteor radar measurements (Jacobi, 2011) it is not yet clear whether trend analyses can be performed using these two datasets without the risk of artefacts leading to possible inhomogeneity of the combined time series.

Acknowledgements

This study was supported by Deutsche Forschungsgemeinschaft under grant JA 836/22-1. F10.7 solar indices have been provided by NGDC through ftp://ftp.ngdc.noaa.gov/STP/SOLAR_DATA/.

References

- Gavrillov, N. M., Jacobi, Ch., Kürschner, D., 2001: Climatology of ionospheric drift perturbations at Collm, Germany, *Adv. Space Res.*, 27, 1779-1784.
- Hoffmann, P., Rapp, M., Singer, W., Keuer, D., 2011: Trends of mesospheric gravity waves at northern middle latitudes during summer, *J. Geophys. Res.*, 116, D00P08, doi:10.1029/2011JD015717.
- Jacobi, Ch., Arras, C., Kürschner, D., Singer, W., Hoffmann, P., Keuer, D., 2009: Comparison of mesopause region meteor radar winds, medium frequency radar winds and low frequency drifts over Germany, *Adv. Space. Res.*, 43, 247-252.
- Jacobi, Ch., 2011: Meteor radar measurements of mean winds and tides over Collm (51.3°N, 13°E) and comparison with LF drift measurements 2005-2007, *Adv. Radio Sci.* 9, 335-341.
- Jacobi, Ch., Gavrillov, N.M., Kürschner, D., Fröhlich, K., 2006: Gravity wave climatology and trends in the mesosphere/lower thermosphere region deduced from low-frequency drift measurements 1984-2003 (52.1°N, 13.2°E), *J. Atmos. Solar-Terr. Phys.*, 68, 1913-1923.
- Kürschner, D., 1991: Ein Beitrag zur statistischen Analyse hochatmosphärischer Winddaten aus bodengebundenen Messungen, *Z. Meteorol.* 41, 1991, 262 - 266.
- Kürschner, D., Schminder, R., Singer, W., Bremer, J., 1987: Ein neues Verfahren zur Realisierung absoluter Reflexionshöhenmessungen an Raumwellen amplitudenmodulierter Rundfunksende bei Schrägeinfall im Langwellenbereich als Hilfsmittel zur Ableitung von Windprofilen in der oberen Mesopausenregion, *Z. Meteorol.*, 37, 322 - 332.
- Schminder, R., Kürschner, D., 1988: Mean winds and tides in the 85- to 110-km region over Central Europe in 1983-1986, *J. Geophys. Res.*, 93, 2493-2497.
- Schminder, R., Kürschner, D., 1994: Permanent monitoring of the upper mesosphere and lower thermosphere wind fields (prevailing and semidiurnal tidal components) obtained from LF Dl measurements in 1991 at the Collm Geophysical Observatory, *J. Atmos. Terr. Phys.*, 56, 1263-1269.

Wissenschaftliche Mitteilungen aus dem Institut für Meteorologie der
Universität Leipzig Bd. 50

Enhanced sporadic E occurrence rates during the Geminid meteor showers 2006-2010

Ch. Jacobi¹, C. Arras²

¹Institut für Meteorologie, Universität Leipzig, Stephanstr. 3, 04104 Leipzig

²GeoForschungsZentrum Potsdam, Department Geodesy & Remote Sensing,
Telegrafenberg, 14473 Potsdam

Summary

Sporadic E (Es) layer occurrence rates derived from GPS radio occultation measurements during the Geminid meteor showers 2006-2010 are compared with meteor rates obtained with the Collm VHF meteor radar. In most years, Es rates increase after the shower, with a short delay of few days. This indicates a possible link between meteor influx and the production of metallic ions that may form Es. However, the correlation between Es rates and meteor flux varies from year to year, indicating that more processes significantly influence Es occurrence also during meteor showers.

Zusammenfassung

Auftretensraten sporadischer E- (Es-) Schichten während der Geminiden 2006-2010 wurden mit Meteorraten aus Radarmessungen am Collm verglichen. Es zeigt sich, dass die Es-Raten kurz nach dem Meteorschauer ansteigen, was auf einen möglichen Zusammenhang zwischen Meteorfluss und der Produktion von Metallionen hinweist, welche Es bilden können. Die Korrelation ist jedoch in verschiedenen Jahren unterschiedlich, so dass auch andere Prozesse die Es-Bildung auch während eines Meteorschauers signifikant beeinflussen.

1. Introduction

Sporadic E (Es) layers are thin regions of enhanced electron density in the lower ionosphere. Their origin is generally accepted to be vertical ion drift convergence due to tidal wind shear (Whitehead, 1960), while the ions are generally accepted to be provided by meteors. There have been long discussions about how sporadic E layers are linked to meteor rates, and the similarity of the seasonal cycles of both meteor rates and Es occurrence rates or strength has given rise to speculations about a cause-and-effect explanation for the sporadic E layer seasonal dependence (Haldoupis et al., 2008).

However, not all features of the seasonal cycle of Es can be found in meteor rates, too. One reason may be that meteor radars, which are usually utilised to provide meteor rate seasonal cycles, only detect part of the incoming meteor flux. Another possible reason is that metallic ions are relatively long-lived and some details of short-term variability is thus not visible in Es. Nevertheless, it is of interest whether short-period meteor events, especially meteor showers, may influence Es rates.

The Geminids are a major meteor shower which forms every year between December 4-17 with its peak activity on December 13. Its parent body is the asteroid 3200 Phaeton. Geminid shower meteors are relatively slow ones with a geocentric velocity of 35 km/s (e.g., Stober et al., 2011a). Consequently, they burn at comparatively low altitudes and are thus well visible in the height range accessible to standard meteor radars (about 80-100 km). The Geminid meteor shower is the major shower visible in radio detections, while other showers are less well visible at least if the analysis is not focused on altitudes above about 100 km.

In this paper we present Es occurrence rates detected by the GPS radio occultation method using FORMOSAT-3/COSMIC data during the Geminid meteor showers 2006-2010, and compare them with meteor rates observed with the VHF meteor radar at Collm. In sections 2 and 3 the methods are briefly presented. In section 4, we present time series of Es and meteor count rates, which are discussed in section 5. Section 6 concludes the paper.

2. Sporadic E analysis using FORMOSAT-3/COSMIC radio occultations

The FORMOSAT-3/COSMIC (FORMOsat SATellite mission-3/Constellation Observing System for Meteorology, Ionosphere and Climate) constellation was launched on April 14, 2006. It consists of 6 satellites, and the main scientific instrument aboard each satellite is a GPS receiver, which applies the GPS radio occultation (RO) technique (e.g., Kursinski et al., 1997) for vertical atmosphere sounding on a global scale. Data and analysis results are made freely available to the international scientific community.

To obtain information on the sporadic E occurrence we use Signal-to-noise ratio (SNR) profiles of the 50 Hz GPS L1 signal according to Wu et al. (2005). Sudden changes in the vertical electron density gradients, as it is usual in presence of a sporadic E layer, appear as strong fluctuations in the SNR above 85 km altitude. The disturbances are caused by signal divergence/convergence which leads to a decrease/increase of the signal intensity at the receiving antenna. The fluctuations are extracted from the background by applying a band pass filter which only accepts disturbances stretching between 1.0 km and 12.5 km height range. If the standard deviation of the SNR in a 2.5 km interval exceeds the threshold of 0.2, the disturbance in the SNR profile is regarded as a significant one. Since Es are very thin layers, the standard deviation should rise abruptly. Consequently, a second criterion is introduced defining that the standard deviation has to rise suddenly by more than 0.14 between two adjacent intervals. In order to avoid using disturbances resulting from other effects than sporadic E, all profiles are excluded from further investigation if the standard deviation exceeds the threshold of 0.2 in more than five intervals. Are all the above mentioned conditions fulfilled, it is considered that the respective profile includes a sporadic E signature. The maximum deviation from the mean profile represents approximately the altitude of the sporadic E layer. For details, see, e.g., Arras et al. (2008, 2009). Note that this method does not provide information about the strength of the Es layer, but only on the occurrence rates in a given time and space interval.

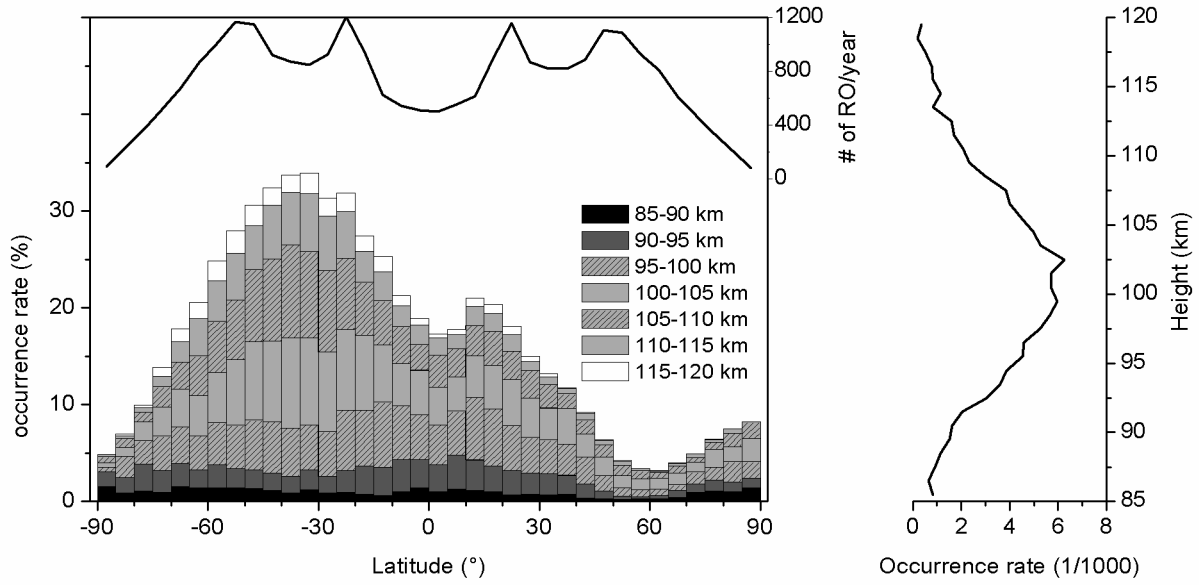


Fig. 1: Left panel: 2006-2010 mean sporadic E occurrence rates per 5km height interval for different 5° latitude bands for the time interval December 4-17 of each year. Right panel: Mean occurrence rates per 1 km height interval for all latitudes between 20°N and 60°N and for the same time interval.

GPS radio occultations are not uniformly distributed around the globe (see also Arras et al., 2009). In the left panel of Figure 1, the total number of occultations per 5 degree latitude interval between December 4 and 17, taken as the average of the years 2006 and 2010, are presented as black line. In the lower part of the panel, the occurrence rates, defined as the number of detected Es divided by the number of occultations in a 5 km height and 5 degrees latitude gate, are presented. One can see that the majority of Es are found in the Southern (summer) hemisphere, but there is also considerable Es activity at lower winter latitudes. The maximum number of Es is found at altitudes slightly above 100 km. Note that there is a tendency for lower altitudes in the winter hemisphere. In the right panel of Figure 1, the 20-60°N mean occurrence rates per 1 km height interval are presented. Most Es are found between 90 and 110 km. Note, however, that this result is partly due to the measurement method, which does not allow to detect Es above ~120 km.

3. Collm meteor radar measurements

At Collm (51.3°N , 13.0°E), a meteor radar is operated at 36.2 MHz since summer 2004. The radar is a commercial SKiYMET all sky system. The radar antenna system consists of one 3-element Yagi transmitting antenna and five 2-element Yagi receiving antennas, forming an interferometer. Peak power is 6 kW. Pulse repetition frequency is 2144 Hz, but effectively only 536 Hz, due to 4-point coherent integration. The sampling resolution is 1.87 ms. The angular and range resolutions are $\sim 2^{\circ}$ and 2 km, respectively. The pulse width is 13 μs , the receiver bandwidth is 50 kHz (see also Stober et al., 2011b).

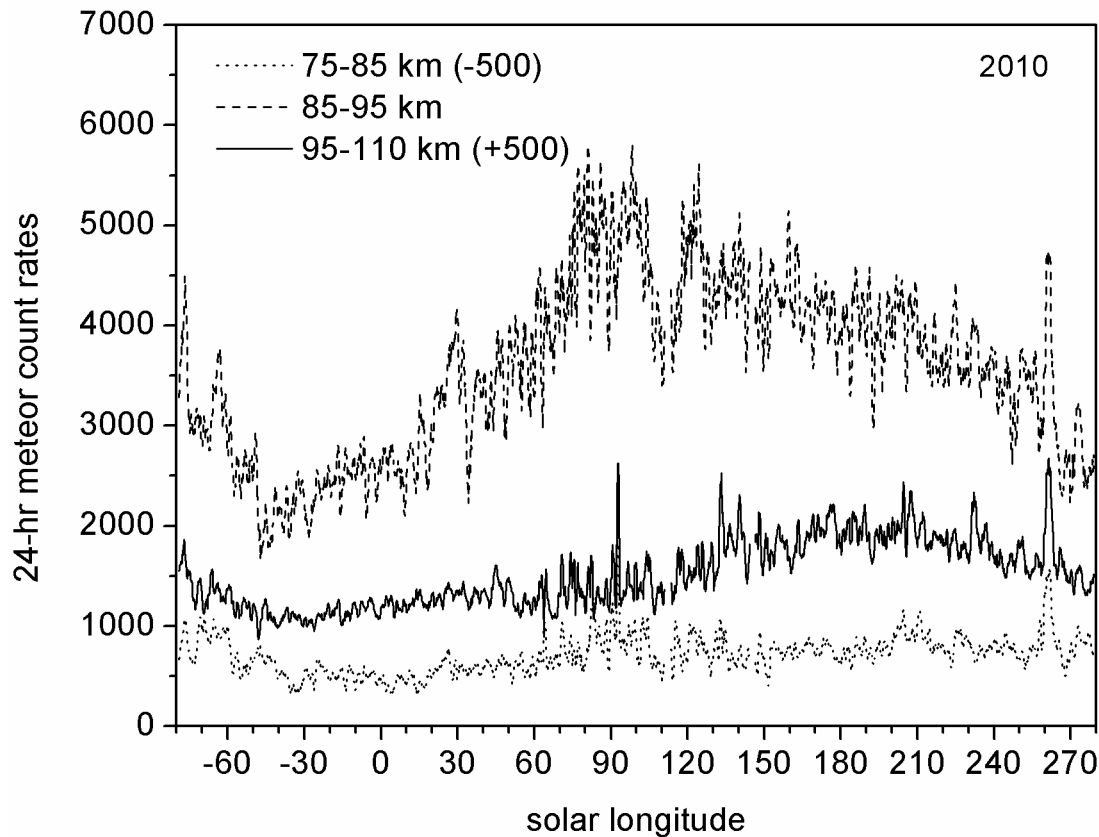


Fig. 2: 24-hr count rates (at 2 hrs step) as measured at Collm during 2010 for 3 different height gates. The curves for the upper and lower height gates have been shifted by +500 and -500 meteors/24 h, respectively.

The radar system was originally designed for wind measurements, but has been used for meteor studies as well. Here we consider zenith angles between 0° and 70° , and distances of up to 400 km from the transmitter. Count rates are taken every 2 hours, and running 24-hr means are calculated.

In Figure 2, meteor count rates for 3 different height gates are presented for the year 2010. The main bulk of meteors is detected at heights between 85 and 95 km. The seasonal cycle is due to the orientation of the radar with respect to the ecliptic plane in the morning hours, when the majority of meteors are detected. This leads to a clear seasonal cycle of fast (and thus high) meteors with minimum in spring and maximum in autumn. This is clearly different from the seasonal cycle of Es. At lower altitudes, where slower meteors are detected, the seasonal cycle is different. It can also be seen that fast meteor showers, like the Leonids (at solar longitude $\lambda = 234^\circ$) is only visible at upper altitudes. Showers of slow meteors, like the Quadrantids in early January or the Geminids in December ($\lambda = 262^\circ$), are visible at each height gate.

In the following, we consider the Geminid meteor shower as one that is visible in each height gate, and which considerably influences meteor count rates. We analyse count rates at altitudes between 75 and 105 km.

4. Results

As an example, in Figure 3 the 24-hr mean meteor count rates and Es occurrence rates are shown for the year 2010. The minimum in spring is visible in every year, followed by an increase and maximum Es and meteor rates in summer. This behaviour led to the conclusion that the annual cycle of meteor rates is responsible for the seasonal cycle of Es (Haldoupis et al., 2008). However, from then on meteor rates remain at an approximately constant level until November, while Es rates decrease. There is an increase of Es rates during December which is, however, not visible in each year.

From Figure 3 one may conclude that the seasonal cycle of meteor rates only partly explains the seasonal cycle of Es. On shorter time scales, however, some peculiarities are found when Es and meteor rates behave in a similar manner. One of them is the enhancement of Es rates in autumn (maximum around day #285) which is accompanied by increased meteor rates. Another one is the maximum of Es rates during the Geminid meteor shower in December. This may lead to the conclusion that strong meteor showers could lead to enhanced Es rates owing the increasing mass flux and thus ion production rate. Thus, in the following Es rates during the Geminid meteor showers will be analysed in more detail.

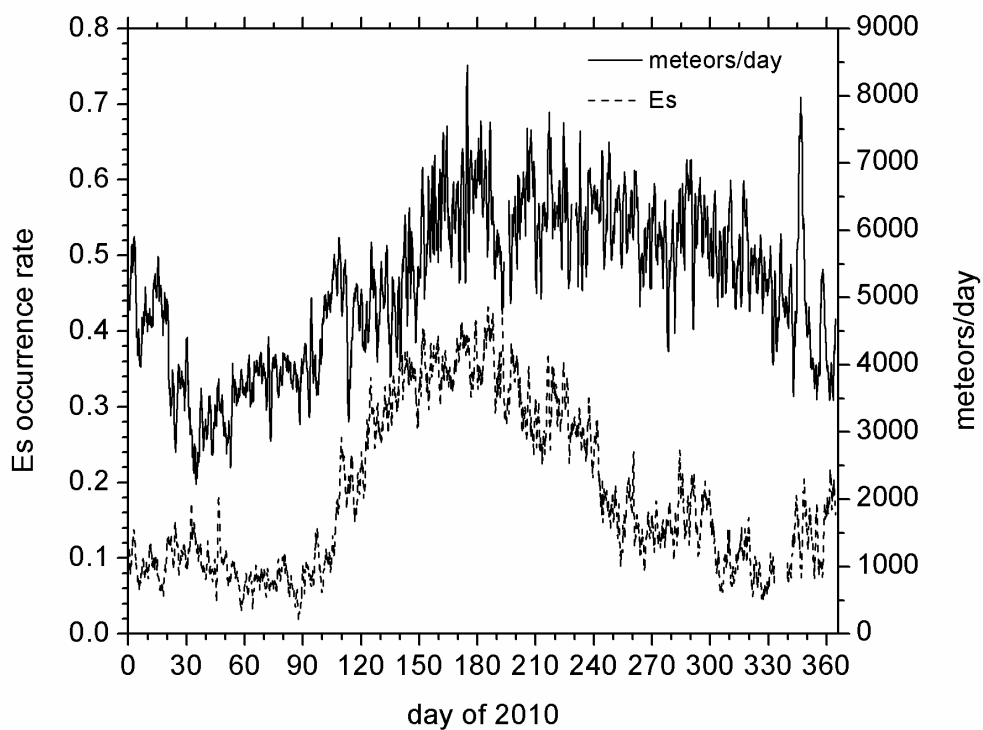


Fig. 3: 24-hr mean Collm meteor count rates and 20-60°N mean sporadic E occurrence rates in 2010.

Two examples of Es rates and meteor rates during different years are presented in Figure 4. We added the 2-hourly mean meteor rates multiplied by 12, to give an impression how the 24-hr means are obtained. Meteor rates have a distinct diurnal cycle with maximum rates in the early morning. This may influence the trends of the 24-hr means presented and definitely makes it difficult to detect the exact time of a meteor shower peak. The Es rates are taken over all longitudes and thus do not show the diurnal cycle. In 2006, the Es rates increase with some delay after the time of increasing meteor rates. Meteor rates after solar longitude $\lambda = 256^\circ$ show a double-peak structure, which is also represented in Es rates. In 2010, however, the picture is not that clear. Es rates undergo an oscillation not very clearly linked to the Geminid shower. However, in most cases an Es increase is preceded by an increase in meteor rates with a time delay of 2 to 3 days, although there is no quantitative connection between the respective maxima.

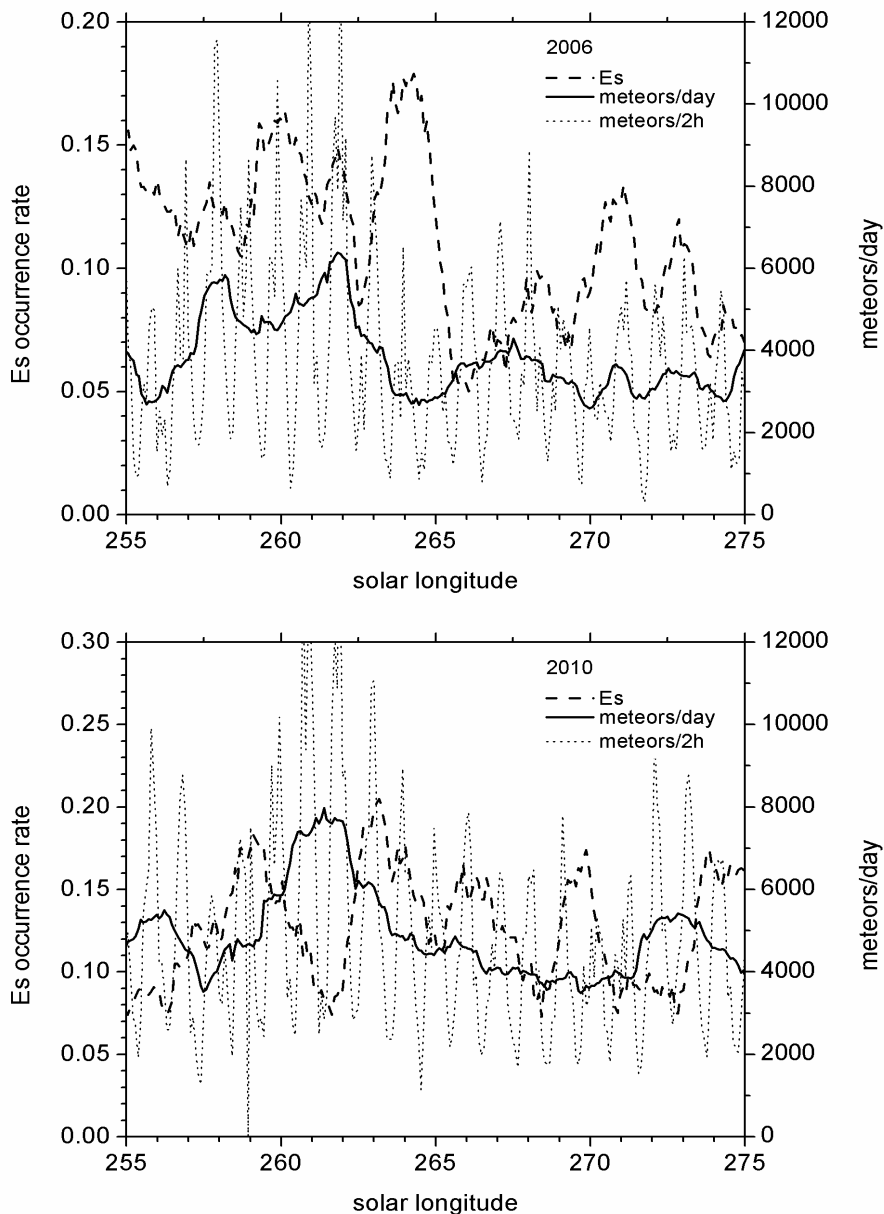


Fig. 4: Daily sporadic E layer occurrence rates in 2006 (top) and 2010 (bottom). Daily mean meteor rates are added, as well as 2-hourly meteor rates multiplied by 12.

On the upper panel of Figure 5, the 5-year averages of Es occurrence and meteor rates are presented together with the standard error. Owing to the small number of years included, the error is partly large due to interannual variability. One can see that on an average, Es rates maximise about 2.5 days later than meteor rates. Note that there is an Es maximum also shortly before the meteor rate maximum, however, this is preceded by a weak enhancement of meteor rates, too. In the lower panel of Figure 5, the cross-correlation functions, taken from data of the days #335-355 of each year, are presented. One can see that the Es-meteor rate correlation in respective years behave in different manners, but there is a tendency for the cross-correlation to maximise at a lag of few days, except for 2007, when the correlation is low at a lag of few days.

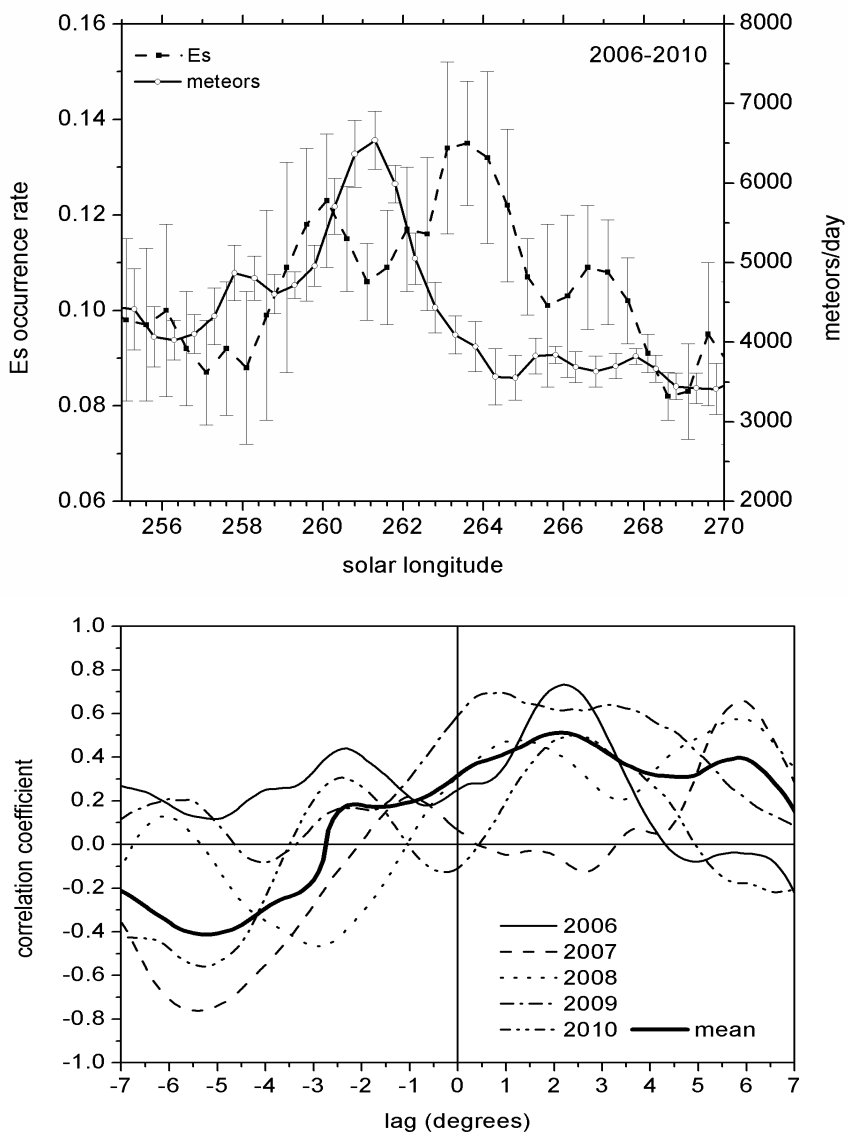


Fig. 5: Upper panel: 2006-2010 mean sporadic E occurrence rates (dashed) and 24-hr mean meteor count rates (solid). Standard errors are added. Lower panel: cross-correlation functions between sporadic E occurrence rates and meteor count rates. Positive lag denotes meteor rate changes heading Es ones.

5. Discussion

Considering the standard error bars of the 5-year mean Es rates, one finds that the enhancement of Es after the Geminid meteor shower is hardly significant. Part of this may be due to the small number of years considered, but definitely there is considerable interannual variability of the Es behaviour, which, as is the case in 2007, during some years does not seem to be strongly influenced by the meteor shower, while in other years a rather strong correlation is found. Clearly, other factors must play a role.

The wind shear theory predicts that at midlatitudes Es are formed at the convergence nodes of vertical ion drift owing mainly to vertical shear of the zonal wind. The main contribution to wind shear is by the semidiurnal tide (SDT), such that the SDT signature is clearly visible in Es (e.g. Arras, 2009). Figure 6 presents SDT zonal wind amplitudes as measured at Collm during December 2006-2010. One can see that the amplitudes are smaller in 2007, 2008, and 2010 compared to 2006 and 2009. Comparing this with Figure 5 reveals that these are the years when the cross-correlation function at lag up to some 5 days does not exceed values of 0.5, while in 2006 and 2009 larger values are found. Although the number of years considered is too small to draw substantial conclusions, and the amplitudes are only a sort of proxy for the wind shear, this nevertheless indicates that SDT wind shear variability may modulate the Es reaction on meteor showers.

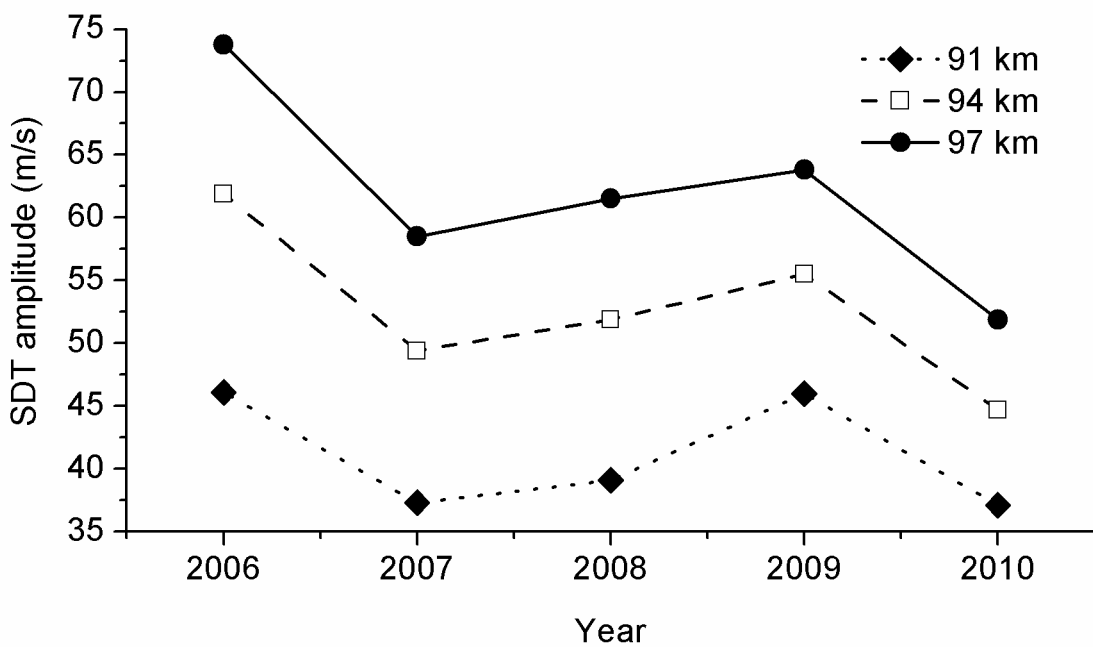


Fig. 6: December mean SDT zonal wind amplitudes as observed at Collm.

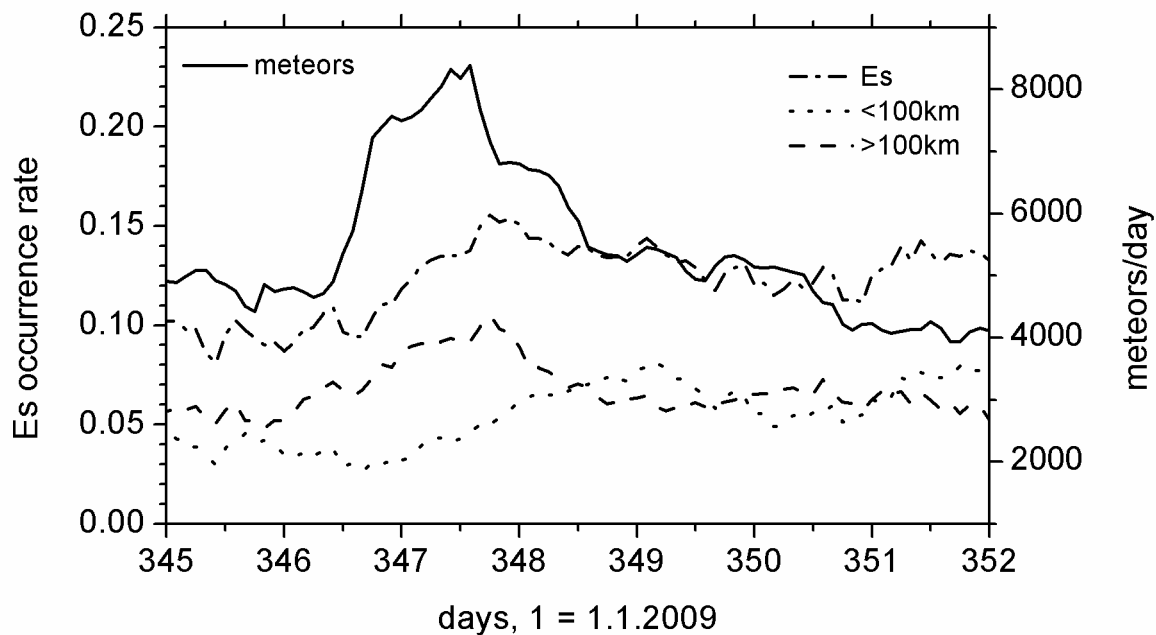


Fig. 7: Time series of meteor rates (solid line), total Es occurrence rates (dash-dotted line) and occurrence rates for heights higher and lower than 100 km (dashed and dotted lines, respectively) in 2009.

One has to note also that possible enhancement of Es after meteor showers should be a rather indirect process. To date there is no proof that after the Geminid shower the concentration of metallic ions is really enhanced, and measurements showed inconclusive and partly contradicting results (Stober, pers. comm.). One reason may be that the mass influx of the Geminids is not very large compared with the sporadic background. Moreover, other slow meteor showers like the Quadrantids do not seem to have considerable influence on the Es rates (see Figure 3).

Another open question refers to the time delay between meteor shower and Es increase. To clarify, in Figure 7 we present the Es occurrence rates above and below 100 km altitude. One can clearly see that above 100 km there is no delay of the Es rates with respect to the meteor rates, while below 100 km the Es rates increase later. This means that, although the Geminid meteors are found in every height accessible to the Collm radar, ions probably first form at greater altitude and are then transported downwards. In total, this leads to a time delay of the overall Es occurrence rate. However, descent speeds of Es layers in winter are usually of the order of 2 km/h (Arras et al., 2009), so that there is another source for delay of the layer formation. Generally, the Es layer descent follows the phase speed of the SDT convergent node at altitudes well above about 100 km, but slows down owing to enhanced ion-neutral collisions (Haldoupis et al., 2006; Christakis et al., 2009).

6. Conclusions

Comparison shows that there is a tendency for sporadic E layer occurrence rates to increase after the Geminid meteor shower. This increase happens with a time delay of 2.5 days on an average. The effect is expressed with variable strength in different

years, in particular during 2007 it appeared to be quite weak. Comparison with SDT amplitudes indicates a possible relationship with changing wind shear magnitudes.

Taking into account the small number of years considered so far and the comparatively large error bars of the mean effect, conclusions should be drawn with care. This is also the case, since supporting evidence of increasing metal concentration after meteor showers is not available. Further studies, both experimental and modelling ones, are required to substantiate the results.

Acknowledgements

We acknowledge UCAR (Boulder, U.S.) and NSPO (Taiwan) for the free and rapid provision of FORMOSAT-3/COSMIC data and related support. Solar longitudes have been calculated based on those provided by the International Meteor Organisation (IMO) on <http://www.imo.net/data/solar>.

References

- Arras, C., Wickert, J., Beyerle, G., Heise, S., Schmidt, T., Jacobi, Ch., 2008: A global climatology of ionospheric irregularities derived from GPS radio occultation. *Geophys. Res. Lett.*, 35, L14809, doi:10.1029/2008GL034158.
- Arras, C., Jacobi, Ch., Wickert, J.. 2009: Semidiurnal tidal signature in sporadic E occurrence rates derived from GPS radio occultation measurements at midlatitudes. *Ann. Geophys.*, 27, 2555–2563.
- Christakis, N., Haldoupis, C., Zhou, Q., Meek, C., 2009: Seasonal variability and descent of mid-latitude sporadic E layers at Arecibo, *Ann. Geophys.*, 27, 923–931.
- Haldoupis, C., Meek, C., Christakis, N., Pancheva, D., Bourdillon, A., 2006: Ionogram height-time-intensity observations of descending sporadic E layers at mid-latitudes, *J. Atmos. Solar Terr. Phys.*, 68, 539–557.
- Haldoupis, C., Pancheva, D., Singer, W., Meek, C., MacDougall, J., 2008: An explanation for the seasonal dependence of midlatitude sporadic E layers. *J. Geophys. Res.*, 112, A06315, doi:10.1029/2007JA012322.
- Kursinski, E.R., Hajj, G.A., Schofield, J.T., Linfield, R.P., Hardy, K.R., 1997: Observing earth's atmosphere with radio occultation measurements using the global positioning system. *J. Geophys. Res.*, 102, 23429-23465.
- Stober, G., Jacobi, Ch., Singer, W., 2011a: Meteoroid mass determination from under-dense trails. *J. Atmos. Solar-Terr. Phys.*, 73, 895-900.
- Stober, G., Singer, W., Jacobi, Ch., 2011b: Cosmic radio noise observations using a mid-latitude meteor radar. *J. Atmos. Solar-Terr. Phys.*, 73, 1069-1076.
- Whitehead, J.D., 1960: Formation of the sporadic E layer in the temperate zones. *Nature*, 188, 567-567.
- Wu, D.L., Ao, C.O., Hajj, G.A., de la Torre Juarez, M., Mannucci, A.J., 2005: Sporadic E morphology from GPS-CHAMP radio occultations. *J. Geophys. Res.*, 110, A01306, doi: 10.1029/2004JA01701.

Proxies to describe ionospheric variability and heating rates of the upper atmosphere: current progress

C. Unglaub, Ch. Jacobi, G. Schmidtke, B. Nikutowski, R. Brunner

Summary

An updated version of the EUV-TEC proxy, describing the total primary ionisation of the upper atmosphere, is calculated from satellite-borne EUV measurements. Regional number densities of the background model atmosphere consisting of four major constituents are taken from the NRLMSISE-00 climatology. Furthermore, a first estimate of a global thermospheric heating rate is calculated from the absorbed energy. For the calculations the Lambert-Beer law is used to describe the decrease of the radiation along their way through the atmosphere. The EUV-TEC proxy is compared against the global mean total electron content (TEC), obtained from vertical TEC maps derived from GPS data. Strong correlations between these indices are found on different time scales. Results show that the EUV-TEC proxy describes the ionospheric variability better than the conventional solar index F10.7, especially at short time scales of days to weeks.

Zusammenfassung

Aus solaren EUV-Spektren wurde eine neue Version des EUV-TEC Proxys berechnet, der die primäre Gesamtionisation der oberen Atmosphäre beschreibt. Dafür wurden die regionalen Teilchendichten der einzelnen atmosphärischen Komponenten einer Modellatmosphäre berechnet. Des Weiteren wurde eine erste Abschätzung der mit der Energieabsorption verbundenen Erwärmungsraten durchgeführt. Zur Berechnung der atmosphärischen Absorption und Ionisation wurde das Gesetz von Lambert-Beer genutzt. Bei einem Vergleich von EUV-TEC mit dem globalen Gesamtelektronengehalt, der aus vertikalen Elektronenprofilen berechnet werden kann, offenbart sich eine starke Korrelation zwischen diesen Indizes auf unterschiedlichen Zeitskalen. Die Ergebnisse zeigen, dass der EUV-TEC Proxy die ionosphärische Variabilität besser beschreibt als der üblicherweise verwendete solare F10.7 Index.

1. Introduction

The EUV wavelength range is defined as the one between 10 nm and 120 nm (ISO, 2007). It is completely absorbed in the earth's atmosphere at altitudes above 50 km, so that it does not reach neither the troposphere nor the Earth's surface. The absorption occurs mainly in the upper atmosphere, i.e. in the thermosphere/ionosphere, and therefore EUV radiation is the most important energy source at altitudes above about 110 km. It interacts with the atmosphere in this region through photodissociation and photoionisation, the latter at wavelengths up to 102 nm, thereby leading to the

development of the planetary ionosphere. However, independent of the respective absorption mechanism EUV radiation finally causes heating of the upper atmosphere.

The total electron content (TEC) of the atmosphere is defined as the integrated electron density along a path under consideration. TEC depends on the solar EUV radiation and the composition of the atmosphere, which is in turn influenced by the EUV radiation variability (e.g., Maruyama, 2010). Thus, ionospheric changes mirror EUV changes. To determine TEC, the ionospheric influence of radio wave propagation paths may be used, because the ionospheric effect on the propagation velocity depends on the radio wave frequency and the ionospheric electron density integrated along the radio wave propagation path. Because GPS satellites emit two frequencies the total electron content along the line of sight between the GPS satellite and a ground-based receiver can be deduced. Subsequently this slant TEC may be converted into a vertical TEC applying an appropriate mapping function. Consequently, measured TEC can be defined as the height integrated electron density between the ground and the satellite orbit (Aggarwal, 2011).

The solar EUV radiation varies on different time scales, where the 11-year Schwabe sunspot cycle causes the primary decadal-scale irradiance variability and the Carrington rotation with an average period of 27 days causes the primary short-term variability. Consequences are strong changes of temperature, composition, density, electron density and ion content of the upper atmosphere. This can affect Low Earth Orbit (LEO) satellites and spacecraft through changes of the atmospheric drag, and may disturb communication and navigation signals (Woods, 2008).

Solar activity is often described by simple indices like F10.7, which is defined as the solar radio emission at a wavelength of 10.7 cm, although the primary factor that controls TEC variations and the variability of thermospheric density and temperature is the solar EUV radiation (Emmert et al., 2010, Maruyama, 2010). Furthermore, a nonlinear relationship between F10.7 and EUV fluxes is found (Liu, L., et al., 2011). Dudok de Wit and Bruinsma (2011) found that the EUV flux in the 26-34 nm band offers a better performance in the thermospheric density reconstruction than other indices like F10.7 or the MgII-index do. Therefore, especially under solar minimum conditions, conventional indices may not well describe the EUV radiation and there is a need for updated EUV indices to describe the ionospheric variability.

In this work we present an updated version of the EUV-TEC proxy (Unglaub et al., 2011), which is intended to explain solar induced ionospheric variability, because the ionospheric electron content is primarily determined by the direct photoionisation induced by the incident solar EUV radiation (Lean et al., 2011). The proxy thus describes ionospheric variability in response to the changing sun. The proxy may be used for space weather monitoring and ionospheric research. EUV-TEC is calculated from satellite-borne instruments measuring the EUV radiation considering the modified composition of the atmosphere which is caused by the EUV radiation. The proxy will be compared with F10.7 and the global mean TEC on different time scales to demonstrate that the EUV-TEC proxy describes the ionospheric variability better than conventional indices like F10.7.

Quasi independent of the absorption mechanism, the absorbed energy is finally transformed into heat, when the atmosphere is considered on a global scale and heat transport processes can be disregarded. Therefore, the calculated absorbed energy, which is a by-product of the EUV-TEC calculation, may be converted into a heating rate when taking into account the atmospheric composition. In the following, this heating rate, named EUV-THERM, is also presented.

2. EUV-TEC and EUV-THERM calculation

EUV spectra with a resolution of 1 nm are available from the Solar EUV Experiment (SEE) onboard the TIMED satellite (Woods et al., 2000, 2005) from February 2002 to date. We use version 10 level 3 products provided by LASP, University of Colorado. In addition, some available spectra from the SOLAR Auto-Calibrating EUV/UV Spectrometers (SolACES) Experiment (Schmidtke et al., 2006a, Nikutowski et al., 2010) are used for comparison.

For the calculation of EUV absorption and ionisation the regional thermospheric composition profiles are needed. Therefore a spherical model atmosphere is assumed around a spherical model Earth's surface. The model atmosphere consists of the four major constituents O, N, O₂ and N₂ and reaches from the ground to an altitude of 1000 km with a resolution of 1 km. To obtain the regional thermospheric composition profiles, first a model sphere with 6370 km radius is assumed surrounded by 1000 spherical shells with 1 km distance representing the atmospheric layers. Then, the points of intersection between the radiation paths of the incoming EUV-radiation and the spherical shells are determined. Subsequently these intersection points are converted into geographical coordinates considering the declination. Thus, the regional thermospheric densities can be calculated by the NRLMSISE-00 model (Picone et al., 2002) for every particular atmospheric layer.

To obtain the EUV-TEC proxy, the primary ionisation is calculated for each atmospheric layer along the radiation paths using the Lambert-Beer law, whereby the required ionisation cross sections are taken from Metzger and Cook (1964) and Fenelly and Torr (1992) and the path lengths through each particular layer can be deduced from the intersection points between the radiation paths and the spherical shells. Integrating the primary ionisation over one day and multiplying with the area where the radiation impacts yields the total ion production rate per day in the atmosphere. Dividing the production rate by the surface of the earth, the EUV-TEC proxy is obtained representing the global mean ion production per day and m² in the atmosphere. In summary, the EUV-TEC calculation is similar to the one described in Unglaub et al. (2011), but there global mean atmospheric densities were considered, while now regional number density profiles are used.

The absorption of the EUV radiation causes heating of the upper atmosphere. Therefore, a first estimate of the heating rate of the atmosphere EUV-THERM can be deduced from the absorbed EUV energy by

$$(1) \quad \Delta T = \frac{\Delta E}{\sum_i n_i \cdot m_i \cdot c_{pi}},$$

where i represents the respective constituents of the model atmosphere. ΔE is the absorbed energy, n_i is the number density, m_i is the mass and c_{pi} is the specific heat capacity of the respective gas i of the model atmosphere. ΔT is calculated for each intersection point between the radiation paths and the atmospheric layers, and subsequently a mean heating rate can be obtained, called EUV-THERM. The calculations are performed with a horizontal resolution of 220 km and a temporal resolution of 4 hours.

3. EUV-TEC results

Photoionisation rates may not be an appropriate dimension to describe electron densities locally, essentially because of the influence of dynamics. However, on a global scale a relatively strong correlation is expected. To check the quality of EUV-TEC as an ionospheric parameter, the proxy has been compared against a global daily mean TEC created from gridded vertical TEC maps recorded with the IGS tracking network (Hernandez-Pajares et al., 2009). To compare the indices, EUV-TEC, TEC, and F10.7 data were normalized by subtracting their mean value between July 2002 and June 2007 and dividing through their respective standard deviation. We chose this time period because EUV datasets from TIMED/SEE are available from February 2002 so a complete solar cycle is not available with a comparatively small data amount during solar maximum conditions that can be used for the normalization. This procedure also ensures that the peculiarities of the recent solar minimum are highlighted, since this time interval is not included in the data used for normalization. As a side effect, however, the average of the subsequently presented proxy data is not zero.

In Fig. 1 the time series of normalized EUV-TEC, normalized F10.7 and normalized global TEC are shown including the EUV-TEC data points based on SolACES measurements. The Figure essentially shows similar features like the one presented in Unglaub et al. (2011). For the SolACES points we apply the normalization of EUV-TEC calculated from TIMED/SEE measurements. There is generally good correspondence between these data points.

To study the solar influence on the atmosphere all data are uncorrected for the earth orbit effect. Comparing the three time series the annual pattern is well visible in both global TEC and EUV-TEC especially during low solar activity. This is, however not the case with the dynamically induced semiannual pattern, which is only visible in TEC.

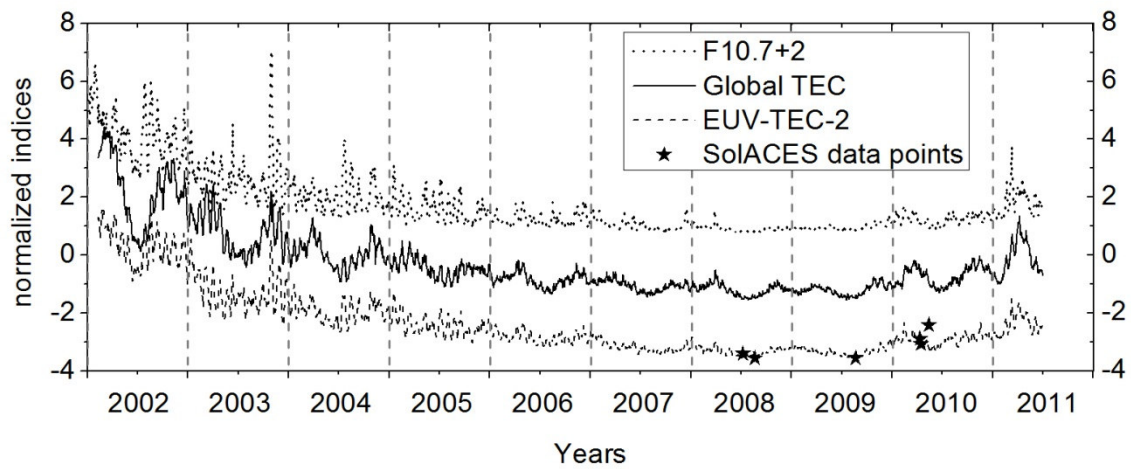


Fig. 1: Time series of the normalized EUV-TEC, global mean TEC and F10.7 from February 2002 to June 2011. The EUV-TEC data points based on SolACES measurements are shown as stars.

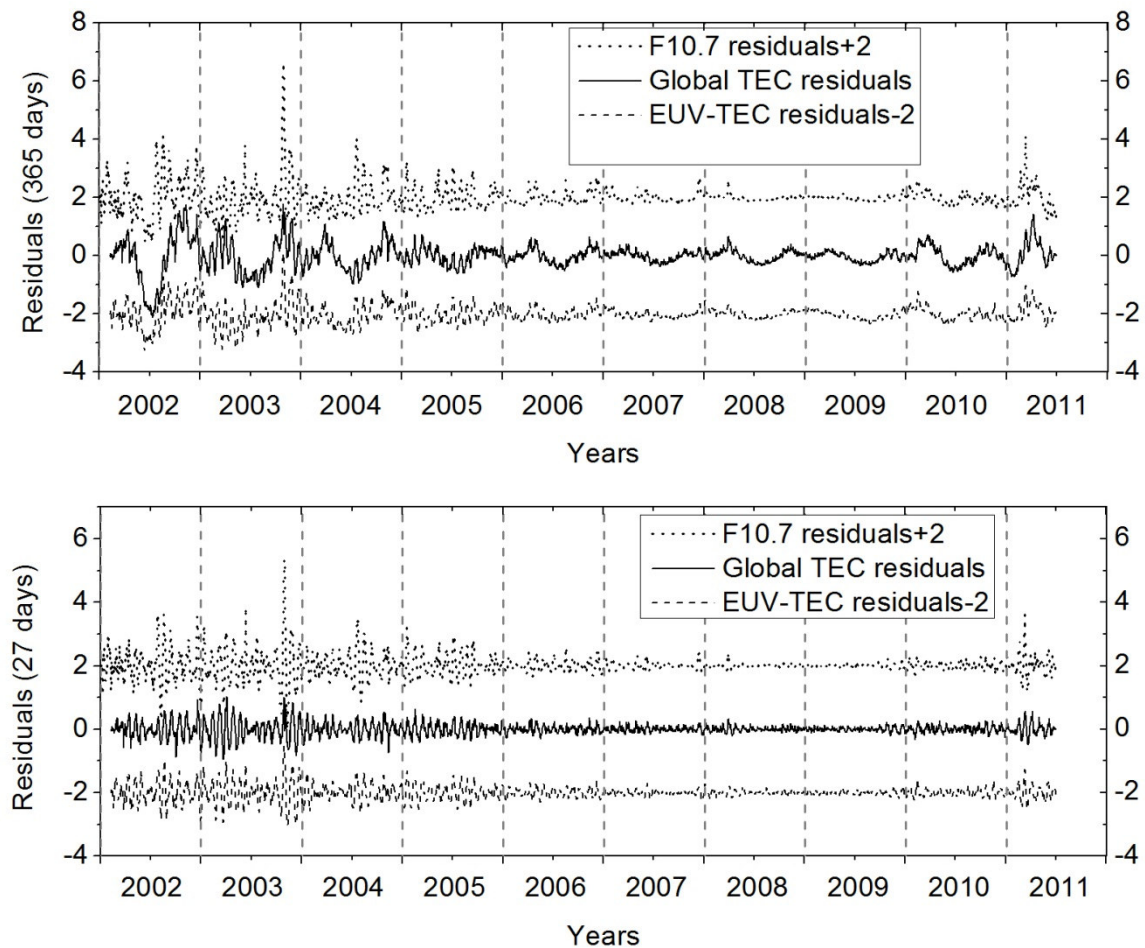


Fig. 2: Time series of residuals of the normalized EUV-TEC, global TEC and F10.7. The 365-days residuals are shown in the upper panel and the 27-day residuals are shown in the lower panel.

The seasonal pattern of EUV-TEC is mainly caused by the earth orbit effect where the earth is in perihelion at the beginning of January and in the aphelion at the beginning of July. Thus, EUV-TEC attains the largest values in the winter and the smallest values in summer. In addition to the earth orbit effect the seasonal pattern of global TEC shows a semiannual oscillation with maxima in spring and autumn. F10.7 shows a seasonal pattern which is caused by the earth orbit effect, too. But in contrast to EUV-TEC and global TEC, F10.7 attains nearly constant values during solar minimum conditions, thus showing a less marked seasonal pattern with a smaller amplitude than global TEC and EUV-TEC do. The dynamically induced semiannual oscillation of global TEC is described neither by EUV-TEC nor F10.7.

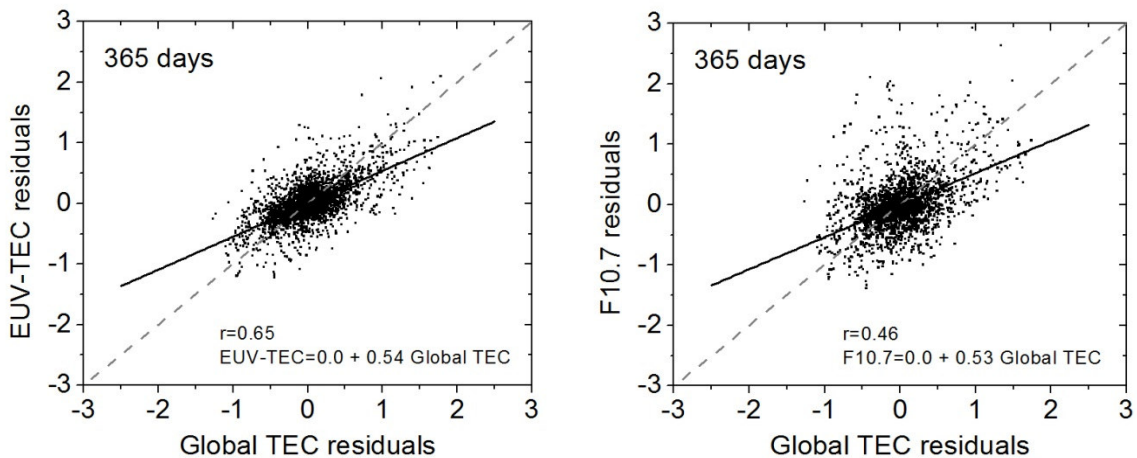


Fig. 3: Residuals after 365 day averaging. Left panel: EUV-TEC vs. global TEC, right panel: normalized F10.7 vs. global TEC.

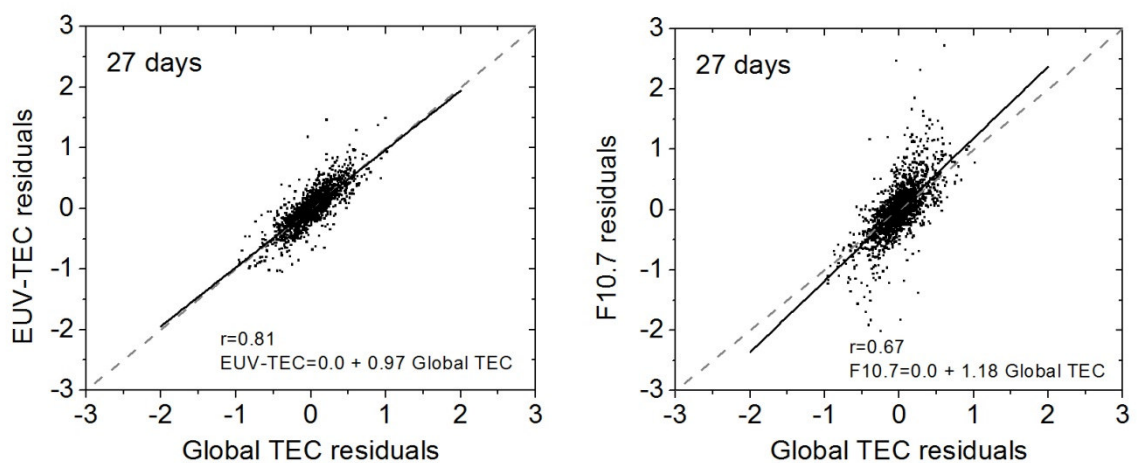


Fig. 4: As in Fig. 3, but for 27 days averaging.

For data from February 2002 to June 2011 there is a strong correlation of the EUV-TEC proxy and global TEC with a correlation coefficient of $r=0.95$, whereas the correlation between F10.7 and global TEC is weaker with a correlation coefficient of $r=0.89$. Thus, EUV-TEC describes the ionospheric variability, including long-term and

short-term variability better than F10.7 during 2002 to 2011. The strong correlations result from the 11-year Schwabe sunspot cycle, because all indices attain smaller values with decreasing solar activity.

To describe short-term variability, running averages over a defined time period (here 365 and 27 days) were calculated and the residuals were analysed. Fig. 2 shows the residuals of the normalized indices EUV-TEC, global TEC and F10.7 after subtracting their smoothed data over 365 days (upper panel) and 27 days (lower panel).

In the left panel of Fig. 3 the residuals (365 days) of EUV-TEC are shown vs. the residuals (365 days) of normalized global TEC. A significant correlation between these indices with a correlation coefficient of $r=0.65$ is obtained. For comparison, the correlation of the normalized residuals (365 days) of F10.7 vs. The normalized residuals (365 days) of global TEC is shown in the right panel of Fig. 3. There is a substantial weaker correlation than between the residuals of EUV-TEC and global TEC with a correlation coefficient of $r=0.46$. Thus, the ionospheric short-term TEC variability and its seasonal pattern are clearly better described by EUV-TEC than by F10.7. Because of the dynamical influence the seasonal pattern of global TEC has larger amplitudes than the seasonal pattern of both EUV-TEC and F10.7 has. This can be seen as well in Fig. 3 through the slope of the regression line smaller than 1.

In the left panel of Fig. 4 the 27 days residuals of EUV-TEC are shown vs. the 27 days residuals of normalized global TEC. There is a strong correlation with a correlation coefficient of $r=0.81$. The right panel of Fig. 4 shows the 27 days residuals of F10.7 vs. the 27 days residuals of global TEC. The correlation coefficient is $r=0.67$. Thus, also in this case the correlation between the residuals of F10.7 and global TEC is considerably weaker than the correlation between the residuals of EUV-TEC and global TEC. Furthermore, it can be seen in Fig. 4 that the amplitudes of the 27 days residuals of EUV-TEC and normalized global TEC are similar whereas the residuals of F10.7 slightly overestimate the residuals of global TEC. Thus, the ionospheric short-term variability up to 27 days, including the Carrington rotation is well described by the EUV radiation and thus can be better described by the EUV-TEC proxy than by the F10.7 index.

4. EUV-THERM: first results

From the EUV absorption rates a global mean thermospheric heating rate is calculated using the globally absorbed energy and the global thermospheric mass and composition by Eq. (1). To this end, we assume that the absorbed energy is finally and quasi-instantaneously transformed into heat, although without including dynamics and a detailed ionospheric model we cannot estimate, where this heating takes place. Thus a temperature signal constant over altitude is calculated as an index contributing to the analysis of the global energy budget.

The time series of the absorbed energy per day is shown in the upper panel of Fig. 5. As expected the absorbed energy time series shows the increasing values of the absorbed energy with increasing solar activity and the seasonal pattern caused by the

earth orbit effect. The corresponding time series of EUV-THERM is shown in the lower panel of Fig. 5. It was calculated using TIMED/SEE measurements in the wavelength range from 5 nm to 104 nm corresponding to the wavelength range where ionisation occurs (up to 102 nm), and thus the trend of the EUV-THERM proxy is very similar to this of EUV-TEC (see Fig. 1) and also following this of the absorbed energy. There is a very strong correlation between EUV-THERM and EUV-TEC and also between EUV-THERM and the absorbed energy with a correlation coefficient of $r=0.99$ in either case.

The very large heating rates of about 6000/14000 K/day during solar minimum/maximum conditions are not realistic for local heating, because we neglected dynamical effects and loss processes.

However, EUV-THERM is based on a physical model representing the solar based thermospheric variations. Because the thermosphere is influenced by both atmospheric (meteorological) and solar signals, EUV-THERM in comparison to some parameter describing total thermospheric variability like density trends (Emmert et al., 2009) can be used to distinguish between solar and meteorological .

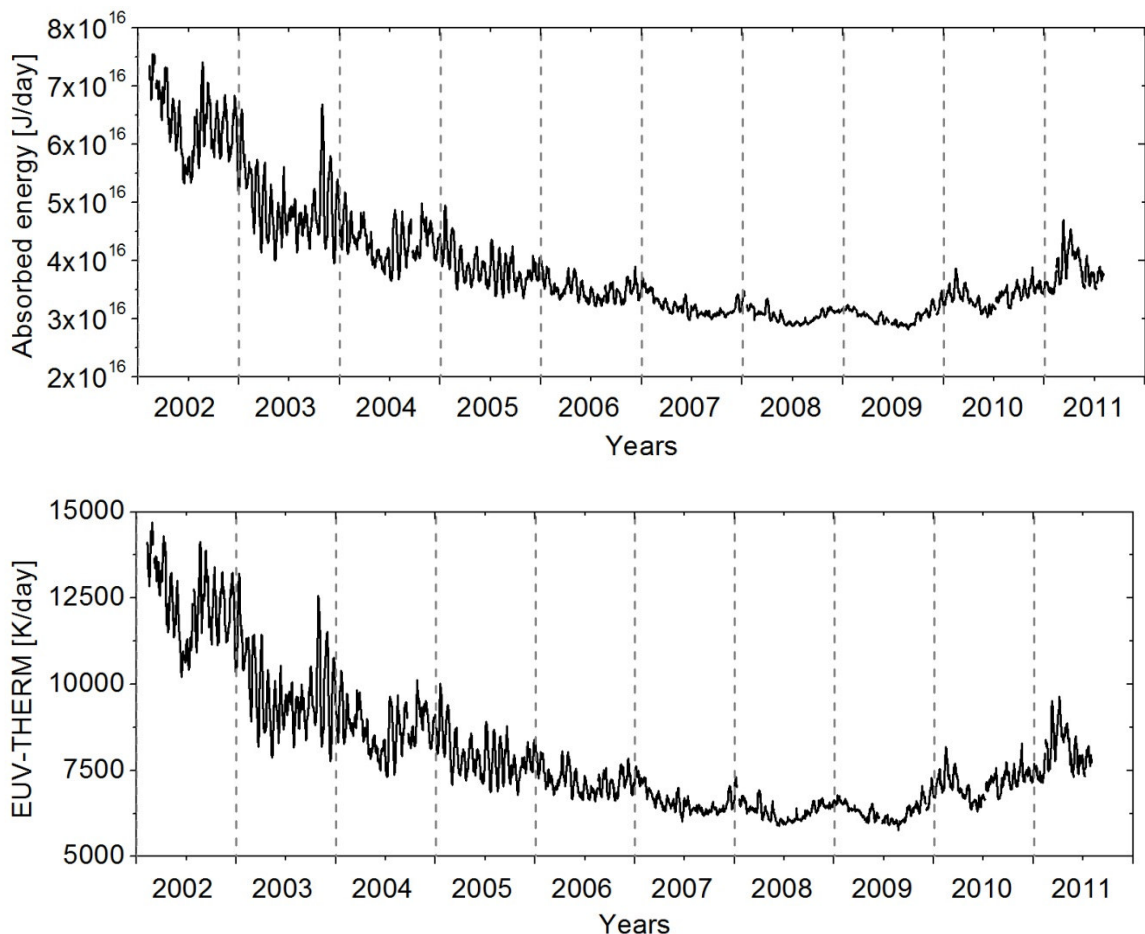


Fig. 5: Time series of the absorbed energy (upper panel) and the EUV-THERM index (lower panel) calculated with EUV measurements in the wavelength range from 5 nm to 104 nm.

5. Conclusions

From satellite-borne EUV measurements two proxies, EUV-TEC and EUV-THERM have been calculated. Here, as an update to earlier data presented in Unglaub et al. (2011) regional thermospheric composition profiles of the background atmosphere are taken from the NRLMSISE-00 climatology. The EUV-TEC proxy, representing a global mean photoionisation rate, describes the influence of the solar EUV irradiance variability on the ionosphere and thus can be considered as an ionospheric proxy useful for the analysis of space weather effects on the upper atmosphere. Comparisons of EUV-TEC with a global mean TEC created from vertical TEC maps show stronger correlations between these indices than between the conventional solar index F10.7 and global TEC especially on short time scales. On the whole, the EUV-TEC proxy performs better than F10.7 to describe ionospheric variability.

The EUV-THERM proxy, a global mean heating rate, is calculated from the absorbed energy in the wavelength range from 5 nm to 104 nm. It represents the solar induced thermospheric heating signal. The values are of the order of magnitude of 10^5 K/day. The proxy may be used to analyse solar effects on the thermosphere and to distinguish, in combination with other data, between solar and meteorological variability of the thermosphere.

Acknowledgements

This research has partly been performed in cooperation between IPM and Universität Leipzig. TIMED-SEE data has been provided by LASP, University of Colorado, through http://lasp.colorado.edu/see/see_data.html. TEC data has been provided by NASA through <ftp://cddis.gsfc.nasa.gov/gps/products/ionex/>. F10.7 indices have been provided by NGDC through [ftp://ftp.ngdc.noaa.gov/STP/SOLAR DATA/](ftp://ftp.ngdc.noaa.gov/STP/SOLAR_DATA/).

References

- Aggarwal, M., 2011: TEC variability near northern EIA crest and comparison with IRI model, *Adv. Space Res.* 48, 1221–1231.
- Emmert, J.T., Picone, J.M., Meier, R.R., 2009: Thermospheric global average density trends, 1967-2007, derived from orbits of 5000 near-Earth objects, *Geophys. Res. Lett.*, 35, L05101, doi:10.1029/2007GL032809.
- Emmert, J. T., Picone, J. M., 2010: Climatology of globally averaged thermospheric mass density, *J. Geophys. Res.*, 115, A09326, doi:10.1029/2010JA015298.
- Fennelly, J.A., Torr, D.G., 1992: Photoionization and photoabsorption cross sections of O, N₂, O₂ and N for aeronomical calculations, *Atom. Data Nucl. Data Tables* 51, 321–363.
- Hernandez-Pajares, M., Juan, J.M., Sanz, J., Orus, R., Garcia-Rigo, A., Feltens, J., Komjathy, A., Schaer, S.C., Krzykowski, A., 2009: The IGS VTEC maps: a reliable source of ionospheric information since 1998, *J. Geod.* 83, 263–275.

- ISO, ISO 21348:2007(E), 2007: Space environment (natural and artificial) - Process for determining solar irradiances, ISO, 12 p.
- Lean, J. L., Meier, R. R., Picone, J. M., Emmert J. T., 2011.: Ionospheric total electron content: Global and hemispheric climatology, *J. Geophys. Res.*, 116, A10318, doi:10.1029/2011JA016567.
- Liu, L., Chen, Y., Le, H., Kurkin, V.I., Polekh, N.M., Lee, C.-C., 2011: The ionosphere under extremely prolonged low solar activity, *J. Geophys. Res.*, 116, A04320, doi:10.1029/2010JA016296.
- Maruyama, T., 2010.: Solar proxies pertaining to empirical ionospheric total electron content models, *J. Geophys. Res.*, 115, A04306, doi:10.1029/2009JA014890.
- Metzger, P.H., Cook, G.R., 1964: A reinvestigation of the absorption cross sections of molecular oxygen in the 1050-1800 $\text{\textnormal{nm}}$ region, *J. Quant. Spectrosc. Radiat. Transfer* 4, 107–116.
- Nikutowski, B., Brunner, R., Jacobi, Ch., Knecht, S., Ehrhardt, C., Schmidtke, G., 2010: SolACES spectrometers onboard the International Space Station (ISS), COSPAR 2010, Bremen, 18-25.7.
- Picone, J.M., Hedin, A.E., Drob, D.P., 2002: NRLMSISE-00 empirical model of the atmosphere: statistical comparisons and scientific issues, *J. Geophys. Res.*, 107, 1468, doi:10.1029/2002JA009430.
- Schmidtke, G., Brunner, R., Eberhard, D., Halford, B., Klocke, U., Knothe, M., Konz, W., Riedel, W.-J., Wolf, H., 2006a: SOL-ACES: Auto-calibrating EUV/UV spectrometers for measurements onboard the International Space Station, *Adv. Space Res.*, 37, 273-282.
- Schmidtke, G., Fröhlich, C., Thuillier, G., 2006b: ISS-SOLAR: Total (TSI) and spectral (SSI) irradiance measurements, *Adv. Space Res.*, 37, 255-264.
- Unglaub, C., Jacobi Ch., Schmidtke G., Nikutowski B., Brunner R., 2011: EUV-TEC proxy to describe ionospheric variability using satellite-borne solar EUV measurements: first results, *Adv. Space Res.* 47, 1578–1584.
- Woods, T. N., Bailey, S., Eparvier, F., Lawrence, G., Lean, J., McClintock, B., Roble, R., Rottmann, G. J., Solomon, S. C., Tobiska, W. K., White, O. R., 2000: TIMED Solar EUV Experiment, *Phys. Chem. Earth (C)*, 25, 393–396.
- Woods, T. N., Eparvier, F., Bailey, S., Chamberlin, P., Lean, J., Rottmann, G. J., Solomon, S. C., Tobiska, W. K., Woodraska, D. L., 2005: Solar EUV Experiment (SEE): Mission overview and first results, *J. Geophys. Res.*, 110, A01312, doi:10.1029/2004JA010765.
- Woods, T. N., 2008: Recent advances in observations and modeling of the solar ultraviolet and X-ray spectral irradiance. *Advances in Space Research*, 42:895–902.

Addresses of authors

- C. Unglaub, Ch. Jacobi: Institut für Meteorologie, Universität Leipzig, Stephanstr. 3, 04104 Leipzig
- G. Schmidtke, B. Nikutowski, R. Brunner: Fraunhofer-Institut für Physikalische Messtechnik (IPM), Heidenhofstraße 8, 79110 Freiburg

Measuring saltation and creep with high spatial and temporal resolution

Hans-Jürgen Schönfeldt

Summary

Measurement of aeolian sand transport rates with high temporal and spatial resolution is crucial for further progress in developing proper sand transport equations, in testing and developing numerical models of sand movement by wind, and in the modelling of sand dunes, ripples and other aeolian forms. Observational research on the behaviour of sand grains in natural sediments under natural conditions is presented herein.

This study uses the established measuring principle of a Saltiphone (Spaan and Van den Abeele, 1991) and a webcam commonly used in personal computers. The webcam frame transfer is triggered every 0.1s by a sonic anemometer. Consecutive frames are compared and analysed in real-time by a computer program. The webcam signal also provides the number of moving grains also the grain size of the moving grains and this for every grain that has moved in a time step of 0.1s.

Problems to determine the transport near the thresholds and the difficulties in the determination of thresholds from measured mean transport rates are discussed, and proposals for dealing with the problems are made. An iterative technique to determine the thresholds of transport (ITT) from high resolution transport measurements is presented. In this way, constitutive equations for sand transport in terms of wind speed can be tested. If viable, they can be employed to infer estimates for the thresholds by minimising the root-mean-square error between measured and calculated transport data. Alternatively, the fluid and impact thresholds for aeolian sand transport are determined from the field measurements on a beach by analysing the onset and breakdown of saltation in gust and lull intervals (GLM) of rising and falling wind speeds, respectively.

Zusammenfassung

Für den weiteren Fortschritt bei der Entwicklung geeigneter Sandtransportgleichungen sowohl der Entwicklung und dem Test numerischer Modelle des durch den Wind verursachten Sandtransports und bei der Modellierung von Sanddünen, Sandrippeln und anderen äolischen Formen ist die Messung der äolischen Sandtransportrate mit hoher zeitlicher und räumlicher Auflösung Voraussetzung. Untersuchungen unter natürlichen Bedingungen über das Verhalten der Sandkörner im natürlichen Sediment werden vorgestellt.

Diese Studie beruht auf dem etablierten Messprinzip des Saltifons (Spaan and Van den Abeele, 1991) und benutzt eine handelsübliche Webcam, wie sie auch an einen PC angeschlossen werden kann. Der Webcam Frame Transfer wird durch ein Ultraschallnemometer jede 0.1s ausgelöst. Aufeinander folgende Bilder werden in Echtzeit durch ein Computerprogramm analysiert. Das Webcam Signal liefert sowohl die Anzahl der Körner als auch deren Größe, die sich im Abtastschritt von 0.1s bewegt haben.

Probleme der Transportberechnung nahe der Transportschwellen und Schwierigkeiten in der Bestimmung der Schwellen aus den gemessenen Transportraten werden diskutiert und es werden Vorschläge zum Umgang mit diesen Problemen gemacht. Es wird eine iterative Technik zur Bestimmung der Transportschwellen (ITT) aus hochaufge-

lösten Transportmessungen vorgestellt. Damit lassen sich Vorhersagegleichungen für den Sandtransport als Funktion der Windgeschwindigkeit testen. Wenn diese Vorhersagegleichungen sich als brauchbar erweisen, können diese zur Bestimmung der Schwellen durch Minimieren der mittleren quadratischen Abweichung zwischen gemessenen und berechneten Transport dienen. Alternativ werden die „fluid“- und „impact“- Schwellen des äolischen Sandtransports aus Feldmessungen an einem Strand durch Analyse des Einsetzens und des Abklingens der Saltation (GLM) in Windböen und Flauten bestimmt.

Introduction

A number of equations have been proposed, which link horizontal sand fluxes with wind velocities (Bagnold 1941; Zingg 1953; Williams 1964; Kawamura 1964; Owen 1964; Gillette and Goodwin 1974; Gillette 1979; Lettau and Lettau 1978; White 1979; Sørensen 1985; Gillette and Stockton 1989; Leys and Raupach 1991; Shao et al. 1993; Stout and Zobeck 1997; Zheng et al. 2003, 2006; Stout 2004; Leenders et al. 2005). Bowker et al. (2007) compared the sand flux of model predictions with field measurements and then assessed the sensitivity of the simulations to several aspects such as the formulation of the sand flux equation and the specific value of the threshold velocity, u_{*t} . They used the transport equations of Kawamura (1964) and White (1979) (Eq. (1)) and of Owen (1964) (Eq. (2)), with Q as the transport rate, u_* as the friction velocity and A , A_1 as constants. Kawamura and White's equation has a correction term reciprocally proportional to the friction velocity, but the difference between the measured and simulated data are nevertheless significant.

$$Q = A_1 u_*^3 \left(1 - \frac{u_{*t}^2}{u_*^2} \right) \left(1 + \frac{u_{*t}}{u_*} \right) \quad \text{Kawamura (1964), White (1979)} \quad (1)$$

$$Q = A u_*^3 \left(1 - \frac{u_{*t}^2}{u_*^2} \right) \quad \text{Owen (1964)} \quad (2)$$

Eq. (1) and Eq. (2) underestimate the measurement during the storm-event 1 in 2003 (see Bowker et al., 2007), and on storm 5 in 2003 the equations overestimate the measurements up to 100%. Storm 1 in 2004 cannot be predicted with this method. In the problem with the equations is the prediction of threshold friction velocity. Direct measurements of threshold friction velocity with a Sensit instrument have not solved the problem (Bowker et al., 2007). Both Stout (1998), with an experimental approach and Schönfeldt (2003) with a theoretical approach found that the averaging time of wind speed measurement affects the observed time fraction equivalence threshold.

Our current understanding of this problem lies in the nonlinearity of the transport equations with regard to friction velocity and in the use of different time scales for determining the variables. A simple reassessment of the problem as Schönfeldt (2003) has done leads to the conclusion that a transport equation must include the turbulence intensity of the wind, I , that is the relation of standard deviation in the wind, σ , to the mean wind speed \bar{u} . Mean wind speed equalling the threshold does not lead to transport in Eq. (1) and (2). Eqs. (1) and (2) provide negative transports for $u_* < u_{*t}$ and must actually be multiplied by the Heaviside function $H(u_* - u_{*t})$, with $H(x) = 0$ for

$x < 0$ else $H(x) = 1$. Introducing this, as well as using a Gaussian distribution for the wind (Stout and Zobeck, 1997), one gets the following simple analytical expression for the expected value of the wind during saltation (if $\bar{u} = u_{*t}$), where the function $\mathcal{E}\{x\}$ denotes the expectation value of x ,

$$\mathcal{E}\{u\} = u_s = \frac{1}{\sigma\sqrt{2\pi}} \int_{u_{*t}=\bar{u}}^{\infty} u \cdot \exp\left(-\frac{(u-\bar{u})^2}{2\sigma^2}\right) du = \frac{1}{2} \bar{u} + \frac{\sigma}{\sqrt{2\pi}} . \quad (3)$$

From Eq. (3) it is concluded that there is a conflict in the models. The expected value of the wind responsible for transport is not the mean of the wind, and sand will be transported; however, Eqs. (1) and (2) provide no transport. Unfortunately Eq. (3) cannot be inserted mathematically into Eqs. (1) and (2). The situation is, of course, more complicated. An analytical discussion of the Bagnold (1941) transport equation in relation to wind variability was done by Sørensen (1997). Following Jacksen (1997), the instantaneous transport is more linear and quadratic in u , not cubic. It can be stated

$$Q = a \cdot \mathcal{E}\{(u - u_{*t})\} + b \cdot \mathcal{E}\{(u - u_{*t})^2\} . \quad (4)$$

Eq. (4) is analytically resolvable. Analogous to Eq. (3), the expectation value of Q (Eq. (4)) involves in addition to the mean wind speed terms of σ , σ^2 and mixed terms.

This analytical issue will not be pursued: the problem is yet more complex. According to Bagnold (1941), there are two thresholds for saltation: the fluid threshold, which is defined as the wind speed at which particles start moving due to the forces of wind only, and the impact threshold, which is the speed at which the combined action of wind forces and saltation impacts can only sustain movement. This means that grain movement by a fluid has a characteristic hysteresis and is strongly nonlinear. The saltation process depends on how frequently the wind speed exceeds the fluid threshold and then how long the wind speed stays over the impact threshold. The same mean wind speed may provide different transport rates, depending on statistical parameters of the wind. Schönfeldt (2008, 2011) has introduced these two thresholds in a transport equation of Sørensen (2004) for homogeneous sand of sizes greater than 125 μm , based on measurements of Iversen and Rasmussen (1999)

$$Q = \frac{\rho}{g} u_{*t}^3 \left(\mathcal{W}^2 + \beta V - \gamma - \beta \frac{1}{V} \right) , \quad (5)$$

where $V = u_{*t} / u_{*t}$ denotes the dimensionless friction velocity or, transformed to the short time scale, the dimensionless saltation scaled wind speed at arbitrary height z well above the saltation height ($V = u(z) / u_t(z)$), ρ the density of the air, g the acceleration of gravity and β and γ are grain diameter-dependent constants. In this transport equation derived from wind tunnel data, Schönfeldt (2008) replaced the powers of V by its expected values during saltation, and the non-written Heaviside function in the transport equation by the probability of saltation F . The expected values are functions of V , relation of the mean wind speed to the impact threshold, turbulence intensity I and r_I , and autocorrelation of the wind at lag one Δt .

$$Q = \frac{\rho}{g} u_{*t}^3 F(V, I, r_1) \left(\gamma \epsilon \{V_s^2\} + \beta \epsilon \{V_s\} - \gamma - \beta \epsilon \left\{ \frac{1}{V_s} \right\} \right) \quad (6)$$

Near the thresholds, transport based on wind with a distribution function can deviate up to 100% from the transport calculated with the same constant mean wind speed. In Figure 1, transport Q is shown as function of the mean scaled wind speed with the parameters I and r_1 , based on the Sørensen (2004, Eq. (5)) equation and a Gaussian distributed wind. Note that all these curves are based on the same scaled impact threshold $V_i = 1$, and, according to Bagnold (1941),

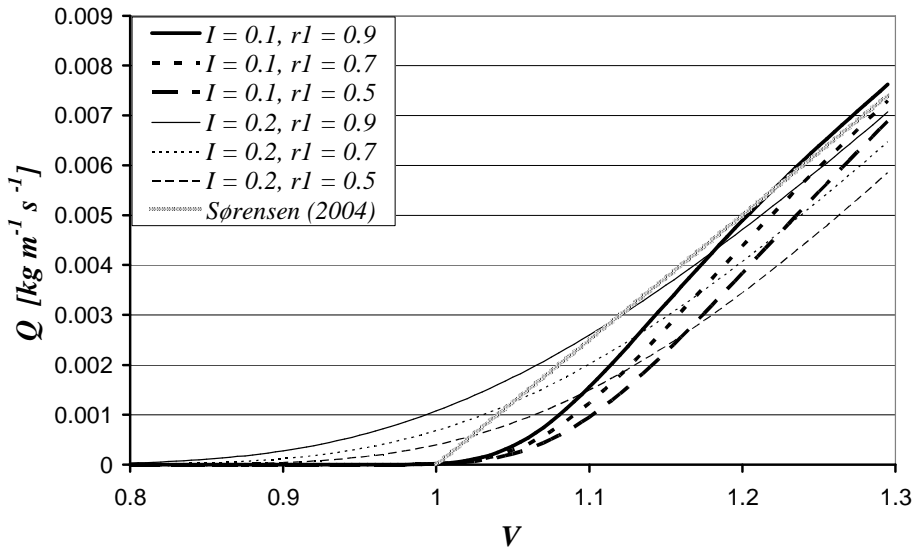


Fig. 1: Sand transport Q as function of the scaled saltation velocity V with the turbulence intensity I and the autocorrelation r_1 as parameters (Schönfeldt, 2008, 2011).

on the same scaled fluid threshold of $V_f = 1.25$. It is apparent that a meaningful threshold is never obtained by extrapolation of the transport to zero. Methods such as the time fraction equivalence method (TFE, Stout and Zobeck, 1996) or the fractionating in count rate method (Schönfeldt, 2004) provide only one threshold. Using synthetic time series of transport with the two Bagnold (1941) thresholds, these methods differ and do not find the thresholds introduced in the synthetic time series depending on the statistical parameters of the wind. The distribution functions of the powers of wind speed during saltation are indeterminate without knowledge of the thresholds. The key variables are the thresholds. They depend not only on the grain diameter, but also on the humidity of the bed and must be determined experimentally by testing transport equations with field observations.

In the following, two methods of threshold determination are discussed, both of which both provide a fluid and an impact threshold. We will show the need of high resolution sensors for determination of the two thresholds. Furthermore we provide thresholds of a natural mixed sand bed in dependence of the grain diameter.

Material and methods

1. The gust and lull method to determine the fluid and impact thresholds (GLM)

The gust and lull method (GLM) to determine the thresholds was introduced by Schönfeldt (2004) and is strictly based on the Bagnold's (1941) findings of the properties of the two thresholds. The basic idea is that in an intermittent transport there are periods with transport (gusts) and periods without transport (lulls). In the GLM, the time series of moving grains (data of Saltiphone, Sensit, Safire, etc.) were searched for periods with zeros following periods of saltation, and for periods of saltation following periods of zeros. Only periods with a minimum number of consecutive zeros followed by the same number of consecutive values greater than zero will be used from the data set for a gust interval, and vice versa for a lull interval. The fluid threshold is then calculated as the mean of wind speed on the sampling point preceding saltation and the wind speed on the sampling point on which saltation was first observed. The impact threshold is calculated as the mean of wind speed on the first sampling point without saltation and the wind speed on the preceding sampling point with saltation. In developing the method, Schönfeldt (2004) did not take into account that the time series of saltation lags behind the wind, but it is not a simple time shift of the two series. The time series of saltation is predicted by a transfer function of the wind time series. The transfer function can be established by exponential functions with a time constant (characteristic response time) τ without time shift (Pfeifer and Schönfeldt, 2012). Using these findings, GLM can be evaluated.

Figure 2 shows a sinusoidal, scaled wind-speed alteration with a relatively long period of 40 seconds. On the fluid threshold ($V = 1.25$), the saltation starts. Two models of transport reaction are plotted: an immediate reaction of saltation on wind speed (thick dotted line), and an exponential transfer function described by Eq. (7) with τ equal to 0.7 seconds (thick dashed line).

$$Q(t) = \int_0^{-\infty} H(V(t-\xi)) \exp(-(t-\xi)/\tau) \cdot V(t-\xi) d\xi \quad (7)$$

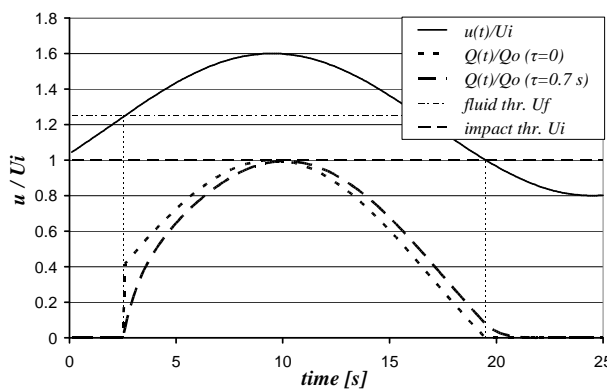


Fig. 2: A scaled, sinusoidal wind-speed alteration with a period of 40 seconds and the reaction to the saltation activity with two models: an immediate reaction of saltation on wind speed (thick dotted line), and an exponential transfer function with τ equal to 0.7 seconds (thick dashed line; this curve has the 'saw-tooth' shape also recovered in the measurements of Butterfield (1999)).

Eq. (7) is the convolution of wind speed with exponential transfer function of the wind to saltation activity in a linearized form. The sinusoidal gust produces a typically 'saw-tooth' shaped curve of transport also recovered in the measurements of Butterfield (1999). The transport has 8% of the steady state if the wind goes below the impact

threshold ($V = 1$). The GLM underestimates the impact threshold by up to 16%, depending on the resolution of the sensor used. A response time of 1.6s, as predicted by Butterfield, enlarges the error. On the other hand, the GLM provides exactly the fluid threshold and never the impact threshold if the response of saltation to wind speed fluctuations is a decay curve. Similar to Schönfeldt (2004), the GLM was tested using arbitrary time series of wind speeds. The time series of wind speed was modeled as a first-order autoregressive Markov process and the saltation activity, in contrast to Schönfeldt (2004), with Eq. (7) to produce an exponential transfer.

2. The iterative technique to determine the thresholds of transport (ITT)

Given the deficiency of the GLM, a method was developed to take a transfer function of wind to saltation activity into account. This method is described by Schönfeldt (2012). The method uses arbitrary transfer weights. The ITT provides thresholds from measured time series of wind and saltation activity. For this purpose, a discrete formulation of Eq. (7) is helpful:

$$Q_{approach}(j) = \sum_{i=0}^N h(j-i) f_{h(t=0)}(i) \cdot (u(j-i) - u_i) \quad (8)$$

Variables are defined as follows. Variable $u(j)$ is the measured wind speed at time j ; scaled wind speed was not used, the impact threshold u_i is unknown; $h(j)$ is the status of saltation and performs like the Heaviside function; $h(j)$ is equal to 1 if the wind speed is equal to or higher than the fluid threshold u_f ($u(j) \geq u_f$) and remains 1 if the wind speed stays above the impact threshold which involves $h(j-1) = 1$ (the previous time step was saltation and it will be sustained because $u(j)$ is greater than the impact threshold). In all other cases, $h(j)$ is equal to zero. Variables $f_i(i)$ are the transfer weights on the time shift $i\Delta t$ if $h(j=0) = 1$ (saltation begins or sustains), and $f_0(i)$ are the transfer weights on the time shift $i\Delta t$ if $h(j=0) = 0$ (saltation stops and dropout). $Q_{approach}(j)$ is a sand transport approach. The task of the ITT is to vary all these parameters on the right hand side of Eq. (8) such that

$$rmse = \sqrt{\frac{1}{M} \sum_{j=1}^M \left(\frac{Q(j)_{approach}}{\sigma_{Q_{approach}}} - \frac{Q(j)_{measured}}{\sigma_{Q_{measured}}} \right)^2} \quad (9)$$

will be a minimum. Essentially, two sets of transfer weights on $N+1$ nodes, and the two thresholds are to vary. If we use $N = 30$, we have 60 variables to vary, $f_i(0)$ can be set to 1 and $f_0(0)$ to zero ($h(j=0) = 0$ per definition). Alternatively, it is possible to use a sum of three exponential transfer characteristics, three to start saltation activity and three to cease saltation activity

$$f_{h(0),k}(i) = a_{h(t=0),k} \exp(-i\Delta t / \tau_{h(0),k}), \quad (10)$$

with $h(0) = 0, 1$ and $k = 1, 2, 3$. Then the $f_{h(t=0)}$ in Eq. (8) will be

$$f_{h(t=0)}(i) = \sum_{k=1}^3 f_{h(t=0),k}(i). \quad (11)$$

This process reduces the degrees of freedom from 61 to 11.

$rmse$ as calculated after Eq. (9) may have secondary minima. In this case, it is not easy to find the absolute maximum with a numerical program by varying the parameters. In the reviewed cases, start parameters could be varied and the minimum for $rmse$ was always the same, but with somewhat other weights $f_h(i)$. Insofar as the formulation of Eq. (10) is more particular, the numerical noise from one transfer weight to the other will be smoothed by the reduction to an exponentially transfer. In order to get the same minima with Eq. (10), not less than two to three characteristic response times are required.

3. Study site

Field experiments were carried out on the beach of Zingst in the North East part of the peninsula Fischland-Darß-Zingst on the Baltic Sea ($54^{\circ}26' N$, $12^{\circ}42' E$) during the spring of 2011. This beach is 18 km long, orientated along an East-West direction. Surface of the beach was covered with dry quartz sand with a mean grain diameter of $400 \mu m$. To remedy beach erosion in the past, gravellike material was hydraulically pumped onto the beach. Consequently, the size distribution of moving grains and of those on the surface was variable, depending on the wind direction. Slightly onshore winds activate finer sand from the foreshore/berm, and longshore winds activate the gravel-like particles from the backshore/beach. The prevailing wind direction is in the form of longshore westerlies. Measurements were carried out under such longshore winds, in order that fetch differences do not influence the measurements. In Figure 3, the instrument array is depicted. The Guelph sand trap was used to compare the measured webcam grain-size distribution with the sieved contents of the trap. An array of six microphones (black diaphragms in Fig. 3) works as array of six Saltiphones. The miniaturisation of the microphones (Saltiphones) leads to a less intense intervention in the flow and permit a fine sensing near the ground (the nearest two are 0.015 m above the ground level). A sonic anemometer was buried into the sand so that the centre of the sampling volume was at a typical height of 0.1-0.2 meters. This low measuring height was used to minimise the effect of time shift in the wind field as reported by van Boxel et al. (2004). This measuring position of the sonic is acceptable especially near the thresholds, i.e. in periods of low saltation intensity.

The webcam is a relatively new measuring device in measuring aeolian sand transport and is described by Schönfeldt (2012). The webcam observe the sand (beach surface) from a distance of 8 cm and has a resolution of 640×480 pixels. One pixel equates 0.1×0.1 mm on the beach surface. The webcam frame transfer is triggered by the sonic every 0.1 s. A laptop computer (shadow of the laptop, mounted on a tripod appears on the left in Fig. 3 behind the sonic) records data sequentially from the sonic, the webcam data generated parallel to the sonic, and microphone data, all in one file. Thereby, it will prevent a time shift in between the signals of the different instruments.

The guiding principle in webcam signal generation is that a previous frame will be compared to a current frame pixel by pixel. Where differences occur, a grain has moved. The software detects it and records the place of change. The postprocessing program arranges the pixels and provides grain sizes. The maximum usable frame rate is limited by the maximum usable data transfer. This frame rate is too low, and the exposure time of the webcam is too long for observation of saltating grains. The web-

cam cannot see moving grains, i.e., the moving grain appears as a shadow in the picture and is smaller than the noise. Creeping grains also move fast, but yet every saltating and creeping grain causes a change in light reflection on the start position and/or on the arrival point. Simply, the webcam signal is proportional to the number of grains that, on average, leaves and arrives in the webcam's visual field of the beach surface (6.4×4.8 cm). The webcam has potential in characterization of grain-size distribution (examination of sieved grain fractions in a wind tunnel), and the application of microphones is described in Schönenfeldt (2012).



Fig. 3: The instrument array. From left to right: Guelph sand trap, web cam, microphone array of six microphones (work as Saltiphones), and sonic anemometer (buried).

Results

Figure 4a shows the grain-size distribution of the contents of the Guelph sand trap after one hour exposure, together with the distribution measured by the webcam and the surrounding surface grain-size distribution. The curves in Figure 4a are normalized such that the sum of distribution bins multiplied by the bin distance ΔD is equal to 1. The different resolution of sieve set and webcam leads to different height of maxima. Nevertheless, the webcam overestimates the grains of size less 0.2 mm.

The Guelph sand trap has measured a sand transport of $0.001 \text{ kg m}^{-1} \text{ s}^{-1}$ and the webcam on average has determined 160 moving grains in one time step of 0.1 s, but only in 38% of the measuring time of one hour did the webcam record saltation activity. The maximum recorded activity was 2405 grains in one time step of 0.1 s. The mean friction velocity was 0.19 m/s, the turbulence intensity 0.41, and the autocorrelation of the wind $r_1 = 0.966$. On that day, the wind was extremely turbulent, and the measurement was suitable for the two above stated methods GLM and ITT.

In Figure 4b, grain-size distribution as measured the webcam is compared with sieved samples from the Guelph trap. Strong winds have activated gravel-like material which was hydraulically pumped onto the beach to remedy beach erosion. The shift of the maximum of the grain-size distribution is seen in the sieved probes as well as in the webcam signal. The particle-size distribution determined by sieving of the content of a Guelph sand trap after 10 minutes exposure is very similar to that determined with the web cam during the same time period. More results are given by Schönfeldt (2012).

As documented in Figures 4a and b, the webcam can clearly resolve grain size, and consequently the webcam was used to determine the thresholds. The thresholds (Fig. 5) are measured on the beach of Zingst using the webcam and the microphones, not measurements in a wind tunnel using different grain-size fractions. The bed is a mix of grains of different sizes (Fig. 4a). The software determines the diameter, sorts the grains and determines the thresholds using the GLM and ITT method.

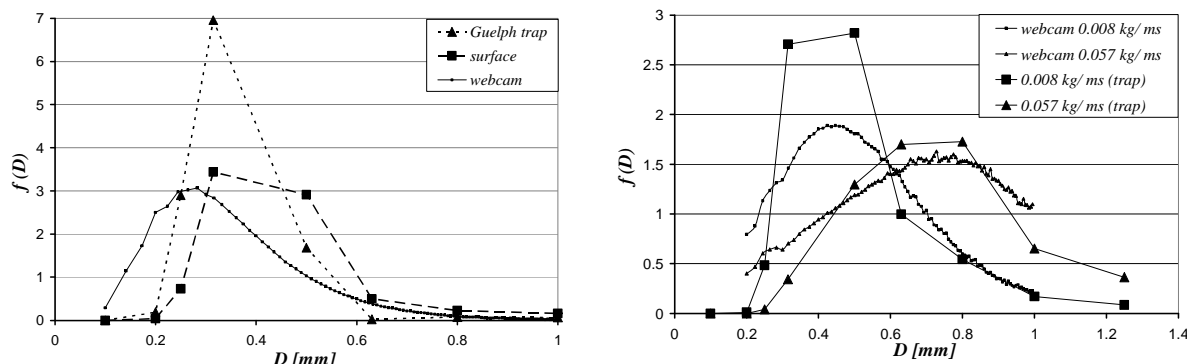


Fig. 4a: (left) *Grain-size distribution from 14.02.2011, dotted line - the contents of the Guelph sand trap, dashed line - the grain-size distribution of the uppermost 2 mm of the investigated area, and solid line - the grain-size distribution as measured the webcam.*

Fig. 4b (right) *The mean grain-size distribution for ten minutes on 24.03.2011, large symbols - the contents of the Guelph sand trap, small symbols - the grain-size distribution as measured with the webcam. The shift to the maximum grain size was caused by strong wind which activated the gravel-like material pumped onto the beach to remedy beach erosion.*

Given the errors of the GLM (see above), the two methods were tested with synthetic time series. A detailed variation of the parameters as Schönfeldt (2011) has used for the transport will be passed on. The parameters of the arbitrary time series of wind speed are adapted to the mean, the standard deviation and r_1 of measured wind parameters on 14.02.2011. Time series of wind speed were modeled as a first-order auto-regressive Markov process. Saltation activity was then modeled with Eq. (7) to produce an exponential transfer with a response time of one second ($\tau = 1$). The thresholds were selected such that the modeled transport activity was the same as in the measurements, which means transport occurred on 38% of the time. This is the same way of looking at the problem as Stout and Zobeck (1996), i.e., by determining the time fraction equivalence threshold of transport. In contrast to the latter, two scaled Bagnold thresholds ($V_i = 1$, $V_f = 1.25$) were used and received the scaled mean wind speed $\bar{V} = 0.8$, which caused 38% of saltation time activity in the synthetic transport time series.

The point of interest is not only the reaction of the methods on a response time, but also the reaction on noise in the signals. The wind speed on the webcam and the microphones is not the same as measured by the sonic, especially in the high frequency range. Successive noise is added to the synthetic time series, additive to the

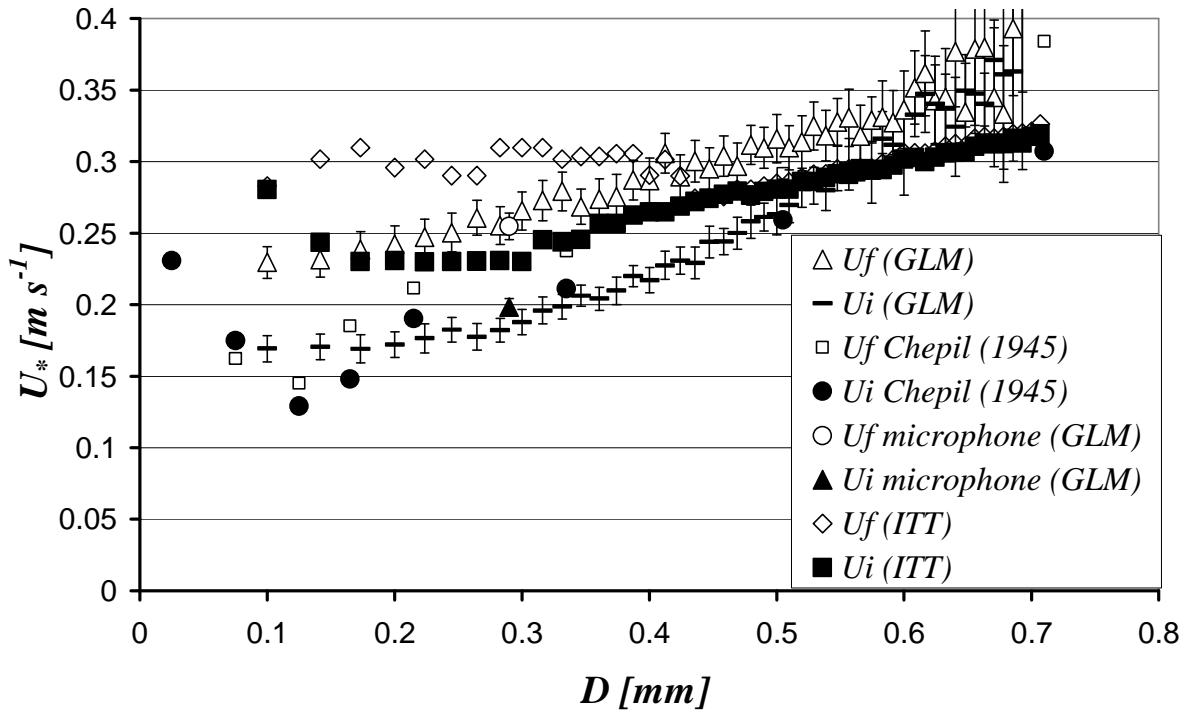


Fig. 5: Fluid and impact thresholds occurring on 14.02.2011 determined using the gust and lull method (GLM; Schönfeldt, 2004), with the iterative technique to determine the thresholds of transport (ITT) described in the text and data from Chepil (1945). Error bars on the GLM thresholds denote the 90% confidence interval.

wind and multiplicative to the transport. The rationale is that an additive noise to the transport in periods without saltation destroys the lull intervals and sometimes produces negative transport (the mean of the noise must be zero). The results are shown in Figure 6a. Note the axis of the abscissae is not absolutely correct, a result of the model used for noise. A random noise of 200% means that a Gaussian-distributed, non-correlated random noise with the same standard deviation as the model wind is added to the modelled wind speed and a non-correlated Gaussian random noise with the same standard deviation as the modelled saltation activity is multiplied with the saltation activity. The more or less variations from one point of calculation to the next are caused by the relatively “short” data length of 42345 observations, the same as existing data on 14.02.2011. Comparing the correlation coefficients of the noisy synthetic series (not shown in Fig. 6a) and the correlation coefficients of measured data (wind and approach saltation activity, $r \approx 0.9$), we can rate the noise in the measurements to 100 – 130%. The noisy synthetic time series of wind correlate with $Q_{approach}$ from one (no noise, $rmse = 0.0005$, Eq. (7)) to 0.37 (400% noise, $rmse = 3.5$). Without noise, the ITT method meets the thresholds exactly, the GLM underestimate the fluid threshold a bit and the impact threshold ($Vi (GLM) = 0.71!$) as given above. The departure from the value mentioned above is caused by the higher response time and the sensor used.

The program has no minimal threshold for saltation activity as a real sensor has. The program threshold is given by the number of transfer weights ($N = 30$); after three seconds, the transfer pipe (Eq. (8)) is broken off, and the saltation activity becomes zero in a lull interval.

The ITT method provides the transfer of wind to saltation activity as a by-product. In Figure 6b are transfer functions of wind to saltation activity shown. These are the transfer functions as a sum of the three exponential transfer characteristics (Eq. (11)), one if saltation and the second if the wind speed is lower than the impact threshold. The functions are standardised so that the integral over all of them is equal to 1. The two cases have three response times $\tau_{h,k}$, each with different corresponding amplitudes $a_{h,k}$ in Eq. (10).

Discussion

The above sentence “the GLM provides exactly the fluid threshold and never the impact threshold if the response of saltation to wind speed fluctuations is a decay curve” must be modified. A correction factor must include, depending on the relation of mean wind speed to the thresholds and on r_1 , the autocorrelation of the wind at lag one Δt . For the used statistical values and the thresholds, this factor is 1.016, less than 2 % of the value. If r_1 is lower as the used value of 0.966, the error becomes greater. The statistical error is caused by the calculation of the fluid threshold as the mean wind speed of the first sampling interval preceding saltation and the sampling interval in which saltation was first observed. These two values must be weighted by the probability of occurrence (see also Schönfeldt, 2004). With consideration of the statistical error, the GLM provides the fluid threshold.

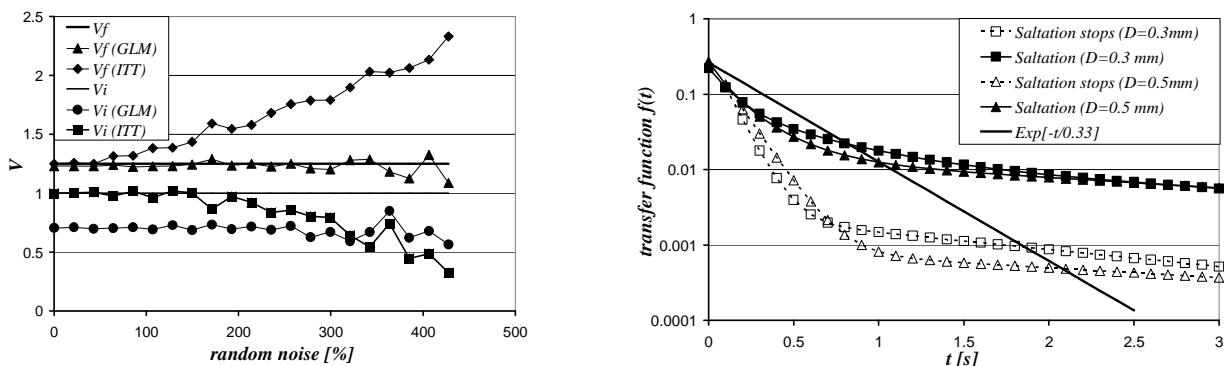


Fig. 6a: (left) Thresholds determined by the GLM and ITT method as a function of additional noise. V_i and V_f are the default normalised impact and fluid thresholds, respectively.

Fig. 6b: (right) Transfer functions of wind to saltation activity for two grain diameters. The transfer during the gust intervals with saltation is denoted by “Saltation” and in a lull interval where the wind speed is lower than the impact threshold by “Saltation stops”. For comparison, an exponential decay curve with $\tau = 0.33$ s is plotted.

The impact threshold determined by the GLM has also statistical errors and is additionally dependent upon the response time of saltation and the resolution of the used sensor. The GLM is not promising in determining the impact threshold. Conversely, the

ITT gives better impact thresholds as fluid thresholds when one considers additional noise. The ITT method seems to present reliable results for the impact threshold. In the region of the most recorded grains, the relation of $u_{*ITTimpact} / u_{*GLMfluid}$ is 0.89, the same as Chepil (1945) reported for this grain size. For a nearly uniform sand of average grain diameter 0.25 mm, Bagnold (1941, p. 57) obtained a fluid threshold friction velocity of 0.22 m s^{-1} and an impact threshold friction velocity of 0.192 m s^{-1} , which results in a ratio of impact threshold to fluid threshold equal to 0.87. The absolute friction velocities measured here seems a little bit too high, but it must be kept in mind that the presented thresholds are measured on a bed with a mix of grains of different sizes, not on a bed with homogeneous sand.

Thresholds for grains smaller than 0.2 mm should be treated with caution; the webcam detects more grains than actually occur. These grains can be a mix of fine grains and “splintered” pixels from large grains. Grains greater than 0.6 mm are rather rare (see Fig. 4a). The confidence interval of the GLM shows that, too. Apart from this, the measured thresholds behave as the thresholds determined from the synthetic time series. On the other hand, it is not clear how the small grains influence the fluid threshold of large grains. If small grains are saltating, they can strike a larger grain and then the larger grain has sufficient energy to leave the bed. Given this issue, the measured thresholds are plausible.

The response of saltation activity on wind speed corresponds with the response time as determined by Pfeifer and Schönfeldt (2012) in cases of continuously saltating grains. In the case when saltation drops out, there are two equal response times. This means that two constants are sufficient to describe the drop-out process, but not so for beginning and maintenance of saltation. When the saltation begins and is sustained, there are three time constants necessary to describe saltation. In both cases, an exponential decay curve with $\tau = 0.33\text{s}$ drop out slow up more as the measured in the time scale of zero to two seconds, and then the measured transfer functions drop out slow up. The persistent stronger slow up of the transfer function in a lull interval is expected.

Conclusions

Measurements show that the webcam is effective in measuring saltation with high spatial and temporal resolutions. The webcam provides useful results to determine the grain size distribution up to a tenth of a second. A gap yet persists in determining thresholds between the two methods, GLM and ITT. It is more a shortcoming of the methods than one of the webcam. The weak point of the ITT method is the high-frequency noise caused by the fact that wind and transport are not measured at the same place. The root-mean-square error between measured and calculated transport data has then a very flat absolute minimum.

Of the two methods for determining thresholds of saltation, acceptable errors were obtained for fluid threshold with the GLM and for impact threshold with the ITT. To reduce noise in the time series, distance between webcam and sonic could be reduced. A hot-wire anemometer in lieu of a sonic may be the way to entirely solve this problem. All in all, there is a wide application spectrum for a future use of the webcam or a similar camera system.

Acknowledgement

The article was improved thanks to comments from W. C. Johnson and Ch. Jacobi.

References

- Bagnold, R.A., 1941: The Physics of Blown Sand and Desert Dunes. Methuen, London, 256 pp.
- Bowker, G.E., Gillette, D.A., Bergametti, G., Marticorena, B., Heist, D.K., 2007: Sand flux simulations at a small scale over a heterogeneous mesquite area of the northern Chihuahuan Desert. *Journal of Applied Meteorology and Climatology* 46(9), 1410–1422.
- Butterfield G.R., 1999: Application of thermal anemometry and high-frequency measurement of mass flux to aeolian sediment transport research. *Geomorphology* 29: 31–58.
- Chepil, W.S., 1945: Dynamics of wind erosion. II. Initiation of soil movement. *Soil Science* 60(4): 397-411.
- Gillette, D.A., Goodwin, P.A., 1974: Microscale transport of sand-sized soil aggregates eroded by wind. *J. Geophys. Res.*, 79, 4080–4084.
- Gillette, D.A., 1979: Environmental factors affecting dust emission by wind erosion. *Saharan Dust, SCOPE 14*, C. Morales, Ed., John Wiley and Sons, 71–91.
- Gillette, D.A., Stockton, H., 1989: The effect of nonerodible particles on wind erosion of erodible surfaces. *J. Geophys. Res.*, 94, 12 885–12 893.
- Iversen, J.D., Rasmussen, K. R., 1999: The effect of wind speed and bed slope on sand transport. *Sedimentology* 46, 723 – 731.
- Kawamura, R., 1964: Study of sand movement by wind. Translated (1965) as University of California Hydraulics Engineering Laboratory Report HEL 2-8 Berkeley.
- Jacksen, D.W.T., 1997: A new, instantaneous Aeolian sand trap design for field use. *Sedimentology* 43, 791-796.
- Leenders, J.K., van Boxel, J.H., Sterk, G., 2005: Wind forces and related saltation transport. *Geomorphology*, 71, 357–372.
- Lettau, K., Lettau, H., 1978: Experimental and micrometeorological field studies of dune migration. Exploring the World's Driest Climate, K. Lettau and H. Lettau, Eds., University of Wisconsin—Madison IES Rep. 101, 110–147.
- Leys, J.F., Raupach, M. R., 1991: Soil flux measurements using a portable wind erosion tunnel. *Aust. J. Soil Res.*, 29, 533–552.
- Owen, R.P., 1964: Saltation of uniform grains in air. *J. Fluid. Mech.*, 20, 225-242.
- Pfeifer, S., Schönfeldt, H.-J., 2012: The response of saltation to wind speed fluctuations. *Earth Surface Processes and Landforms*, DOI: 10.1002/esp.3227.
- Schönfeldt, H.-J., 2003: Remarks on the definition and estimation of the aeolian erosion threshold friction velocity. *Meteorol. Z.*, 12, 137-142.
- Schönfeldt, H.-J., 2004: Establishing the threshold for intermittent aeolian sediment transport. *Meteorol. Z.*, 13, 3, 437-444.
- Schönfeldt H-J. 2008: Turbulence and aeolian sand transport. (16.04.2008, EGU Vienna)
http://www.uni-leipzig.de/~meteo/en/orga/Schoenfeldt_EGU_2008_presentation.pdf
- Schönfeldt, H.-J., 2011: Turbulence and aeolian sand transport. *Wissenschaft. Mitt. aus dem Inst. f. Meteorologie d. Uni. Leipzig* 48, 103-112.

http://www.uni-leipzig.de/~meteo/de/orga/LIM_Bd_48.pdf

- Schönenfeldt, H.-J., 2012: High resolution sensors in space and time for determination saltation and creep intensity. *Earth Surface Processes and Landforms*, DOI: 10.1002/esp.3228.
- Shao, Y., Raupach, M. R., Findlater, P. A., 1993: Effect of saltation bombardment on the entrainment of dust by wind. *J. Geophys. Res.*, 98, 12, 719–12 726.
- Sørensen, M., 1985: Estimation of some Aeolian saltation transport parameters from transport rate profiles. *Proc. Int. Workshop on the Physics of Blown Sand*, Vol. 1, Aarhus, Denmark, University of Aarhus, 141–190.
- Sørensen, M., 1997: On the effect of time variability of the wind on rates of Aeolian sand transport. *Aarhus Geoscience*, 7, 73-77, (Department of Earth Sciences, University of Aarhus).
- Sørensen, M., 2004: On the rate of aeolian sand transport. *Geomorphology*, 59, 53-62.
- Spaan W.P, Van den Abeele G.D. 1991. Wind borne particle measurements with acoustic sensors. *Soil Technology* 4: 51-63.
- Stout, J.E., Zobeck, T.M., 1996. Establishing the threshold condition for soil movement in wind-eroding fields. *Proceedings of International Conference on Air Pollution from Agricultural Operations*, February 1996, Kansas City, Missouri, USA, Midwest Plan Service (MWPS C-3). Iowa State University, Ames, Iowa, USA, pp. 65–71.
- Stout, J.E., Zobeck, T. M., 1997: Intermittent saltation. *Sedimentology*, 44, 959–970.
- Stout, J.E., 1998: Effect of averaging time on the apparent threshold for aeolian transport. *Journal of Arid Environments*, 39, 395-401.
- Stout, J. E., 2004: A method for establishing the critical threshold for aeolian transport in the field. *Earth Surface Processes Landforms*, 29, 1195–1207.
- Van Boxel JH, Sterk G, Arens SM. 2004: Sonic anemometers in aeolian sediment transport research. *Geomorphology* 59: 131–147.
- White, B., 1979: Soil transport by winds on Mars. - *J. Geophys. Res.*, 84, 4643-4651
- Williams, G., 1964: Some aspects of the eolian saltation load. *Sedimentology*, 3, 257–287.
- Zheng, X. J., Huang, N., Zhou, Y.-H., 2003: Laboratory measurement of electrification of wind-blown sands and simulation of its effect on sand saltation movement. *J. Geophys. Res.*, 108, 4322, doi:10.1029/2002JD002572.
- Zheng, X. J., Huang , N., Zhou, Y., 2006: The effect of electrostatic force on the evolution of sand saltation cloud. *Eur. Phys. J. E*, 19, 129–138.
- Zingg, A. W., 1953: Wind tunnel studies of the movement of sedimentary material. *Proc. Fifth Hydraulics Conf.*, Bulletin 34, Iowa City, IA, Institute of Hydraulics, 111–135.

Address of the Author

Hans-Jürgen Schönenfeldt

University of Leipzig, Institute for Meteorology, Stephanstr. 3, D04103 Leipzig

e-mail: schoenfeldt@uni-leipzig.de

Jahresbericht des Institutes für Meteorologie der Universität Leipzig 2011

1. Bearbeitete Forschungsprojekte

AG Atmosphärische Strahlung

Hubschraubergetragene Strahlungsmessungen zur Bestimmung des Einflusses von Wolkeninhomogenitäten tropischer Grenzschichtbewölkung auf die Strahlungsbilanz

Helicopter-borne radiation measurements to investigate the influence of cloud heterogeneities of tropical boundary layer clouds on radiative budget

F. Henrich (f.henrich@uni-leipzig.de), M. Wendisch (m.wendisch@uni-leipzig.de)
H. Siebert (siebert@tropos.de)

Die Vernachlässigung von horizontalen Wolkeninhomogenitäten in Modellen zur Berechnung der solaren Strahlungsbilanz von Wolken kann zu erheblichen Diskrepanzen zwischen Modellergebnissen und Messungen führen. In Zusammenarbeit mit dem Leibniz-Institut für Troposphärenforschung wird der Einfluss von Inhomogenitätseffekten von tiefer Cumulusbewölkung in den Tropen auf den Strahlungshaushalt untersucht. Hierfür wird ein neues, kompaktes Messsystem für spektrale Strahlungsmessungen gebaut, welches zusammen mit einer Messplattform für Aerosol-, Turbulenz- und Mikrophysikalischen Wolkenparametern (ACTOS) erstmals die gleichzeitige Beobachtung von Wolkenmikrophysikalischen und Strahlungsgrößen ermöglichen wird. Hierfür wird ein Hubschrauber als Instrumententräger genutzt. Ergänzend sollen dreidimensionale Rechnungen mit einem Strahlungstransfermodell zur Interpretation der Messungen durchgeführt werden.

Das Messgebiet (Barbados) bietet aufgrund seiner Lage zusätzlich die Möglichkeit der Untersuchung von anthropogenen Einflüssen auf den atmosphärischen Strahlungstransfer und die Beeinflussung des solaren Strahlungshaushaltes durch Feuchtigkeits-Halos.

Weiterführung: ja

Finanzierung: Uni Leipzig, DFG WE 1900/18-1, IfT Leipzig

AG Atmosphärische Strahlung

Räumliche Verteilung von Eis- und Flüssigwasser in Arktischen Mischphasenwolken und deren Einfluss auf Energiehaushalt und Fernerkundung

Spatial distribution of ice and liquid water in Arctic mixed-phase clouds and its impact on energy budget and remote sensing

A. Ehrlich (a.ehrlich@uni-leipzig.de), E. Bierwirth (eike.bierwirth@uni-leipzig.de)
M. Wendisch (m.wendisch@uni-leipzig.de)

Mischphasenwolken mit nebeneinander existierendem flüssigem Wasser- und Eisanteil treten häufig in arktischen Regionen auf. Sie können theoretisch in einem Temperaturbereich zwischen -40 °C und 0 °C über längere Zeit hinweg stabil

existieren. Wie bekannt ist, unterscheiden sich die optischen Eigenschaften von reinen Wasser- und Eiswolken und damit auch ihr Einfluss auf die solare Strahlung. Zur Untersuchung der horizontalen Verteilung von Eis- und Flüssigwasser und deren Einfluss auf den Strahlungstransport wird dieses Projekt in Zusammenarbeit mit dem Alfred-Wegener-Institut für Polar- und Meeresforschung (AWI), Bremerhaven, durchgeführt.

Kern des Projektes ist die internationale Messkampagne „Solar Radiation and Phase Discrimination of Arctic Clouds“ (SORPIC), die vom 30.April bis zum 20.Mai 2010 auf Svalbard (Norwegen) stattfand (Projekt-Webseite <http://www.uni-leipzig.de/~sorpic/>). Dabei wurden erfolgreich spektrale solare Strahlungsmessungen an Bord des Forschungsflugzeuges Polar-5 des AWI durchgeführt. Die gemessenen Strahlungsdaten sind vollständig korrigiert und kalibriert und stehen den Projektpartnern zur Verfügung.

Simultan wurden Messungen mit der hyperspektralen Kamera AISA Eagle des AWI durchgeführt; die Auswertung erfolgt in Zusammenhang mit den Strahlungsdaten des SMART-Albedometers am LIM. AISA Eagle wurde im Labor des LIM spektral und radiometrisch kalibriert.

Am 15.November 2010 hat das LIM einen Daten-Workshop mit den beteiligten Projektpartnern (AWI Potsdam/Bremerhaven, LaMP Clermont-Ferrand (Frankreich), Freie Universität Berlin) veranstaltet, bei dem der Fortgang der Datenauswertung und das Publikationskonzept für 2011 abgesprochen wurden.

Weiterführung: ja

Finanzierung: DFG WE 1900/17-1

AG Atmosphärische Strahlung

Einfluss von SAHARA-Staubschichten und Biomasseverbrennungsprodukte auf den atmosphärischen Strahlungsantrieb

Influence of Saharan dust layers and biomass burning on atmospheric radiative forcing

S. Bauer (mail@bauerstefan.com), [M. Wendisch \(m.wendisch@uni-leipzig.de\)](mailto:m.wendisch@uni-leipzig.de)

B. Heinold (heinold@mail.tropos.de), I. Tegen (itegen@tropos.de)

A. Torge (atorge@ifm-geomar.de), A. Macke (macke@tropos.de)

Das Projekt untersucht den Einfluss von Saharastaub und Biomasseverbrennungsprodukte auf den atmosphärischen Strahlungshaushalt. Dafür stehen flugzeuggetragene und bodengebundene Messungen von solaren Radianzen und Irradianzen während der Kampagne SAMUM 2 (Saharan Mineral Dust Experiment) auf den Kap Verden im Januar/Februar 2008 zur Verfügung. Somit wurden Strahlungsmessungen unter und über Staub- und Biomasseschichten durchgeführt. Die gesammelten Daten werden unter Zuhilfenahme von eindimensionalen Strahlungstransfersimulationen auf Abkühlungs- und Erwärmungseffekte solarer Strahlung in Staub- und Biomasseschichten untersucht. Die gemessenen aufwärtsgerichteten Radianzen über Staubschichten werden zudem mit Messungen des Meteosat-Second-Generation-Satelliten (MSG) verglichen. Unter Annahme von isotroper atmosphärischer Strahlung können

Irradianzen aus MSG-Radianzen abgeleitet und mit den gemessenen Irradianzen auf dem Flugzeug verglichen werden.

Weiterhin werden Ergebnisse aus Staubtransportmodelle, die im Zuge von SAMUM 1 im Jahr 2006 entwickelt wurde, mit den gemessenen Irradianzen verifiziert.

Weiterführung: nein

Finanzierung: DFG WE 1900/15-1

AG Atmosphärische Strahlung

Eine neue Methode zur bodengebundenen Fernerkundung von Profilen mikrophysikalischer Eigenschaften von Wolken mittels abtastender Radiometrie und Lidar

A novel method for ground-based remote sensing of profiles of cloud microphysical properties using scanning radiometry supplemented by Lidar

E. Jäkel (e.jaekel@uni-leipzig.de), J. Walter (jwalter@uni-leipzig.de), M.Wendisch (m.wendisch@uni-leipzig.de)

Mit Hilfe einer neuen bodengebundenen aktiven und passiven Fernerkundungsmethode soll die vertikale Entwicklung der Wolkenmikrostruktur und das Tropfenwachstum in konvektiven Wolken untersucht werden. Für diesen Zweck werden Strahldichtemessungen (passiv) der an den Wolkenrändern reflektierten solaren Strahlung mit Lidarmessungen (aktiv) kombiniert. Die Wolkenseite wird mit beiden Geräten sowohl zeitlich als auch örtlich synchronisiert vermessen. Diese Messungen werden mit neuen Algorithmen zur Gewinnung von wolkenmikrophysikalischen Parametern kombiniert. Aus den analysierten Messungen kann dann ein Vertikalprofil der thermodynamischen Phase, sowie der effektive Wolkenpartikelradius abgeleitet werden. Dabei werden die drei-dimensionalen Strahlungseffekte der räumlich und zeitlich inhomogenen konvektiven Wolke berücksichtigt, was bei dieser Beobachtungsgeometrie unabdingbar ist.

Weiterführung: ja

Finanzierung: DFG JA 2023/2-1

AG Atmosphärische Strahlung

Megacities - Hochauflöste spektrale Albedo-Karten von Megastädten und ihre Anwendung in Aerosol-Satelliten Datengewinnung

Megacities - High-resolution spectral albedo maps of megacities and its application in aerosol retrievals from satellite data

B. Mey (b.mey@uni-leipzig.de), M. Wendisch (m.wendisch@uni-leipzig.de)
H. Jahn (heiko.jahn@uni-bielefeld.de), A. Krämer (alexander.kraemer@uni-bielefeld.de),

Chen Xingfeng (chenxf@irsa.ac.cn), Gu Xingfa (guxingfa@irsa.ac.cn)

Megastädte sind eines der größten Quellgebiete anthropogenen Aerosols. Sie fungieren daher als Punktquellen für Aerosole im globalen Kontext und beeinflussen lokal die Gesundheit der Menschen. Daher ist es wichtig den Aerosolgehalt der Atmosphäre in Megastadt-Regionen möglichst genau zu bestimmen. In Regionen ohne dichtes Messnetz für Spurenstoffe, ist die Satelliten-Fernerkundung ein geeignetes Mittel, um Spurenstoffe regelmäßig zu messen. Zur Ableitung der Aerosoloptischen Dicke aus Satellitendaten muss das empfangene Signal der reflektierten Strahlung in einen atmosphärischen Anteil und den Bodenanteil getrennt werden. Der Bodenanteil ist durch die Boden-Albedo oder –Reflektivität gegeben, welcher schwierig aus Satellitenmessungen bestimmt werden kann.

Spektral und räumlich hochauflöste Messungen der Bodenalbedo wurden mit der Kombination aus den flugzeuggetragenen Messsystemen SMART-Albedometer (400-2100 nm) und einer Kamera (Geospatial Systems, MS 4100) mit 3 spektralen Kanälen gemessen. Der erste Datensatz wurde in Leipzig im Jahr 2007 aufgenommen, der zweite Datensatz konnte im Dezember 2009 in Zhongshan, China, gemeinsam mit unseren chinesischen Kooperationspartnern des Institute of Remote Sensing Applications erfasst werden.

Das Satelliten-Tool IMAPP der Universität Wisconsin wurde auf Computern des Instituts für Meteorologie installiert und steht nun für wissenschaftliche Zwecke in diesem, sowie anderen Projekten bereit.

Es wird erwartet, dass durch Verwendung der hochauflösten Messdaten der Bodenalbedo im Aerosol-Retrieval der Satellitendaten das Resultat der Aerosol Optischen Dicke verbessert werden kann.

Weiterführung: ja

Finanzierung: DFG, SPP 1233 (WE 1900/16-2)

AG Atmosphärische Strahlung

Räumlich inhomogene Zirren: Einfluss auf die atmosphärische Strahlung

Spatially Inhomogeneous Cirrus: Influence on Atmospheric Radiation

M. Wendisch (m.wendisch@uni-leipzig.de)

Die Strahlungseffekte durch inhomogene Zirren werden mit Hilfe einer Kombination von Flugzeuggetragenen Messungen (Strahlung und mikrophysikalische Eigenschaften), einem 3D Strahlungsmodell und einem dynamischen wolkenauflösenden Zirrus-Modell untersucht. Ein instrumentiertes Flugzeug (Lear-Jet) misst die spektrale Strahlung über Zirren im Rahmen einer Feldmesskampagne. Daraus werden die mikrophysikalischen Felder der Zirren abgeleitet. Diese werden verglichen mit gleichzeitigen in situ Messungen, welche mit einer Schleppsonde gesammelt werden. Diese wird gleichzeitig vom Flugzeug durch die Zirren gezogen wird. Parallel dazu werden die örtlichen Inhomogenitäten der Zirren Felder mit Hilfe einer abbildenden digitalen CCD Kamera beobachtet. Zusätzlich wird ein wolkenauflösendes Zirren-Modell benutzt zur Berechnung der mikrophysikalischen Zirren-Felder. Die aus den kombinierten in situ und indirekten Messungen abgeleiteten sowie modellierten mikrophysikalischen Zirren-Felder werden als

Eingabe für ein 3D Strahlungsmodell benutzt, um die 3D-Effekte inhomogener Zirren zu untersuchen.

Weiterführung: ja

Finanzierung: DFG WE 1900/19-1

.....

AG Atmosphärische Strahlung

Solare Strahlungsmessungen auf HALO

Solar Radiation Measurements on HALO

C. Fricke (fricke@uni-leipzig.de)

M. Wendisch (m.wendisch@uni-leipzig.de)

HALO (High Altitude and LOng Range Research Aircraft) ist das Synonym für das neue deutsche Forschungsflugzeug mit dem es möglich sein wird, eine Vielzahl von verschiedenen atmosphärischen Parametern bis hin in die untere Stratosphäre zu messen. Aufgrund seiner Reichweite, sowohl in vertikaler als auch in horizontaler Richtung bietet HALO die Möglichkeit großräumige Strahlungsfelder zu erfassen. Während zwei HALO Demo-Missionen kommen dabei neu entwickelte Spektrometersysteme zur spektralen Erfassung solarer Strahlung zum Einsatz. Die dabei ermittelten Messgrößen sind zum einen die (i) spektrale Strahlflussdichte, welche den solaren Strahlungshaushalt der Atmosphäre bestimmt, sowie die (ii) spektrale aktinische Flussdichte, welche photolytische Prozesse innerhalb der Atmosphäre kontrolliert. Die solare spektrale Strahldichte in Nadir-Richtung wird für Fernerkundungsuntersuchungen zusätzlich simultan gemessen. Für die Strahlflussdichten ist es dabei entscheidend, die aufwärts- sowie abwärts gerichteten Flussdichten, welche mittels der Kosinusempfänger oberhalb und unterhalb des Flugzeugs empfangen werden, zu unterscheiden. Hierfür sind Stabilisierungsplattformen vorgesehen, die die Bewegungen des Flugzeuges aufzeichnen und die Position der Empfänger mit hinreichender zeitlicher Verzögerung korrigieren. Bezuglich der aktinischen Flussdichte ist die Kombination aus hoher zeitlicher Auflösung und hoher Genauigkeit innerhalb des UV-B Bereiches die größte Herausforderung. Realisiert wird selbige durch eine entsprechende Kombination aus Monochromatoren und Detektoren. Die aus allen Daten gewonnenen Erkenntnisse sollen zur Modellverbesserung verwendet werden, um sowohl Oxidationsprozesse als auch die mikrophysikalischen Prozesse, welche für die Bildung und zeitlichen Entwicklung von Zirren verantwortlich sind, besser zu verstehen.

Weiterführung: ja

Finanzierung: DFG WE 1900/21-1

.....

AG Atmosphärische Strahlung

HALO Koordination von “Aerosol, Cloud, Precipitation, and Radiation Interactions and Dynamics of Extra-Tropical Convective Cloud Systems” (ACRIDICON)

HALO coordination of ACRIDICON

D. Rosenow (d.rosenow@uni-leipzig.de)

M. Wendisch (m.wendisch@uni-leipzig.de)

Konvektive Wolken können erheblichen ökonomischen Schaden verursachen aufgrund von starken Windböen, heftigen Schauern und Niederschlägen, welche teilweise mit Hagel, Graupel, und Gewittern verbunden sein können. Die Dynamik und Heftigkeit dieser ausgeprägten Wettererscheinungen werden bestimmt durch mikrophysikalische Prozesse bei der Wolken- und Niederschlagsbildung, welche beeinflusst werden können durch Aerosolpartikel und Wechselwirkungen mit atmosphärischer Strahlung. Weiterhin werden durch konvektive Wolken Spurengase und Aerosolpartikel prozessiert und umverteilt durch vertikalen Transport sowie Ein- und Ausmischen der Wolke mit der Umgebungsluft. Um diese Wechselwirkungen zwischen Spurengasen, Aerosolpartikeln und der Wolken- und Niederschlagsbildung sowie atmosphärischer Strahlung in außertropischen, konvektiven Wolken zu untersuchen, wurde die HALO Demo-Mission “Aerosol, Wolken, Niederschlag, und Strahlungswechselwirkungen sowie Dynamik von außertropischen, konvektiven Wolkensystemen (ACRIDICON)” vorgeschlagen. ACRIDICON trägt bei zu zwei Schwerpunkten des SPP 1294 bei: „Wolken und Niederschlag“ und „Transport und Dynamik in der Troposphäre und der unteren Stratosphäre“. Der vorliegende Antrag beinhaltet hauptsächlich die Organisation und das Management von ACRIDICON sowie teilweise einen Beitrag zur Analyse und Auswertung der Strahlungsmessungen, welche bei dieser HALO Demo-Mission gesammelt werden.

Weiterführung: ja

Finanzierung: DFG WE 1900/22-1

AG Atmosphärische Strahlung

Koordination des Schwerpunktsprogramms 1294 "Atmosphären- und Erdsystemforschung mit dem Forschungsflugzeug HALO (High Altitude and Long Range Research Aircraft)"

HALO coordination project

M. Wendisch (m.wendisch@uni-leipzig.de)

D. Rosenow (d.rosenow@uni-leipzig.de)

Das Projekt dient vornehmlich der Kooperation und der Kommunikation unter den Einzelprojekten des Schwerpunktprogramms. Im Rahmen des Projekts werden ein jährliches Statusseminar sowie jährliche Themen-Workshops geplant und durchgeführt. Die drei Koordinatoren vertreten den SPP gegenüber der DFG, dem Wissenschaftlichen Lenkungsausschuss von HALO (WLA), dem HALO Projektteam des Deutschen Zentrums für Luft- und Raumfahrt (DLR) und nach außen. Das Koordinatoren-Team betreibt Maßnahmen zur Nachwuchs- und Gleichstellungsförderung. Zentrale Initiativen wie gemeinsame Sammelveröffentlichungen in einem Sonderband oder die Durchführung von Sitzungen zu Themenschwerpunkten ("special sessions") bei internationalen

Konferenzen sowie der Internetauftritt des SPP werden im Rahmen dieses Projekts koordiniert und durchgeführt.

Weiterführung: ja

Finanzierung: DFG WE 1900/24-1

AG Atmosphärische Strahlung

EUFAR - European Facility for Airborne Research in Environmental and Geosciences

M. Wendisch (m.wendisch@uni-leipzig.de)
D. Rosenow (d.rosenow@uni-leipzig.de)

Im Rahmen dieses Projektes werden die Expert Working Groups koordiniert. Workshops werden organisiert, und ein Buch wird geschrieben:
Wendisch, M., and J.-L. Brenguier, Airborne Measurements – Methods and Instruments. In preparation to be published by *Wiley & Sons*.

Weiterführung: ja

Finanzierung: EU

AG Atmosphärische Strahlung

Spektrale Strahlungsbilanz über dem Atlantik aus Modell und Beobachtung

Spectral radiation budget over the Atlantic Ocean from model and observation

A. Macke (macke@tropos.de)
M. Wendisch (m.wendisch@uni-leipzig.de)
M. Brückner (mbrueck@rz.uni-leipzig.de)
B. Pospichal (bernhard.pospichal@uni-leipzig.de)

Der Stoff- und Energieaustausch zwischen Ozean und Atmosphäre spielt eine entscheidende Rolle für die physikalische, chemische und biologische Entwicklung unseres Klimasystems Erde. Die von den beteiligten Forschungseinrichtungen entwickelten und eingesetzten Technologien zur in-situ Messung im Ozean und zur aktiven/passiven Fernerkundung der Atmosphäre, ermöglichen erstmalig durch eine Kombination dieser Daten eine kontinuierliche Erfassung relevanter Parameter. Im Rahmen des WGL-Verbundprojekts OCEANET wurde in Zusammenarbeit der Forschungseinrichtungen (IFM-GEOMAR, IfT Leipzig, Universität Leipzig, GKSS Geesthacht, AWI) eine autonome Messplattform entwickelt, die langfristig für den operationellen Betrieb an Bord von Fracht- und Forschungsschiffen vorgesehen ist.

Zum Verstehen des Klimasystems Ozean und Atmosphäre spielen Wolken und Strahlung eine wichtige Rolle. Da die Wolkenstrukturen sehr inhomogen sind und damit für Strahlungsübertragungsprozesse entscheidend sind, müssen diese Prozesse in Strahlungsparametrisierungen berücksichtigt werden. Eine Kombination der Beobachtung von physikalischen Eigenschaften und Strahlungseigenschaften von Wolken sind eine Möglichkeit solche

Parametrisierungen anzugelichen oder zu validieren. Mithilfe der Erweiterung der breitbandigen Strahlungsflussdichtemessungen auf spektrale Strahldichte- und Strahlungsflussdichtemessungen mit einem bodengebundenem Spektrometer (CORAS) können unterschiedliche Wolkentypen zugeordnet werden. Beobachtete Atmosphärenzustände werden in ein 3D-Monte-Carlo Strahlungstransportmodell eingegeben, sodass die Ergebnisse mit den gemessenen Parametern verglichen werden können. Die Messungen finden weitestgehend auf FS Polarstern statt.

Weiterführung: ja

Finanzierung: Leibniz-Institut für Troposphärenforschung

AG Wolken und globales Klima

Evaluierung des Einflusses von kurzlebigen Verschmutzungen der Atmosphäre auf Klima und Luftqualität

Evaluating the climate and air quality impacts of short-lived pollutants (ECLIPSE)

Koordinator: A. Stohl, Norwegian Institute for Air Research (ast@nilu.no)

Beitrag der Universität Leipzig: J. Quaas (johannes.quaas@uni-leipzig.de)

ECLIPSE hat zum Ziel, effektive Emissions-Reduktions-Strategien für kurzlebige, klimarelevante Verschmutzungsstoffe in der Atmosphäre zu entwickeln und zu evaluieren. Gase und Aerosole wie Stickoxide, Kohlenwasserstoffe, Sulfat und Ruß werden derzeit nicht in klimapolitische Maßnahmen einbezogen. Eine Reduktion kann aber der Abmilderung des Klimawandels dienen und gleichzeitig die Luftqualität verbessern. In ECLIPSE trägt die Universität Leipzig gekoppelte Klimasimulationen mit dem Modellsystem ECHAM6-HAM/MPIOM bei und analysiert Beobachtungen der Klimaänderungen in Osteuropa nach der Wende.

Weiterführung: ja

Finanzierung: EU FP7

Monitoring von Zusammensetzung der Atmosphäre und Klima – Interims-Implementierung.

Monitoring atmospheric composition and climate – interim implementation (MACC-II)

Koordinator: V.-H. Peuch, Europäisches Zentrum für Mittelfristige Wettervorhersage (Vincent-Henri.Peuch@ecmwf.int)

Beitrag der Universität Leipzig: J. Quaas (johannes.quaas@uni-leipzig.de)

Im Rahmen des europäischen Beitrags für das globale Monitoring für Umwelt und Sicherheit (Global Monitoring for Environment and Security, GMES), bildet MACC den Vorläufer des operationellen Dienstes für die Atmosphärenkomponente. Dabei wird durch die Assimilation einer Vielzahl von Beobachtungen der Zusammensetzung der Atmosphäre in einer neuen Version des Wettervorhersagemodells des Europäischen

Zentrums für mittelfristige Wettervorhersage (EZMW) ein konsistenter Datensatz geschaffen. Beitrag der Universität Leipzig ist es, den Klimaantrieb durch den anthropogenen Beitrag zur Aerosolbelastung aufgrund ihres Einflusses auf die Wolken zu berechnen. Auf Basis des neuen Datensatzes soll ein verbesserter Ansatz entwickelt werden.

Weiterführung: ja

Finanzierung: EU FP7

AG Allgemeine Meteorologie

Entwicklung eines tomographischen Wasserdampfsondierungssystems auf der Basis von GNSS Daten.

Development of a tomographic water vapour sounding system based on GNSS data

Prof. Dr. G. Tetzlaff (tetzlaff@uni-leipzig.de), Dr. A. Raabe (raabe@uni-leipzig.de),
Dr. M. Bender, Prof. Dr. M. Rothacher, Dr. J. Wickert, Dr. G. Dick, Dr. G. Gendt, (GFZ Potsdam)

Die hochgenaue Positionsbestimmung mit Hilfe des GPS oder auch demnächst verfügbarem GALILEO-Systems ist erst möglich, wenn die Atmosphäreneinflüsse auf die Signallaufzeiten korrigiert werden. Diese Korrekturen repräsentieren auch den Einfluss des atmosphärischen Wasserdampfes auf die Laufzeiten der GPS-Signale an der entsprechenden Bodenstation. Die GNSS-Boden netze (*Global Navigation Satellite System*) in Europa erreichen eine solche räumliche Dichte, so dass es mit Ihnen möglich wird eine dreidimensionale Verteilung des Wasserdampfes in der Atmosphäre unter Zuhilfenahme von tomografischen Rekonstruktionstechniken abzuleiten.

Dazu sind Abschätzungen der Genauigkeiten notwendig und Algorithmen zu erarbeiten, die ein Zusammenfassen der an einzelnen Stationen vorliegenden Daten ermöglicht.

Ziel ist es, den numerischen Wettermodellen quasi Echtzeit-Informationen über die dreidimensionale Wasserdampfverteilung in der Atmosphäre z.B. über Europa zur Verfügung zu stellen.

Weiterführung: Nein

Finanzierung: DFG (TE 51/26-1; RO 2330/5-1)

Auswirkung möglicher Klimaänderung auf das Wasserdargebot in verschiedenen Wassereinzugsgebieten Sachsens

Potential climate change impacts on the water supply in different drainage basins of Saxony

Prof. Dr. G. Tetzlaff (tetzlaff@uni-leipzig.de), Dr. A. Raabe (raabe@uni-leipzig.de),
Dr. M. Barth (mbarth@uni-leipzig.de), L. Schenk (ludwig.schenk@uni-leipzig.de)

Klimaveränderungen wirken sich auf das Wasserdargebot im Einzugsgebiet von Talsperren aus. Aus den Langfristvorhersagen unterschiedlicher Klimamodelle, deren Grundlage verschiedene Emissions-Szenarien sind, sollen Wasserdargebotsaussagen für die Region der sächsischen Talsperren abgeschätzt werden.

Weiterführung: Ja

Finanzierung: Landestalsperrenverwaltung des Freistaats Sachsen (LTV)

AG Hochatmosphäre
Upper Atmosphere

Selbstkalibrierende EUV/UV-Spektrophotometer SolACES
Auto-Calibrating EUV/UV Spectrophotometers SolACES

Prof. Dr. Christoph Jacobi (jacobi @ rz.uni-leipzig.de), Dr. B. Nikutowski, C. Unglaub

Das vom Fraunhofer IPM entwickelte Instrument SolACES (Solar Auto Calibrating EUV / UV Spectrometers), soll die solare Strahlung im Wellenlängenbereich von 17 bis 220 nm spektral aufgelöst mit hoher radiometrischer Absolutgenauigkeit messen. Im Projekt erfolgt neben Unterstützung der Missionsvorbereitung und -begleitung die Aufbereitung der Rohdaten, Datenauswertung, Erstellung empirischer Modelle der EUV-Strahlung, und Analyse der ionosphärischen Reaktion auf EUV-Variabilität.

Weiterführung: ja

Finanzierung: Auftrag (Fraunhofer-Institut für Physikalische Messtechnik)
Wiedereinstiegsstipendium (C. Unglaub)

Arbeitsgruppe Hochatmosphäre
Upper Atmosphere

Variabilität planetarer Wellen
Variability of planetary waves

Prof. Dr. Christoph Jacobi (jacobi @ rz.uni-leipzig.de), Prof. A.I. Pogoreltsev, S.S..
Derugina, Russian State Hydrometeorological University

Das Projekt umfasst experimentelle und numerische Studien atmosphärischer Wellenaktivität insbesondere in den Schichten oberhalb der Tropopause. Innerhalb des Projekts soll die Variabilität der Frühjahrsumstellung in der Stratosphäre im Detail untersucht werden, wobei Reanalysedaten und numerische Simulationen zum Einsatz kommen.

Weiterführung: nein

Finanzierung: DAAD, Leonard-Euler-Stipendienprogramm

AG Hochatmosphäre
Upper Atmosphere

Untersuchung der Mesosphäre/unteren Thermosphäre mit Meteorradar
Investigation of the mesosphere/lower thermosphere using meteor radar

Prof. Dr. Christoph Jacobi (jacobi @ rz.uni-leipzig.de), Prof. A. Oleynikov, V. Kukush,
Kharkiv Technical University of Radioelectronics

Innerhalb des Projekts werden VHF-Funksignale kommerzieller Fernsehsender zur Analyse von Meteoren zur Ableitung der horizontalen Windgeschwindigkeit in der Mesosphäre und unteren Thermosphäre verwendet. Validierung dieser Experimente erfolgt mit Radardaten der Universität Leipzig und Satellitendaten.

Weiterführung: nein

Finanzierung: DAAD

AG Hochatmosphäre
Upper Atmosphere

Planetare Wellen aus Radiookultationen
Planetary waves derived from radio occultations

Prof. Dr. Christoph Jacobi (jacobi @ rz.uni-leipzig.de), Prof. A.I. Pogoreltsev, E.
Chumak, Russian State Hydrometeorological University

Innerhalb des Projekts sollen globale Karten konvektiver Indizes, abgeleitet aus GPS-Radiookultationsdaten, erstellt werden. Diese werden ergänzt durch Analysen planetarer Wellenaktivität aus MetOffice-Reanalysen. Die Untersuchungen sollen klären, ob die konvektiven Indizes zur Vorhersage rascher Stratosphärenerwärmungen dienen können.

Weiterführung: ja

Finanzierung: DAAD, Leonhard-Euler-.Stipendium

AG Hochatmosphäre
Upper Atmosphere

Ableitung atomaren Sauerstoffs
Vertical profiles of atomic oxygen

Prof. Dr. Christoph Jacobi (jacobi @ rz.uni-leipzig.de), Prof. V. Yankovsky, E.
Fodotova, St. Petersburg State University

Innerhalb des Projekts wird ein Modell weiter entwickelt, welches die Raten atomaren Sauerstoffs aus denjenigen molekularen Sauerstoffs bestimmt. Das Modell dient der Messung von atomarem Sauerstoff mit Satelliten.

Weiterführung: nein

Finanzierung: DAAD, Leonhard-Euler-.Stipendium

AG Akustik
Acoustics

Schallausbreitung in urbanen Gebieten unter Berücksichtigung des Atmosphärenzustandes

Sound propagation in urban areas considering the state of the atmosphere

Dipl. Met. Gabi Fischer (g.fischer@uni-leipzig.de), Dr. Astrid Ziemann (ziemann@uni-leipzig.de), Prof. Dr. Manfred Wendisch (m.wendisch@uni-leipzig.de)

Aufgrund der dynamischen Entwicklung von Stadtregionen sind diese verdichteten Räume besonders anfällig gegenüber kurz- und langfristig wirkenden Risikofaktoren, wie z.B. Lärm, für die Gesundheit und Lebensqualität der Stadtbewohner. Vor allem der Straßenverkehrslärm stellt im urbanen Raum ein ungelöstes Umweltproblem mit Langzeitauswirkungen dar.

Zur verbesserten Abschätzung der Kopplung zwischen Atmosphärenstruktur und Schallausbreitung im urbanen Umfeld werden im verwendeten Schallstrahlenmodell neben den vertikalen meteorologischen Profilen auch die horizontal inhomogenen meteorologischen Strukturen integriert, um die Raum-Zeitskalen zu ermitteln, auf welchen der Atmosphäreneinfluss im städtischen Lärmmanagement zu berücksichtigen ist. Untersucht wird dabei die Schallausbreitung ab einigen 10 m Entfernung, da dort die Einflüsse meteorologischer Parameter, wie z.B. Lufttemperatur, Windvektor und Luftfeuchte, signifikant nachweisbar sind. Zur Validierung der Modellergebnisse sowie zur Abschätzung der Fehler und Grenzen des Modells sollen Messergebnisse aus dem urbanen Raum verwendet werden. Die Durchführung von Sensitivitätsstudien mit dem validierten Modell ermöglicht es, charakteristische Längenskalen für die Lärmbelastung abzuschätzen und Lärmindikatoren in Abhängigkeit von verschiedenen atmosphärischen Grenzschichtbedingungen zu bewerten.

Weiterführung: nein

Finanzierung: Wiedereinstiegsstipendium des Freistaates Sachsen

AG Akustik
Acoustics

Bestimmung des Energie- und Stoffaustauschs zwischen Bodenoberfläche und Pflanzenbestand, Umgebung und Atmosphäre durch mikrometeorologische Messverfahren der Anemometrie –Thermometrie, Teilprojekt: Akustische Strömungs- und Temperaturmessungen über einer Lysimeterfläche
Determination of the energy and matter exchange between the ground surface and vegetation canopy, environment and atmosphere using micro-meteorological measurement techniques of anemometry and thermometry, sub-project: Acoustic flow and temperature measurements over a lysimeter

Dr. Armin Raabe (raabe@uni-leipzig.de), Dr. Astrid Ziemann (ziemann@uni-leipzig.de), Dr. Manuela Barth (mbarth@uni-leipzig.de), Dipl. Met. Gabi Fischer (gfischer@uni-leipzig.de), Dipl.-Inf. (FH) Falk Kaiser (fkaiser@rz.uni-leipzig.de),
Dr. Sascha Reth (sascha.reth@ugt-online.de), Dr. Christian Heerdt (christian.heerdt@ugt-online.de), Rick Friedrich (rick.friedrich@ugt-online.de), Umwelt-Gerätetechnik UGT GmbH Müncheberg,
Prof. Dr. Christian Bernhofer (christian.bernhofer@tu-dresden.de), Dipl.-Hydrol. Markus Hahn (markus.hahn@tu-dresden.de), Dipl.-Geogr. David Schaffrath (david.schaffrath@tu-dresden.de), TU Dresden, Professur für Meteorologie

Für die Quantifizierung des Energie- und Gasaustausches am oberen Rand eines Lysimeters existieren bislang keine allseits anerkannten Messmethoden. Derzeit wird die Lysimeteroberfläche mit Sensoren bestückt, die allerdings ihrerseits die Wechselwirkung zwischen Lysimeter und Luftströmung beeinflussen können. Einen Beitrag zur Quantifizierung dieser Energie- und Stofftransporte können mikrometeorologische Messverfahren leisten, wenn es gelingt, die Sensoren nahe genug über einer Lysimeterfläche zu positionieren, ohne dass die Wechselwirkungsverhältnisse zwischen Lysimeter und Luftströmung gestört werden.

Deshalb wird hier ein über die Messfläche des Lysimeters aufgespanntes akustisches Temperatur- und Strömungsmessverfahren entwickelt, das in einem durch die akustischen Messstrecken begrenzten Volumen über dem Lysimeter die Wechselwirkung zwischen der Oberfläche und den Luftmassen über dem Lysimeter aufzeichnet. Unter Hinzunahme weiterer Sensoren (in erster Ausbaustufe CO₂, H₂O) soll es gelingen, den Energie- und Massenaustausch in diesem Volumen berührungslos zu sondieren. Dieses kontrolliert behandelte Volumen wird hier als "Akustische Kammer" bezeichnet.

Weiterführung: ja

Finanzierung: BMWi, Zentrales Innovationsprogramm Mittelstand (ZIM), Förderkennzeichen KF2709801BN0

AG Akustik
Acoustics

Wetterabhängige Schallausbreitung, Lärmschutz an Schießplätzen der Bundeswehr
Weather permitting sound propagation, noise protection at artillery range of the Bundeswehr

Dr. Armin Raabe (raabe@uni-leipzig.de),
Jun.-Prof. Dr. Astrid Ziemann (ziemann@uni-leipzig.de)
Dipl. Met. Michael Wilsdorf (mwils@uni-leipzig.de)

Dieses Projekt setzt die langjährige und erfolgreiche Zusammenarbeit des Institutes für Meteorologie der Universität Leipzig mit der Bundeswehr, hier im speziellen mit dem AGeoBw, fort. Anlass waren Artillerieschießen, bei denen die akustische Belastung in der Nachbarschaft von TrÜb-Plätzen derart erhöht war, dass es zu Beschwerden / Klagen von Bürgern und der Kommunen kam. Ein verstärkender Faktor war in den betreffenden Fällen u.a. die Wettersituation, bei der eine ausgeprägte Temperaturinversion zu einer anomalen Schallausbreitung führte.

Ziel dieser Studie ist deshalb die weitere Verbesserung der bestehenden Schallimmissionsprognose, sowohl in konzeptioneller Hinsicht, als auch in ihrer Praktikabilität sowie in der statistischen Absicherung der zu Grunde liegenden Auswertungen.

Datengrundlagen der schallklimatologischen Untersuchungen sind Radiosondenaufstiege des Deutschen Wetterdienstes und der Bundeswehr, die im Zeitraum 2001 bis mindestens 2007 an 14 Stationen im Bundesgebiet jeweils zu den Terminen 00 UTC und 12 UTC durchgeführt wurden. Damit erweitern diese Daten den untersuchten Datenumfang einschließlich der Vorgängerstudie (von 1990 bis 2000) auf 18 Jahre.

Weiterführung: ja

Finanzierung: AGeoBw; M/UR1M/7A180/7A524

2. Wiss. Veröffentlichungen Institut für Meteorologie 2011

Hauptautor	Autoren / Herausgeber	Titel, in: Zeitschrift, Ort; Verlag, Jahr, Seite von – bis
	Wendisch, M., and A. Ehrlich	Bodengebunde und flugzeuggetragene passive Fernerkundung von Wolken mit Hilfe von solaren Strahlungsmessungen. <i>Promet</i> , 36, 2011, 119-128.
	Otto, S., T. Trautmann, and M. Wendisch	On realistic size equivalence and shape of spheroidal Saharan mineral dust particles applied in solar and thermal radiative transfer calculations. <i>Atmos. Chem. Phys.</i> , 11, 2011, 4469-4490, doi:10.5194/acp-11-4469-2011.
	Otto, S., and M. Meringer	Positively homogeneous functions in atmospheric radiative transfer theory, S. Otto and M. Meringer, <i>J. Math. Anal. Appl.</i> (2011), 376, 588-601.
	S. Bauer, S., E. Bierwirth, M. Esselborn, A. Petzold, A. Macke, T. Trautmann and M. Wendisch	Airborne spectral radiation measurements to derive solar radiative forcing of Saharan dust mixed with biomass burning smoke particles. <i>Tellus</i> , 63B, 742-750. doi: 10.1111/j.1600-0889.2011.00567.x
	Ehrlich, A., E. Bierwirth, M. Wendisch, A. Herber, and J.-F. Gayet	Airborne hyperspectral surface and cloud bi-directional reflectivity observations in the Arctic using a commercial, digital camera, <i>Atmos. Chem. Phys. Discuss.</i> , 11, 2011, 24591-24629, doi:10.5194/acpd-11-24591-2011
	Tegen, I., E. Bierwirth, B. Heinold, J. Helmert, and M. Wendisch	The effect of measured surface albedo on modeled Saharan dust radiative forcing. <i>J. Geophys. Res.</i> , 115, 2010, D24312, doi:10.1029/2009JD013764.
	Jahn, H. J., A. Schneider, S. Breitner, R. Eißner, M. Wendisch, and A. Krämer	Particulate matter pollution in the megacities of the Pearl River Delta, China – A systematic literature review and health risk assessment. <i>Int. J. Hyg. Environ. Health</i> , 214, 2011, 281-295, doi:10.1016/j.ijheh.2011.05.008
	Baumgardner, D., J.-L. Brenguier, A. Bucholtz, H. Coe, P. DeMott, T. J. Garrett, J.-F. Gayet, M. Hermann, A. Heymsfield, A. Korolev, M. Krämer, A. Petzold, W. Strapp, P. Pilewskie, J. Taylor, C. Twohy, M. <u>Wendisch</u> , W. Bachalo, and P. Chuang	Airborne instruments to measure atmospheric aerosol particles, clouds and radiation: A cook's tour of mature and emerging technology. <i>Atmos. Res.</i> , 102, 2011, 10-29. doi:10.1016/j.atmosres.2011.06.021
	Yang, P., M. Wendisch, L. Bi, G. Kattawar, M. Mishchenko, and Y. Hu	Dependence of extinction cross-section on incident polarization state and particle orientation. <i>J. Quant. Spectr. & Rad. Trans.</i> , 112, 2011, 2035-2039. doi:10.1016/j.jqsrt.2011.04.012
	Ansmann, A., A. Petzold, K. Kandler, I. Tegen, M. Wendisch, D. Müller, B. Weinzierl, T. Müller, and J. Heintzenberg	Saharan Mineral Dust Experiments SAMUM-1 and SAMUM-2: what have we learned? <i>Tellus</i> , 63B, 2011, 403-429. doi: 10.1111/j.1600-0889.2011.00555.x
	Heinold, B., I. Tegen, S. Bauer, and M. Wendisch	Regional modelling of Saharan dust and biomass-burning smoke – Part 2: Direct radiative forcing and atmospheric dynamic response. <i>Tellus</i> , 63B, 2011, 800-813. doi: 10.1111/j.1600-0889.2011.00574.x
	Köhler, C. H., T. Trautmann, E. Lindermeir, W. Vreeling, K. Lieke, K. Kandler, B. Weinzierl, S. Groß, M. Tesche, , and M. Wendisch	Thermal IR radiative properties of mixed mineral dust and biomass aerosol during SAMUM-2. <i>Tellus</i> , 63B, 2011, 751-769. doi: 10.1111/j.1600-0889.2011.00563.x
	Mey, B., C. Xingfeng, L. Zhengqiang, X. Gu, Y. Tao, and M. Wendisch	Airborne measurements of reflectivity and albedo of urban and rural surfaces of Megacities, <i>Wiss. Mitt. Inst. f. Meteorol. Uni. Leipzig</i> , Bd. 48, 2011, 152 S.
	Otto, S.	On the overestimation of gas absorption optical depth due to spectral layer-transmissivity averaging, <i>Wiss. Mitt. Inst. f. Meteorol. Uni. Leipzig</i> , Bd. 48, 2011, 83-94
	Bender, M., Stosius, R., Zus, F., Dick,	GNSS water vapour tomography - Expected

	G., Wickert, J., Raabe, A.	improvements by combining GPS, GLONASS and Galileo observations. <i>Advances in Space Research</i> , Vol. 47, No. 5, p. 886-897, doi: 10.1016/j.asr.2010.09.011, 2011
	Bender, M., Dick, G., Ge, M., Deng, Z., Wickert, J., Kahle, H.-G., Raabe, A., Tetzlaff, G.	Development of a GNSS Water Vapor Tomography System Using Algebraic Reconstruction Techniques <i>Advances in Space Research</i> , Vol. 47, No. 10, p. 1704-1720, doi: 10.1016/j.asr.2010.05.034, 2011
	J. Van Baelen, Reverdy, J.M., Tridon, F., Labbouz, L., Dick, G., Bender, M., Hagen, M.	On the relationship between water vapour field evolution and the life cycle of precipitation systems <i>Quarterly Journal of the Royal Meteorological Society</i> , Vol. 137, No. S1, p. 204–223, 2011
	Spänkuch, D., Güldner, J., Steinhagen, H., Bender, M.	Analysis of a dryline-like feature in northern Germany detected by ground-based microwave profiling <i>Meteorologische Zeitschrift</i> , Vol. 20, No. 4, p. 409-421, 2011
	Brecht, B., Raabe A., Bender, M.	Comparison of refractivity profiles derived by Radiosonde soundings and GNSS tomography <i>Wiss. Mitt. Inst. f. Meteorol. Uni. Leipzig</i> , Bd. 48, 2011, 13-22
	Ziemann, A., Raabe, A.	Numerical sensitivity tests of acoustically derived meteorological quantities inside an ‚acoustic chamber‘ <i>Wiss. Mitt. Inst. f. Meteorol. Uni. Leipzig</i> , Bd. 48, 2011, 113-126
	Barth M., G. Fischer, A. Raabe	Acoustic measurements in air – A model apparatus for education and testing, <i>Wiss. Mitt. Inst. F. Meteorol. Univ. Leipzig</i> , 48, 2011, 1-12.
	Barth M., A. Raabe	Acoustic tomographic imaging of temperature and flow fields in air, <i>Meas. Sci. Technol.</i> , 22, 2011, 035102 (13pp).
	Weber,T., Räisänen,P., Quaas, J.	Evaluation of the subgrid-scale variability scheme for water vapor and cloud condensate in the ECHAM5 model using satellite data, <i>Quart. J. Royal Meteorol. Soc.</i> , 137, 2079–2091, doi 10.1002/qj.887, 2011
	D. Klocke, R. Pincus, J. Quaas	Evaluation of the subgrid-scale variability scheme for water vapor and cloud condensate in the ECHAM5 model using satellite data, <i>Quart. J. Royal Meteorol. Soc.</i> , 137, 2079–2091, doi 10.1002/qj.887
	Quaas, J., O. Boucher, N. Bellouin, S. Kinne	Which of satellite- or model-based estimates is closer to reality for aerosol indirect forcing? - Reply to Penner et al., <i>Proc. Nat. Acad. Sci. USA</i> , doi 10.1073/pnas.1114634108, 2011.
	Peters, K., J. Quaas, H. Graßl	A search for large-scale effects of ship emissions on clouds and radiation in satellite data, <i>J. Geophys. Res.</i> , doi 10.1029/2011JD016531, 2011
	Unglaub, C., Ch. Jacobi, G. Schmidtke, B. Nikutowski, R. Brunner,	EUV-TEC proxy to describe ionospheric variability using satellite-borne solar EUV measurements: first results. <i>Adv. Space Res.</i> , 47, 1578-1584, doi:10.1016/j.asr.2010.12.014.
	Stober, G., Ch. Jacobi, W. Singer,	Meteoroid mass determination from underdense trails. <i>J. Atmos. Solar-Terr. Phys.</i> , 73, 895-900, doi:10.1016/j.jastp.2010.06.009.
	Placke, M., G. Stober, Ch. Jacobi,	Gravity wave momentum fluxes in the MLT—Part I: Seasonal variation at Collm (51.3°N, 13.0°E). <i>J. Atmos. Solar-Terr. Phys.</i> , 73, 904-910, doi:10.1016/j.jastp.2010.07.012.
	Placke, M., P. Hoffmann, E. Becker, Ch. Jacobi, W. Singer, M. Rapp	Gravity wave momentum fluxes in the MLT – Part II: Meteor radar investigations at high and midlatitudes in

		comparison with modeling studies. <i>J. Atmos. Solar-Terr. Phys.</i> , 73, 911-920, doi:10.1016/j.jastp.2010.05.007.
	Stober, G., W. Singer, Ch. Jacobi, 2011:	Cosmic radio noise observations using a mid-latitude meteor radar. <i>J. Atmos. Solar-Terr. Phys.</i> , 73, 1069-1076, doi:10.1016/j.jastp.2010.07.018.
	Fytterer, T., Ch. Jacobi	Climatology of the 8-hour tide over Collm (51.3°N, 13°E). <i>Rep. Inst. Meteorol. Univ. Leipzig</i> 48, 23-32.
	Hoffmann, P., Ch. Jacobi	Gravity wave influence on middle atmosphere dynamics in model and satellite data. <i>Rep. Inst. Meteorol. Univ. Leipzig</i> 48, 33-47.
	Jacobi, Ch., P. Hoffmann, C. Unglaub, M. Placke, G. Stober,	Peculiarities of mesosphere/lower thermosphere parameters during solar minimum 23/24. <i>Rep. Inst. Meteorol. Univ. Leipzig</i> 48, 49-58.
	Kukush, V., Ch. Jacobi, A. Oleynikov	Possible use of television broadcasting signals for wind measurements by the meteor radiolocation method – main theoretical aspects and results of first experiments. <i>Rep. Inst. Meteorol. Univ. Leipzig</i> 48, 59-72
	Kukush, V., A. Oleynikov, Ch. Jacobi, Y. Lykov	Theoretical and experimental investigation of wind measurements at 80-105 km altitude by television broadcasting signals (in russ.), <i>Radiotekhnika: All-Ukr. Sci. Interdep. Mag.</i> , 165, 10-19.
	Jacobi, Ch.	Meteor radar measurements of mean winds and tides over Collm (51.3°N, 13°E) and comparison with LF drift measurements 2005-2007. <i>Adv. Radio Sci.</i> 9, 335-341.
	Jacobi, Ch., P. Hoffmann, M. Placke, G. Stober,	Some anomalies of mesosphere/lower thermosphere parameters during the recent solar minimum. <i>Adv. Radio Sci.</i> 9, 343-348.
	Xu, X., A.H. Manson, C.E. Meek, Ch. Jacobi, C.M. Hall, J.R. Drummond	Verification of the mesospheric winds within the Canadian Middle Atmosphere Model Data Assimilation System using radar measurements. <i>J. Geophys. Res.</i> , 116, D16108, doi:10.1029/2011JD015589.
	Xu, X., A. Manson, C. Meek, C. Jacobi, C. Hall, J. Drummond	Mesospheric wind semidiurnal tides within the Canadian Middle Atmosphere Model Data Assimilation System. <i>J. Geophys. Res.</i> , 116, D17102, doi:10.1029/2011JD015966.
	Dorninger, M., C. D. Whiteman, B. Bica, S. Eisenbach, B. Pospichal, R. Steinacker	Meteorological Events Affecting Cold-Air Pools in a Small Basin. <i>J. Appl. Meteor. Climatol.</i> , 50, 2223-2234. doi: http://dx.doi.org/10.1175/2011JAMC2681.1

Mitarbeiter am Institut für Meteorologie, 2011

Wissenschaftliche und technische Mitarbeiter am Institut für Meteorologie, 2011

Name		mail-adresse
Barth	Manuela	mbarth@rz.uni-leipzig.de
Bender	Michael	bender@gfz-potsdam.de
Bierwirth	Eike	eike.bierwirth@uni-leipzig.de
Ehrlich	Andre	a.ehrlich@uni-leipzig.de
Feck-Yao	Wolfgang	feckyao@uni-leipzig.de
Finger	Fanny	fanny.finger@uni-leipzig.de
Fischer	Gabi	gfischer@rz.uni-leipzig.de
Fricke	Clemens	fricke@uni-leipzig.de
Hirsch	Kerstin	khirsch@uni-leipzig.de
Hoffmann	Peter	phoffma@rz.uni-leipzig.de
Jacobi	Christoph	jacobi@rz.uni-leipzig.de
Jäkel		e.jaekel@uni-leipzig.de
Kaiser	Falk	fkaiser@rz.uni-leipzig.de
Mey	Britta	b.mey@uni-leipzig.de
Nikutowski	Bernd	bernd.nikutowski@ipm.fraunhofer.de
Pilewskie (G)	Peter	peter.pilewskie@uni-leipzig.de
Pospichal	Bernhard	bernhard.pospichal@uni-leipzig.de
Quaas	Johannes	johannes.quaas@uni-leipzig.de
Raabe	Armin	raabe@uni-leipzig.de
Rehnert	Jutta	rehnert@uni-leipzig.de
Rosenow	Dagmar	d.rosenow@uni-leipzig.de
Schäfer	Michael	michael.schaefer@uni-leipzig.de
Schönenfeldt	Hans-Jürgen	schoenfeldt@uni-leipzig.de
Staake	Karin	staake@uni-leipzig.de
Walter	Jörg	jwalter@uni-leipzig.de
Weiße	Frank	weisse@uni-leipzig.de
Wendisch	Manfred	m.wendisch@uni-leipzig.de
Werner	Frank	f.henrich@uni-leipzig.de
Wilsdorf	Michael	mwils@uni-leipzig.de

Immatrikulationen am Institut f. Meteorologie

Immatrikulationen Meteorologiestudenten			BSC											
Datum	Semester		1.FS	2. FS	3.FS	4.FS	5.FS	6. FS	7.FS	8.FS	9. FS	10.FS	>10.FS	Summe
15.10.2011	WS 11/12		60		27			26	1	19		1		134
15.10.2011	WS 11/12									21		17		48
15.04.2011	SS 11			49		30		21		2				102
15.04.2011	SS 11									17		10		27
15.10.2010	WS 10/11		64		34		20		20		9		5	152
15.04.2010	SS 10			32		21		20		9		14		96
15.10.2009	WS 09/10		67	0	21	0	20	0	11	0	14		7	140
15.04.2009	SS 09		0	71	0	28	0	12	0	14	0	23		148
15.10.2008	WS 08/09		71	0	28	0	12	0	14	0	23	1	25	174
15.04.2008	SS 08		0	54	0	14	0	19	0	25	1	18	13	144
15.10.2007	WS 07/08		98	0	15	0	22	0	26	1	18	2	19	201
15.04.2007	SS 07		0	23	0	32	0	35	1	19	2	13	12	137
13.12.2006	WS 06/07		31	0	40	0	36	0	24	2	14	1	17	175
15.04.2006	SS 06		0	82	0	46	0	29	3	14	1	17	7	200
15.10.2005	WS 05/06		109	0	49	0	30	2	16	1	17	1	13	237
07.06.2005	SS 2005		0	83	0	33	1	19	0	17	1	12	8	177
08.12.2004	WS 04/05		97	0	35	1	20	0	19	0	12	1	15	200
07.06.2004	SS 04		0	57	0	24	0	18	1	13	0	11	10	134
03.12.2003	WS 03/04		68	1	25	0	20	1	13	1	12	1	13	155
26.05.2003	SS 03		0	42	0	19	0	15	0	14	1	12	6	109
14.10.2002	WS 02/03		45	0	19	0	16	0	15	1	12	1	9	118
29.05.2002	SS 02		0	38	0	20	0	17	1	13	2	7	4	102
06.12.2001	WS 01/02		43	0	21	0	16	0	13	0	7	0	5	105
31.05.2001	SS 01		0	31	1	22	0	19	0	8	0	5	3	89
07.12.2000	WS 00/01		41	1	27	0	22	0	8	0	6	1	6	112
05.05.2000	SS 00		0	34	0	24	0	8	0	8	1	6	3	84
01.12.1999	WS 99/00		40	0	24	0	9	0	9	0	6	1	6	95
31.05.1999	WS 99		0	29	0	11	0	13	0	8	1	5	3	70
16.12.1998	WS 98/99		36	0	11	0	17	1	9	1	5	0	8	88
22.04.1998	SS 98		1	21	0	17	0	8	1	6	0	7	2	63
10.11.1997	WS 97/98		29	0	17	0	10	1	8	0	7	0	4	76

Abschlussarbeiten Institut für Meteorologie 2011

Promotionen

Patric Seifert

Dust-related ice formation in the troposphere: A statistical analysis based on 11 years of lidar observations of aerosols and clouds over Leipzig

Markus Ziese

Entwicklung und Aufbau einer mobilen Version des Leipzig Aerosol Cloud Interaction Simulator (LACIS) sowie dessen Einsatz zur Untersuchung des hygroskopischen Wachstums und der Aktivierung laborgenerierter Aerosolpartikel

Peter Hoffmann

Planetary Wave Coupling between Stratosphere and Ionosphere by Gravity Wave Modulation

Alexander Schladitz

Parametrization of relative humidity- and wavelength-dependent optical properties of mixed Saharan dust and marine aerosol

Matthias Tesche

Vertical profiling of aerosol optical properties with multiwavelength aerosol lidar during the Saharan Mineral Dust Experiments

Diplom-Abschlüsse 2011

Name / Vorname	DA-Thema
Vogelsberg, Ulrike	Implementierung eines Bodenmodells in das Atmosphärenmodell ASAM
Schäfer, Michael	Untersuchung des Aktivierungsverhalten atmosphärischer Aerosolpartikel in der nordchinesischen Tiefebene
Schenk, Ludwig	Abschätzung der Bandbreite des Wasserdargebotes unter Verwendung der Daten der Klimaszenarien
Jähn, Michael	Die feuchten kompressiblen Euler-Gleichungen Entropie versus Energie
Finger, Fanny	Aerosolschichten in der oberen Troposphäre und Stratosphäre über Mitteleuropa
Müller, Anja	Mehrwellenlängen-Ramanlidar-Messungen über Leipzig 2000-2010
Skandera, Dominik	Untersuchung der vertikalen Aerosolverteilung anhand von Lidarmessverfahren mittels Eeilometer am IfT
Hänel, Andreas	Untersuchungen zu vertikalen Aerosolprofilen über der EUCCARI-Meßstation SDZ nordöstlich von Peking anhand von Ramanlidarmessungen mit Polly
Spörl, Ulrike	Bestimmung des Aerosol-Signals in den SEVIRI-Kanälen anhand von MODIS-Aerosolprodukten über dem Ozean
Größ, Johannes	Partikelneubildung in der atmosphärischen Grenzschicht: Zusammenhang mit mikrometeorologischen Parametern
Igloffstein, Julia (geb. Geisler)	Ableitung der optischen Dicke bei Zirrusbewölkung aus unabhängigen Strahldichte- und Lidarmessungen

MSC-Abschlüsse 2011

Bach, Stefan	Anpassung des agrarmeteorologischen Wasserhaushaltsmodells METVER an aktuelle Erfordernisse vor dem Hintergrund sich wandelnder klimatischer Randbedingungen und pflanzenbaulichen Gegebenheiten
Bethke, Julia	Liquid Water Content Measurements in Trade Wind Cumuli

BSC-Abschlüsse 2010

Name / Vorname	Thema
Stieger, Bastian	Stratosphärisches Ozon und Zirkulation der mittleren Atmosphäre
Kanter, Sandra	Untersuchung der Genauigkeit von Zweistrom-Strahlungstransportmodellen angewendet auf saharamineralstaubhaltige Atmosphären
Brock, Verena	Windgeschwindigkeitsgradienten oberhalb der Prandtl-Schicht
Kundisch, Marcus	Bestimmung des Wolkenbedeckungssgrades mit Hilfe eines Allsky-Imagers
Flachsbart, Edda	Bestimmung kurzkettiger Dicarbonsäuren in troposphärischen Partikeln und Woleknwasser im HCCT-2010 Feldexperiment
Gatzsche, Kathrin	Darstellung der Kármán-Konstante durch bodennahe Windmessungen

Rüffert, Jörg	Bestimmung der Höhe der Atmosphärischen Grenzschicht mittels LIDAR
Hage, Benjamin	Beregnungsbedürftigkeit landwirtschaftlicher Fruchtarten vor dem Hintergrund des manifesten und erwarteten Klimawandels in Thüringen
Lilienthal, Friederike	Beregnungsbedürftigkeit landwirtschaftlicher Fruchtarten vor dem Hintergrund des manifesten und erwarteten Klimawandels in Sachsen
Klotzsche, Sindy	Initialisierung tropischer Wirbelsürme
Beyer, Alexander	Einfluss von Schneefeldern auf die Albedo borealer Nadelwälder
Böhme, Maria	Statistische Aufarbeitung der Bodentemperaturreihe der Säkularstation Potsdam
Bischoff, André	Schwerewellen im Zirkulationsmodell MUAM
Rosch, Jan	Kalibrierung des Webcam Signals bezüglich durch Winderosion transportierter Sandkörner
Pietsch, Alexandra	Analyse der Messgenauigkeit von Temperatur- und Feuchteprofilen aus Flugzeug-, Radionsonden- und Dropsondenmessungen und Vergleich mit Simulationen des ECMWF-Modells für Fallbeispiele der SORPIC Messkampagne
Rehn, Johanna	Die räumliche Verteilung ultrafeiner Partikel auf der städtischen Mikroskala (<100m): Experimentelle Untersuchung mit Analyse der meteorologischen Transportvorgänge
Rittmeister, Franziska	Untersuchungen und Analyse des Stadtklimas
Herenz, Paul	Untersuchung zum Einfluss von (messgerätespezifischen inneren) Temperaturen auf das Aktivierungsverhalten von Aerosolpartikeln
Schmidt, Martin	Das extreme Minimum solarer Aktivität 2008/2009

**Wissenschaftliche Mitteilungen aus dem Institut für Meteorologie der
Universität Leipzig**

- Band 1 *A. Raabe, G. Tetzlaff und W. Metz* (Edn.), 1995: Meteorologische Arbeiten aus Leipzig I
- Band 2 *R. Devantier*, 1995: Wolkenbildungsprozesse über der südwestlichen Ostsee - Anwendungen eines neuen Wolkenschemas in einem mesoskaligen Modell
- Band 3 *J. Laubach*, 1996: Charakterisierung des turbulenten Austausches von Wärme, Wasserdampf und Kohlendioxid über niedriger Vegetation anhand von Eddy-Korrelations-Messungen
- Band 4 *A. Raabe und J. Heintzenberg* (Edn.), 1996: Meteorologische Arbeiten aus Leipzig II
- Band 5 Wind- und Seegangsatlas für das Gebiet um Darß und Zingst
- Band 6 *D. Hinneburg, A. Raabe und G. Tetzlaff*, 1997: Teil I: Windatlas
W. von Hoyningen-Huene und G. Tetzlaff (Edn.), 1997: Sediment and Aerosol
Teil I: Beiträge zur Alfred-Wegener-Konferenz, Leipzig 1997
Teil II: Aktuelle Beiträge aus dem Institut für Meteorologie
- Band 7 *B.-R. Beckmann*, 1997: Veränderungen in der Windklimatologie und in der Häufigkeit von Sturmhochwassern an der Ostseeküste Mecklenburg-Vorpommerns
- Band 8 *P. Posse*, 1997: Bestimmung klimarelevanter Parameter des maritimen Aerosols unter besonderer Berücksichtigung der Nichtkugelform realer Aerosolteilchen
- Band 9 *A. Raabe, K. Arnold und J. Heintzenberg* (Edn.), 1998: Meteorologische Arbeiten aus Leipzig III
- Band 10 Wind- und Seegangsatlas für das Gebiet um Darß und Zingst, Teil II, 1998:
D. Hinneburg, A. Raabe und G. Tetzlaff: Vergleich Windatlas –Beobachtungsdaten; *M. Börngen, H.-J. Schönfeldt, R. Riechmann, G. Panin und G. Tetzlaff*: Seegangsatlas; *M. Stephan und H.-J. Schönfeldt*: Sedimenttransportatlas
- Band 11** *J. Rissmann, 1998:* Der Einfluss langwelliger Strahlungsprozesse auf das bodennahe Temperaturprofil
- Band 12 *A. Raabe, K. Arnold und J. Heintzenberg* (Edn.), 1999: Meteorologische Arbeiten aus Leipzig IV
- Band 13 *U. Müller, W. Kuttler und G. Tetzlaff* (Edn.), 1999: Workshop Stadtclima 17. / 18. 02. 1999 in Leipzig
- Band 14 *R. Surkow*, 1999: Optimierung der Leistungsverfügbarkeit von Windenergie durch ihre Integration in Wind-Biogas-Hybridanlagen
- Band 15 *N. Mölders*, 1999: Einfache und akkumulierte Landnutzungsänderungen und ihre Auswirkungen auf Evapotranspiration, Wolken- und Niederschlagsbildung
- Band 16 *G. Tetzlaff und U. Grünwald* (Edn.), 1999:
2. Tagung des Fachausschusses Hydrometeorologie 15./16. 11. 1999 in Leipzig
- Band 17 *A. Raabe und K. Arnold* (Edn.), 2000: Meteorologische Arbeiten aus Leipzig V
- Band 18 *K. Arnold*, 2000: Ein experimentelles Verfahren zur Akustischen Tomographie im Bereich der atmosphärischen Grenzschicht
- Band 19 *A. Ziemann*, 2000: Eine theoretische Studie zur akustischen Tomographie in der atmosphärischen Grenzschicht
- Band 20 *Ch. Jacobi*, 2000: Midlatitude mesopause region dynamics and its coupling with lower and middle atmospheric processes
- Band 21 *M. Klingspohn*, 2000: Interdekadische Klimavariabilität über dem Nordatlantik – Statistische Analysen und Modellstudien –
- Band 22 *A. Raabe und K. Arnold* (Edn.), 2001: Meteorologische Arbeiten aus Leipzig VI
- Band 23 *K. Arnold, A. Ziemann, G. Tetzlaff, V. Mellert und A. Raabe* (Edn.), 2001: International Workshop Tomography and Acoustics: Recent developments and methods 06. - 07.03.2001 in Leipzig
- Band 24 *O. Fanenbruck*, 2001: Ein thermophysiolgisches Bewertungsmodell mit Anwendung auf das Leipziger Stadtgebiet
- Band 25 *M. Lange*, 2001: Modellstudien zum CO₂-Anstieg und O₃-Abbau in der mittleren Atmosphäre und Einfluß des Polarwirbels auf die zonale Symmetrie des Windfeldes in der Mesopausenregion
- Band 26 *A. Raabe und K. Arnold* (Edn.), 2002: Meteorologische Arbeiten aus Leipzig VII
- Band 27 *M. Simmel*, 2002: Ein Modul zur spektralen Beschreibung von Wolken und Niederschlag in einem Mesoskalenmodell zur Verwendung auf Parallelrechnern

- Band 28 *H. Siebert*, 2002: Tethered-Balloon Borne Turbulence Measurements in the Cloudy Boundary Layer
- Sonderband *G. Tetzlaff* (Hrsg.), 2002:- Atmosphäre - Aktuelle Beiträge zu Luft, Ozon, Sturm, Starkregen und Klima
- Band 29 *U. Harlander*, 2003: On Rossby wave propagation in atmosphere and ocean
- Band 30 *A. Raabe und K. Arnold* (Edn.), 2003: Meteorologische Arbeiten aus Leipzig VIII
- Band 31 *M. Wendisch*, 2003: Absorption of Solar Radiation in the Cloudless and Cloudy Atmosphere
- Band 32 *U. Schlink*, 2003: Longitudinal Models in Biometeorology: Effect Assessment and Forecasting of Ground-level Ozone
- Band 33 *H. Heinrich*, 2004: Finite barotrope Instabilität unter synoptischem Antrieb
- Band 34 *A. Raabe und K. Arnold* (Edn.), 2004: Meteorologische Arbeiten aus Leipzig IX
- Band 35 *C. Stolle*, 2004: Three-dimensional imaging of ionospheric electron density fields using GPS observations at the ground and onboard the CHAMP satellite
- Band 36 *A. Raabe und K. Arnold* (Edn.), 2005: Meteorologische Arbeiten (X) und Jahresbericht 2004 des Institutes für Meteorologie der Universität Leipzig
- Band 37 *A. Raabe und K. Arnold* (Edn.), 2006: Meteorologische Arbeiten (XI) und Jahresbericht 2005 des Institutes für Meteorologie der Universität Leipzig
- Band 38 *K. Fröhlich*, 2006: The Quasi Two-Day Wave – its impact on zonal mean circulation and wave-wave interactions in the middle atmosphere
- Band 39 *K. Radtke*, 2006: Zur Sensitivität von Starkwindfeldern gegenüber verschiedenen meteorologischen Parametern im Mesoskalenmodell LM
- Band 40 *K. Hungershöfer*, 2007: Optical Properties of Aerosol Particles and Radiative Transfer in Connection with Biomass Burning
- Band 41 *A. Raabe* (Hrsg.), 2007: Meteorologische Arbeiten (XII) und Jahresbericht 2006 des Institutes für Meteorologie der Universität Leipzig
- Band 42 *A. Raabe* (Hrsg.), 2008: Meteorologische Arbeiten (XIII) und Jahresbericht 2007 des Institutes für Meteorologie der Universität Leipzig
- Band 43 *A. Kniffka* , 2008: Einfluss der Inhomogenitäten von Aerosol, Bodenalbedo und Wolken auf das aktinische Strahlungsfeld der Atmosphäre
- Band 44 *M. Barth*, 2009: Akustische Tomographie zur zeitgleichen Erfassung von Temperatur- und Strömungsfeldern
- Band 45 *A. Raabe* (Hrsg.), 2009: Meteorologische Arbeiten (XIV) und Jahresbericht 2008 des Institutes für Meteorologie der Universität Leipzig
- Band 46 *G. Stober*, 2009: Astrophysical Studies on Meteors using a SKiYMET All-Sky Meteor Radar
- Band 47 *A. Raabe* (Hrsg.), 2010: Meteorologische Arbeiten (XV) und Jahresbericht 2009 des Institutes für Meteorologie der Universität Leipzig
- Band 48 *A. Raabe* (Hrsg.), 2011: Meteorologische Arbeiten (XVI) und Jahresbericht 2010 des Institutes für Meteorologie der Universität Leipzig
- Band 49 *A. Raabe* (Hrsg.), 2012: METTOOLS_VIII Tagungsband
- Band 50 *A. Raabe* (Hrsg.), 2012: Meteorologische Arbeiten (XVII) und Jahresbericht 2011 des Institutes für Meteorologie der Universität Leipzig